

## Distribution Agreement

In presenting this thesis or dissertation as a partial fulfillment of the requirements for an advanced degree from Emory University, I hereby grant to Emory University and its agents the non-exclusive license to archive, make accessible, and display my thesis or dissertation in whole or in part in all forms of media, now or hereafter known, including display on the world wide web. I understand that I may select some access restrictions as part of the online submission of this thesis or dissertation. I retain all ownership rights to the copyright of the thesis or dissertation. I also retain the right to use in future works (such as articles or books) all or part of this thesis or dissertation.

Signature:

---

Jacob Billings

---

Date

Multiscale Statics and Dynamics of Cerebral Functional Connectivity

By

Jacob Charles Wright Billings  
Doctor of Philosophy

Graduate Division of Biological and Biomedical Sciences  
Neuroscience

---

Sheila Keilholz  
Advisor

---

Ying Guo  
Committee Member

---

Xiaoping Hu  
Committee Member

---

Dieter Jaeger  
Committee Member

---

Alessio Medda  
Committee Member

Accepted:

---

Lisa A. Tedesco, Ph.D.  
Dean of the James T. Laney School of Graduate Studies

---

Date

Multiscale Statics and Dynamics of Cerebral Functional Connectivity

By

Jacob Charles Wright Billings  
B.S., Florida Agricultural and Mechanical University, 2011

Advisor: Shella D. Keilholz, Ph.D.

An abstract of  
A dissertation submitted to the Faculty of the  
James T. Laney School of Graduate Studies of Emory University  
in partial fulfillment of the requirements for the degree of  
Doctor of Philosophy  
Graduate Division of Biological and Biomedical Sciences  
Neuroscience  
2017

## Abstract

### Multiscale Statics and Dynamics of Cerebral Functional Connectivity

By Jacob C. W. Billings

The advent of whole-brain functional imaging through Blood-Oxygen Level Dependent (BOLD) functional Magnetic Resonance Imaging (fMRI) invites novel analytical frameworks to understand the brain's intrinsic functional organization. As brains are complex self-assembled systems, a mechanistic view of brain activity is expected to observe emergent structures interacting across multiple spectral, spatial, and temporal scales. Analytical frameworks that incorporate information at multiple scales may therefore provide additional insights into brain physiology. Chapter 1 introduces this line of reasoning in greater detail. Because BOLD fMRI is an indirect measure of neuronal activity, Chapter 2 pursues an optimal preprocessing strategy for increasing the information content of the BOLD signal. A strategy that normalizes voxel-wise BOLD signals via z-scoring and removes motion noise via motion parameter regression was found to effectively isolate BOLD signal energetics to the brain's gray matter. Enhancing the signal-to-noise ratio of gray matter BOLD signals is expected to most effectively enhance the proportion of spontaneous hemodynamic (BOLD) fluctuations attributable to neuronal signaling. This is because synaptic activity accounts for the majority of energy usage in the brain, and the dendritic arbor of the central nervous system is unmyelinated gray matter. In Chapter 3, preprocessed, voxel-level BOLD signals are filtered into multiple spectral domains in order to identify the spectral components that best reveal the brain's intrinsic organization. Graphs of the brain's functional connectivity—its spatial network architecture—most closely resemble known brain networks in several pass-bands within the low-frequency fluctuation range ( $\sim 0.1$  to  $\sim 0.01$  Hz). To discover just why low-frequency spectra of the BOLD signal are most effective at revealing the brain's architecture, Chapter 4 links hemodynamic connectivity to neuroelectric connectivity through multimodal studies in the rodent brain. Long-term (static) BOLD connectivity is demonstrated to correspond to static local field potential (LFP) connectivity when neuroelectric activity is filtered into either delta (1-4 Hz), alpha (8-12 Hz), or gamma (40-60 Hz) pass-bands. These findings support the theoretical interpretation of neurovascular coupling as a diffusion-mediated process involving small signaling molecules that communicate information about changing neuronal metabolic load to the cardiovascular system. Essentially, low-frequency fluctuations in the BOLD signal are low-pass filtered versions of neuroelectric activity. Whereas Chapters 2 through 4 pursue long-term trends in coordinated brain activity, Chapter 5 pursues the question of how to identify the kinds of time-varying BOLD dynamics expected to relate to ongoing mental activity. To this end, the instantaneous state space of multi-scale BOLD dynamics is embedded onto a two-dimensional sheet, thereby providing a visually tractable map of the brain dynamics. Discrete epochs of experimentally defined tasks are shown to agglomerate into densely populated peaks in the map space. The brain activities associated with each map region are further investigated in order to better understand how the brain produces a range of experimentally defined states. Taken as a whole, the enclosed dissertation research demonstrates the pervasiveness of the brain's multi-scalar architecture, and the utility that this perspective affords towards the interpretation of various and complex brain functions.

Multiscale Statics and Dynamics of Cerebral Functional Connectivity

By

Jacob Charles Wright Billings  
B.S., Florida Agricultural and Mechanical University, 2011

Advisor: Shella D. Keilholz, Ph.D.

A dissertation submitted to the Faculty of the  
James T. Laney School of Graduate Studies of Emory University  
in partial fulfillment of the requirements for the degree of  
Doctor of Philosophy  
Graduate Division of Biological and Biomedical Sciences  
Neuroscience  
2017

## ACKNOWLEDGEMENTS

Teaching is a passion. I believe that it must be so as the remarks included in the acknowledgements section of a student's dissertation might well count among the most satisfying compensations for a job well. To be fair, teaching is absolutely necessary for the maintenance of human societies. Each treasured ember of knowledge must be conveyed onto a new vessel if it is to be used by future generations. That being said, the necessary good provided by a society's educators is only rarely reflected in the financial compensation afforded to our stewards of wisdom. And so, it must be something deeper—a self-motivated passion to do virtuous work, perhaps—that motivates the teacher in her selflessness.

Dr. Shella Keilholz, members of my committee, I thank you for granting me your insights into the mysteries of this squishy brain. Whereas anything at all might have molded these nerves and synapses over the past 6 years, your balanced advice has brought me to see, at once, the jaw-dropping wonder of the brain's complexity alongside its fundamental order. From this perspective, I might finally answer that fundamental existential question of life's purpose by positively echoing the weak anthropic principle that the purpose of life is only what we decide it is to be. Hopefully you have found my contributions worthy of your service.

Before entering graduate school, I never understood that my late father, Dr. Charles Billings, would often espouse a similar existential principle in quoting the following verse:

Life is real! Life is earnest!  
And the grave is not its goal;  
Lives of great men all remind us  
We can make our lives sublime,  
And, departing, leave behind us  
Footprints on the sands of time;

- Henry Wadsworth Longfellow

Nothing is truly fixed in this life save for its reality. Each person has their time to do with reality what they will. Dad, your life blazed a clear path through this seemingly random morass of epistemic realities. I am blessed to be able to follow in your footsteps.

And whereas confronting life's mercurial and impermanent nature can be stressful, the daily labor of so many people have gone to ensure that I might approach this perspective with more wonder than fear. This is especially the case for my mother, Martha Billings. Mom, thank for raising your family with the confidence to admit to what we do not know, and the curiosity to find the answers that we would seek.

I would also like to thank, as a whole if not by name, my friends and acquaintances among the students faculty and staff of Emory University. Ours is a village where, nestled in Atlanta's Druid Hills, a smile lines every face, and innovations pass effortlessly from hand to hand. It has been an honor and a privilege to work among you all.

Finally, to the love of my life, my wife, Megan Shelfer: your love sustains me through the worst of times and emboldens me when time crests. While none can know what the future brings, you have shown me that we can make it through anything if, standing side-by-side, we turn to face what awaits.

## Table of Contents

1.	Introduction .....	1
2.	Raw Brains: Preprocessing Strategies for Functional Connectivity .....	9
2.1.	Methods .....	13
2.2.	Results .....	16
2.3.	Discussion .....	26
3.	Connected Brains: Multiscaler and Multispatial Functional Connectivity .....	30
3.1.	Methods .....	33
3.1.1.	Data acquisition .....	33
3.1.2.	Preprocessing .....	33
3.1.3.	WPT Theory .....	34
3.1.4.	Wavelet packet transform (WPT) .....	36
3.1.5.	Wavelet packet entropy .....	37
3.1.6.	Multi-subject data .....	38
3.1.7.	Hierarchical clustering (HC) .....	39
3.1.8.	FC networks constructed via dendrogram pruning .....	41
3.1.9.	Comparing WPT-HC networks .....	44
3.2.	Results .....	45
3.2.1.	Wavelet packet entropy .....	45
3.2.2.	Variation in information (VarInf) across spectra .....	46
3.2.3.	Functional connectivity maps across spectra .....	49
3.2.4.	Functional connectivity maps across scan type .....	56
3.2.5.	Packets in low frequency oscillation range .....	60
3.2.6.	High frequency packets .....	62
3.2.7.	The broadband network .....	62
3.2.8.	Network stability after additional noise regression .....	63
3.3.	Discussion .....	64
3.4.	Limitations and Future Directions .....	69
4.	Mammalian Brains: Comparative Functional Connectivity .....	71
4.1.	Evolutionary Foundations of Comparative Neuroscience .....	75
4.2.	Methods .....	77
4.2.1.	Animal selection .....	77
4.2.2.	MRI acquisition .....	78

4.2.3.	Regions of Interest .....	79
4.2.4.	LFP Acquisition .....	79
4.2.5.	Data Analysis .....	80
4.3.	Results .....	82
4.4.	Discussion .....	84
4.5.	Limitations and Future Directions .....	86
5.	Dynamic Brains: Visualizations through multiscale embedding .....	87
5.1.	Methods .....	91
5.1.1.	Data Acquisition .....	91
5.1.2.	Data Preprocessing .....	91
5.1.3.	Spectral and Spatial Filtering .....	92
5.1.4.	Manifold Embedding .....	93
5.1.5.	Sub-Space Identification and Characterization .....	96
5.1.6.	Velocity Field .....	97
5.1.7.	Comparing Embeddings .....	97
5.1.8.	Real-Time Dynamics .....	98
5.1.9.	Permutation Testing for Labeling the Embedded map. ....	99
5.2.	Results .....	100
5.3.	Discussion .....	118
6.	Conclusions and Final Remarks .....	123
7.	References .....	126

## List of Figures

Figure 2.1	Global Signal Correlations - Preprocessing Strategies Set 1	17
Figure 2.2	Global Signal Correlations - Preprocessing Strategies Set 2	18
Figure 2.3	Global Signal Correlations - Preprocessing Strategies Set 3	19
Figure 2.4	Global Signal Correlations Segmented by Tissue Type	21
Figure 2.5	Global Signal Correlations Across Individuals	22
Figure 2.6	Global Signal Correlation Time Lags	23
Figure 2.7	Spatial Deviations from Zero Time Lag	24
Figure 2.8	Global Signal Spectrum	25
Figure 3.1	The Wavelet Packet Transform	37
Figure 3.2	Hierarchical Clustering	43
Figure 3.3	Network Entropy Across Wavelet Packets	46
Figure 3.4	Variation in Information among Spectrally Delimited Functional Networks	48
Figure 3.5	Example Functional Connectivity Dendrograms	49
Figure 3.6	Connectivity Networks - Set 1 - 112 Volunteers	50 - 51
Figure 3.7	Connectivity Networks - Set 2 - 30 and 5 Volunteers	52 - 53
Figure 3.8	Connectivity Networks - Set 3 - Volunteer #027 and #039	54 - 55
Figure 3.9	Connectivity Networks - Set 4 - 0.016 - 0.028 Hz	57
Figure 3.10	Connectivity Networks - Set 5 - 0.028 - 0.052 Hz	58
Figure 3.11	Connectivity Networks - Set 6 - 0.052- 0.100 Hz	59
Figure 3.12	Multispectral Functional Network Variation in Information across Scan Types	60
Figure 4.1	Rodent Default Mode Network	74
Figure 4.1	Rodent Gradient Echo - Echo Planar Image	78
Figure 4.1	Rodent Local Field Potentials	80
Figure 4.1	Inter-node Distances Across Spectra and Between Modalities	81
Figure 4.1	Multispectral Cross-Modal Network Correlations	82
Figure 5.1	Embedded Brain Dynamics during Rest and Task	101
Figure 5.2	Watershed Segmentation of Resting-State Dynamics	102
Figure 5.3	Watershed Segmentation of Task-Active Dynamics	103
Figure 5.4	Fifty Functional Networks from Independent Component Analysis	104
Figure 5.5	Cumulative Dwell Time Histograms	105
Figure 5.6	Embedded Brain Dynamics Segmented across Scan Types	106
Figure 5.7	Statistical Similarities among Scan-Segmented Embeddings	107
Figure 5.8	Structural Similarity Values between Scan-Segmented Embeddings	108
Figure 5.9	Visualization and Statistical Similarities among Event-Segmented Embeddings	109 - 110
Figure 5.10	Temporal Evolution of SOCIAL Task Dynamics	111

Figure 5.11	Close-up View of Temporal Evolution of SOCIAL Task Dynamics	112
Figure 5.12	A Labeled State Space of Brain Dynamics	113
Figure 5.13	Statistical Affinity of Experimental Conditions for each State-Space Regions	115
Figure 5.14	Contrasting Brain States Evoked by Contrasting SOCIAL Stimuli	116

## List of Tables

Table 2.1	Preprocessing Strategy Definitions	15
Table 3.1	Cophenetic Coefficients from Multiple Hierarchical Clusterings of Filtered BOLD Data	40

## 1. Introduction

information (n.) late 14c., informacion, "act of informing, communication of news," from Old French informacion, enformacion "advice, instruction," from Latin informationem (nominative informatio) "outline, concept, idea," noun of action from past participle stem of informare "to train, instruct, educate; shape, give form to" (**see inform**).

inform (v.): early 14c., "to train or instruct in some specific subject," from Old French informer, enformer "instruct, teach" (13c.) and directly from Latin informare "to shape, give form to, delineate," figuratively "train, instruct, educate," **from in- "into" (see in-(2)) + formare "to form, shape," from forma "form"** (see form (n.)). In early use also enform until c. 1600. Sense of "report facts or news, communicate information to" first recorded late 14c.

- etymonline.com

Brains are thought of as complex. For those who would like to understand the brain, this observation may seem daunting. But no real system is infinitely complex everywhere. Complexity is just another way of describing how many unique operations it takes for a system to come into being (Weisstein 2017). What at first may appear insurmountably complex often possesses guiding principles that may be incorporated to understand the properties of a complex system more simply (Papo, Buldú et al. 2014). The presence of guiding principles is especially true for natural living systems who self-assemble under the application of natural laws. The brain's complexity is embedded into an ordered scaling of constituent and constitutive parts: brain cells are a gestalt of chemicals, brain tissues are cellular aggregates, and individual brains find membership in a broader ecology inclusive of other uniquely patterned brains.

A founding figure in the world of information theory, Claude Shannon, may well have said of brains that of all the chaotic arrangements that chemicals can take, their form as brains requires fewer bits of information to describe than a more random arrangement of the same materials in the same volume (Shannon 2001). This is because anatomy is ordered. And the state of an ordered system, no matter how complex, is easier to detail than the state of the same material in a random distribution. Shannon proposed that the number of bits needed to fully characterize a system may be calculated as

$$H(X) = - \sum_{i=1}^k P(x_i) \log_2 P(x_i) \quad (1.1)$$

where  $P(x_i)$  is the overall probability of observing features like  $x_i$ .  $H(X)$  increases when there are more states, each with the same probability of occurring. Black holes, where matter and energy randomly cram together, contain the largest entropy (Bardeen, Carter et al.

1973, Greene 2004). The void, having only one state, approaches zero entropy, however briefly.

When faced with multiple ways to describe a system, it is often more useful to choose the lower entropy representations as doing so recategorizes states that appear dissimilar into a set of features that reflect something about the system's underlying form. Consider a familiar, though simplified and artificial example of the lowest entropy representation of a chord played on a piano. A high entropy representation of the chord might be the recording that digitizes continuous pressure readings from a microphone pickup into  $C_{microphone}$ , double-precision registers. A low entropy space might make use of the piano's intrinsic structure to describe its chord using  $C_{piano}$  notes. Even though the large range of values 64 bits can adopt allows double-precision recordings to represent many instantaneous pressures, each value's relative improbability of being reached makes the chord very costly to represent in bits. Because the number of combinations of notes,  $C'_{piano} < \left( \frac{\text{Number of keys}}{\text{Number of fingers}} \right) \approx \left( \frac{100}{10} \right) \cong 10^{13}$ , is much less than the recording's precision,  $C_{microphone} = 2^{64} \cong 10^{19}$ , distributing the chord across a basis set of notes uses fewer, more probable features than using a basis set of recorded amplitudes.

Similar arguments may be made for natural systems like brains, albeit with greater assurance. Whereas pianos possess structure at the scale of keys, hammers, and strings; they are the artifice of a secondary agent, a piano maker, who is often moved by some economic demand to turn raw materials into pianos. Natural systems, on the other-hand, self-assemble by way of fundamental physical processes. In the presence of a steady-state energy differential, microscopic entities may spontaneously arrive at a configuration that decreases the entropy generated during the exchange of energy (Nicolis and Prigogine 1977, Hidalgo 2015). The

entropy minimizing configuration may entrain adjacent entities to adopt similar configurations. Over time, this process tessellates outwards to build features at macroscopic scales from processes at microscopic scales. For example, pressure waves passing through a glass of water may cause otherwise Brownian fluid dynamics to develop standing waves at the water's surface.

The idea of complexity may be most familiar in artificial systems where it refers to the amount of unique actions an agent must perform to make the system. For self-assembled systems, complexity refers to the amount of unique arrangements substructures must adopt to realize the system's largest-scale feature(s). Complexity naturally emerges when many, well-ordered substructures emerge as a suite of functions in a superstructure. By constraining the arrangement of subparts into only those configurations that support multiple scales of emergent properties, complexity reduces a system's entropy.

Despite the growth of computational efficiencies according to Moore's exponential rate, fundamental statistical physics models are generally available only for systems on the order of a few thousand amino acids (Henry, Best et al. 2013). And although dedicated supercomputing systems have been built to replicate brains as complex as the mouse brain, these systems only mimic the functional input-output relations of individual neurons rather than the physical interactions among increasingly well characterized chemical constituents (Hsu 2014). There remains, therefore, a strong incentive to use measures of brain activity at some intermediate scale to understand the human brain's larger-scale emergent structure(s).

Functional Magnetic Resonance Imaging (fMRI) imaging offers such an intermediate perspective (Papo, Buldú et al. 2014). Because oxygenated hemoglobin is diamagnetic while deoxygenated hemoglobin is paramagnetic, and because blood-oxygen supply is tightly coupled to fluctuations in the brain's local metabolic load, it is possible to use magnetic

resonance images of the Blood Oxygen Level-Dependant (BOLD) contrast to infer changes in brain activity (Ogawa, Lee et al. 1990, Bandettini 2012). BOLD-fMRI measures are easily as precise as  $\sim 1 \text{ mm}^3$ , and faster than 1 Hz. The measure's non-invasiveness allows images to be acquired from the whole brain over an hour or longer. BOLD-fMRI thus provides a way to understand the intrinsic functional architecture of brain system from the perspective of whole brain cardiovascular support.

Model systems to utilize BOLD-fMRI are a topic of current development. One of the measure's earliest use cases regressed BOLD data against a general linear model to reveal which, if any, brain areas experience statistically significant deviations from baseline when volunteers engage in temporally delineated blocks of experimentally defined tasks (Belliveau, Kennedy et al. 1991). Because task related BOLD fluctuations account for only a small fraction, approximately 5%, of the brain's total metabolic demands while the remaining 95% of energy usage goes towards intrinsic brain signaling, a thorough characterization of spontaneous BOLD-fMRI was soon warranted (Raichle and Mintun 2006). Biswal *et al.* (1995) was first to demonstrate that temporal correlations in spontaneous, low-frequency BOLD signal fluctuations—termed the Functional Connectivity (FC) between regions—were strongest in the same motor regions as were preferentially activated during a motor task (Biswal, Yetkin et al. 1995). The experiment was a watershed moment, demonstrating that BOLD-FC may be as useful as task-based BOLD at determining the intrinsic functional organization of the brain (Fox, Snyder et al. 2005, Vincent, Kahn et al. 2008, Smith, Fox et al. 2009, Thomas Yeo, Krienen et al. 2011). BOLD-FC studies have since found wide application as a potential *pathoconnectomic* biomarker for neuro-psychological diseases such as addiction (Salomon, Karageorgiou et al. 2012, Lam, Wang et al. 2013), depression (Salomon, Cowan et al. 2011, Meng, Brandl et al. 2013), Parkinson's (Skidmore, Korenkevych et al. 2011),

Alzheimer's (Supekar, Menon et al. 2008, Wang, Zuo et al. 2013), schizophrenia (Alexander-Bloch, Gogtay et al. 2010, Bassett, Nelson et al. 2012), and others (Rubinov and Bullmore 2013).

Under the supposition that more parsimonious representations of the BOLD signal better reveal how the brain works, researchers have explored various lower entropy representational spaces for the BOLD signal. Each representation imposes certain assumptions about how the data should be ordered. For example: If the analyst believes that any globally present signal confounds discovery of preferential information sharing between brain sub-regions, then it is worthwhile to regress a global BOLD signal from the dataset as noise (Fox, Zhang et al. 2009, Murphy, Birn et al. 2013). If the belief is that simultaneous fluctuations in the BOLD signal may evidence shared information between regions, then an analyst might quantify that information sharing by defining a correlation distance metric between pairs of regions (Salvador, Suckling et al. 2005, Allen, Damaraju et al. 2012). Likewise, if it is believed that the BOLD signal is a mixture of linearly independent systems, one may multiply the dataset by an algorithmically defined un-mixing matrix to separate out the system's independent components (McKeown, Makeig et al. 1997, Majeed and Avison 2014).

The present dissertation research performs several operations on BOLD-fMRI data to transform this mesoscopic window of the brain into a form that more efficiently conveys the underlying structure and operation of whole brains. My central hypothesis is that the fundamental scaling behavior of self-assembled systems is preserved in the neuronal code and embedded in cranial hemodynamics. If this is the case, then scaled domains may offer more parsimonious and informative representational spaces to explore the brain's intrinsic organization.

Strong support for this hypothesis is conveyed by the observed scaling behavior of the BOLD signal itself. The BOLD signal bears a log linear relationship between power spectrum and frequency:  $\log S(f) = c + \gamma \log f$ ; alternatively,  $S(f) \sim 1/f^{-\gamma}$ . For the average BOLD signal in brains, the power law exponent,  $\gamma \cong 1$  (Bullmore, Fadili et al. 2004, He 2011). Such ‘1/f-type’ systems denote that the system’s high-frequency processes establish and maintain its low-frequency structure (Wornell 1993). The simplest 1/f-type systems are termed, ‘scale-free,’ that is, one observes rescaled versions of some elementary process, or fractal, at all observable scales. On the other hand, complex 1/f-type systems exhibit emergent properties at multiple scales (Ciuciu, Varoquaux et al. 2012, He 2014, Liu, Ward et al. 2014).

Scaling basis sets provide theoretically optimal domains for observing 1/f-type processes (Bullmore, Fadili et al. 2004, Ciuciu, Varoquaux et al. 2012). Such a basis provides a view of the system from its coarse features to its fine-scale features. However, scaling basis have been difficult to describe. One well-known scaling basis are the Fourier oscillators which represents systems as constricted of many standing waves, sines and cosines. In the artificial case of the piano chord, we may choose a range of Fourier oscillators,  $C_{Fourier}$ , directly matching the standing-wave frequencies of each note in  $C_{Piano}$ . Clearly then the entropy of a chord projected across a range of sines and cosines  $H(C_{Fourier}) = H(C_{Piano})$ .

Unfortunately, the Fourier transform’s kernels—the sinusoidal basis vectors—are defined over infinite lengths of time. While this assumption of infinite energy is fine as a first approximation for static systems—e.g., single chords sampled for time periods much longer than the period of the lowest note—the assumption breaks down for time-varying, dynamic system like the brain (Van Belleghem and von Sachs 2008, Buzsaki 2009). For non-stationary systems, a representational space bearing some amount of time-domain localization is critical. A class of functions known as *wavelets* develop especially useful multiscale bases (Daubechies

1992). Each kernel function reduces to zero over a finite range, thereby providing a temporal localization of the input signal's time-varying spectral content (Mallat 1999, Misiti, Misiti et al. 2013).

The present dissertation research advances the use of several data driven techniques, including the wavelet transform, to better represent and characterize intrinsic properties of the brain's organization and function. Techniques that may be applied in the raw BOLD signal's domain to improve the representation of spontaneous neuronal activity are addressed in Chapter 2. Chapter 3 identifies the degree to which multiscale wavelet representations produce unique information about the BOLD signal's long-term connectivity. Chapter 4 explores the degree to which the scaling behavior of spontaneous BOLD-FC is related to scaling properties of neuronal activity. Having sufficient evidence to support multiscale BOLD as a parsimonious domain to represent underlying neuronal energetics, Chapter 5 embeds our multiscale BOLD dynamics state space onto a 2-dimensional surface to identify how the brain generates each of a series of experimentally defined conditions.

## 2. Raw Brains: Preprocessing Strategies for Functional Connectivity

For studies utilizing the resting-state as a control condition, characterizing the intrinsic properties of the resting-state is necessary to understand experimental shifts from control conditions. Progress in the overall use of task-based fMRI depends on having a good understanding of the statistical organization of the resting state (Eklund, Nichols et al. 2016, Power, Plitt et al. 2017). Further, we know that when healthy mammals are at rest, their brains are still at work, processing self-relevant information (Hasenkamp, Wilson-Mendenhall et al. 2012, Lu, Zou et al. 2012, Spreng, Sepulcre et al. 2012, Barks, Parr et al. 2013). Characterizing the resting brain is thus a method to understand normative organizational and operational mechanisms.

Preprocessing strategies to explore the properties of spontaneous BOLD signals are presently a subject of research. This is especially true for the use of a Global BOLD Signal (GS) in noise regression. The GS is calculated as the average of the signal from all voxels across the term of a resting state fMRI (rs-fMRI) scan. It was originally proposed for minimizing noise in studies of inter-regional BOLD correlation, or Functional Connectivity (FC). Because the GS accounts for linear changes common to signal variations in all voxels, its Regression (GSR) from voxel time series should enhance the FC contrast among gray matter regions. Motivated by this rationale, a series of studies demonstrated the use of GSR to increase inter-network contrast (Fox et al., 2009; Murphy et al., 2009). However, GSR also forces some of the correlations within the brain to become negative (Murphy et al., 2009), creating problems in interpreting FC data.

Clearly there are many arguments to be made for and against GSR (see Murphy et al., 2013 for an excellent review). The use of GSR promotes spatial specificity in functional networks (Fox et al., 2009). Shirer et al. found that GSR reduced noise but at the expense of test-retest reliability (Shirer et al., 2015). In animal models, it has been used to control for

different levels of baseline blood flow and metabolism in the brain due to varying levels of isoflurane anesthesia (Liu et al., 2013). A positron emission tomography and rs-fMRI study in humans showed a similar effect, with the GS amplitude linked to changes in FDG metabolism and regional variance remaining relatively unchanged by baseline metabolism (Thompson et al., 2016). In one study that compared simultaneously recorded bandlimited power and BOLD correlation from two sites in the brain, GSR improved the fidelity of the BOLD signal to the changes in coordinated neural activity (Thompson et al., 2013b). These studies suggest that if the GS has a neural origin, it is unlikely to lie in the coordinated, time-varying modulations of neural activity that would ideally be detected with resting state MRI and that its removal may improve sensitivity to the signal of interest.

On the other hand, the BOLD GS amplitude is negatively correlated to EEG measures of vigilance in subjects with their eyes closed (Wong et al., 2013), suggesting that it might contain information about important neurophysiological processes that should not be discarded. Neural activity from a single electrode is correlated with the CBV-weighted signal from much of the brain, albeit at variable time delays (Scholvinck et al., 2010). Changes in broadband EEG power are associated with changes in GS at delays approximating the hemodynamic delay (Wen and Liu, 2016). Others have even shown that global activation can be detected in functional MRI provided enough averages are acquired (Gonzalez-Castillo et al., 2012). These findings all suggest that the GS is more than a nuisance. Furthermore, GSR can distort differences between groups (Saad et al., 2012). The GS itself can distinguish patient groups from healthy controls (Hahamy et al., 2014; Yang et al., 2014), though some of these differences may arise from changes in head motion or in vascular tone.

A brief perusal of these findings raises the question of exactly what constitutes the global BOLD signal. Because it is calculated as the sum of signals from all brain voxels,

patterns of widespread activation might provide substantial contributions to the GS. For example, the quasiperiodic spatiotemporal patterns (QPPs) of BOLD fluctuations that have been reported previously (Majeed et al., 2011; Thompson et al., 2014) exhibit large-scale spatial structure involving periodic activation and deactivation of cortical nodes in the default mode network (DMN) and task positive network (TPN), with propagation of activity along the cortex between nodes (Majeed et al., 2011, 2009). QPPs are linked to infraslow activity (Pan et al., 2013; Garth John Thompson et al., 2014) and appear to be separable from the aperiodic changes that are expected to be more cognitively relevant (Garth J Thompson et al., 2014; Thompson et al., 2015). Both infraslow electrical activity and TPN/DMN activity have been linked to performance, particularly on tasks with a strong attentional component (Fox et al., 2007; Kelly et al., 2008; Monto et al., 2008; Thompson et al., 2013a). Moreover, recent work shows that the phase of the QPP predicts reaction time on a simple vigilance task (Abbas et al., 2016). When considered in the context of the growing body of work linking GS and vigilance (Wong et al., 2016, 2013), this suggests that part of the GS may arise from these widespread quasiperiodic patterns of activation and deactivation. The potential link between QPPs and the GS motivated a more thorough examination of the characteristics of the global BOLD signal. Are the two features the same or do they constitute two unique contributions to BOLD FC?

The present study addresses questions about the origins of the BOLD GS by examining the spatial distribution of the global BOLD signal, the time of peak correlation between the GS and the BOLD signal from each voxel, and the relative contribution to the GS from different tissue types. The findings suggest that QPPs are not a major contributor to the global BOLD signal, and confirm that the global BOLD signal is not so global after all.

## 2.1. Methods

*Data Acquisition.* Neuroimaging data were downloaded through the 1000 Functional Connectomes Project ([https://www.nitrc.org/projects/fcon\\_1000/](https://www.nitrc.org/projects/fcon_1000/)) (Milham 2013). The data were acquired as part of the *Enhanced Rockland Sample Multiband Imaging Test-Retest Pilot Dataset*, uploaded by the Nathan Kline Institute for Psychiatric Research (Nooner, Colcombe et al. 2012, Nathan Kline Institute for Psychiatric Research 2013). A total of 31 volunteer datasets were used for the present study. Volunteers were  $44 \pm 18$  years old, with 21 females and 10 males. Thirty volunteers were right-handed; one had no preference.

Whole brain images were acquired on a 3T Siemens Magnetome TriTom (multiband EPI; TR 645 ms; TE 30 ms; 40 slices; FOV 22.2 cm x 22.2 cm; 3 mm isotropic voxels; 900 images). A 32 channel anterior/posterior head coil facilitated multiband EPI imaging at high temporal resolution. A MPRAGE scan was acquired to facilitate alignment (TR 1900 ms; TE 2.52 ms; 176 slices; FOV 25 cm x 25 cm; 1 mm isotropic voxels).

*Standard preprocessing.* A series of preprocessing steps were carried out over the entire data set to bring data points into temporal and spatial alignment. These steps were conducted using revision 6470 of the Statistical Parametric Mapping MATLAB toolbox (Friston, Ashburner et al. 2011). Slice timing mismatches were corrected per each slice's multiband acquisition time. Within-scan images were realigned to correct for movement between repetitions. Each scan's mean realigned image was co-registered to the volunteer's structural image. Structural images were segmented into 5 tissue classes: gray matter, white matter, cerebrospinal fluid (CSF), bone, and soft tissue. A warping matrix was evaluated and used to normalize each scan from subject space to MNI space. Finally, functional images from all volunteers are realigned to the group mean, further increasing the spatial overlap between volunteers.

*Variable preprocessing:* It is common practice to implement several additional preprocessing steps on voxel time series prior to subsequent analysis. Such voxel-wise normalization procedures have a large effect on the resultant GS. Therefore, the present study examines GS after applying different combinations of these preprocessing strategies. Table 1 provides a list and a short description of the variable preprocessing steps. Because the order of preprocessing operations influences the final data product, the present study adopted the following formalisms when applying multiple preprocessing strategies: time series normalization was conducted before noise regression, multiple noise signals were simultaneously regressed from scans.

*Data analysis.* After preprocessing, a GS was calculated for each scan as the mean signal from all image voxels. This signal was cross-correlated against all other voxel time-series to assess any periodic relationships between the GS and individual voxel time-series. GS Correlation (GSC) coefficients at lag time,  $m$ , were calculated as  $R_{gv_i}(m) = E\{v_i(t + m)g(t)\}$ , where the functional  $E$ , is the expected value,  $v_i(t + m)$ , is the  $i^{\text{th}}$  voxel signal at time  $t+m$ , and  $g(t)$  is the GS at time  $t$ . Notice that the correlation is only a vector product and lacks normalization constants. This non-normalized correlation coefficient preserves information about the relative magnitudes of the underlying signals after each preprocessing strategy. Graph representations of study results are scaled to the minimum and the maximum of this range. This strategy provides additional information to compare correlation coefficients through a series of rescaling procedures.

Table 2.1: Preprocessing Strategy Definitions

<b>STEP</b>	<b>DESCRIPTION</b>
<b>TIME-SERIES NORMALIZATION</b>	
<b>NONE</b>	No additional preprocessing steps
<b>DEMEANING</b>	The mean voxel signal is subtracted from each time point
<b>DETRENDING</b>	A linearly increasing vector and a vector of ones are regressed from each voxel time series.
<b>Z-SCORING</b>	Demeaned voxel time series are divided by their variance
<b>NOISE REGRESSION</b>	
<b>MOVEMENT REGRESSION</b>	3 translational, and 3 rotational movement parameters, and their squares, are regressed from voxel time-series
<b>CSF/WM REGRESSION</b>	The first four principal components from cerebro-spinal fluid and white matter voxel time-series are regressed from all voxel time-series

## 2.2. Results

The global BOLD signal exhibited substantial correlation with voxels throughout the brain, particularly in the cortical grey matter. Figure 2.1 shows group average correlation strength of each voxel with the GS across a range of voxel-wise preprocessing strategies. When voxel time series were not normalized, the GS exhibited strong correlations in peripheral tissues, particularly over an anterior and a posterior zone. After removing signal means, maximal correlation with the GS was found at the head's periphery. Normalizing voxel signals to unit variance generated increased GSC deep into the brain's gray matter.

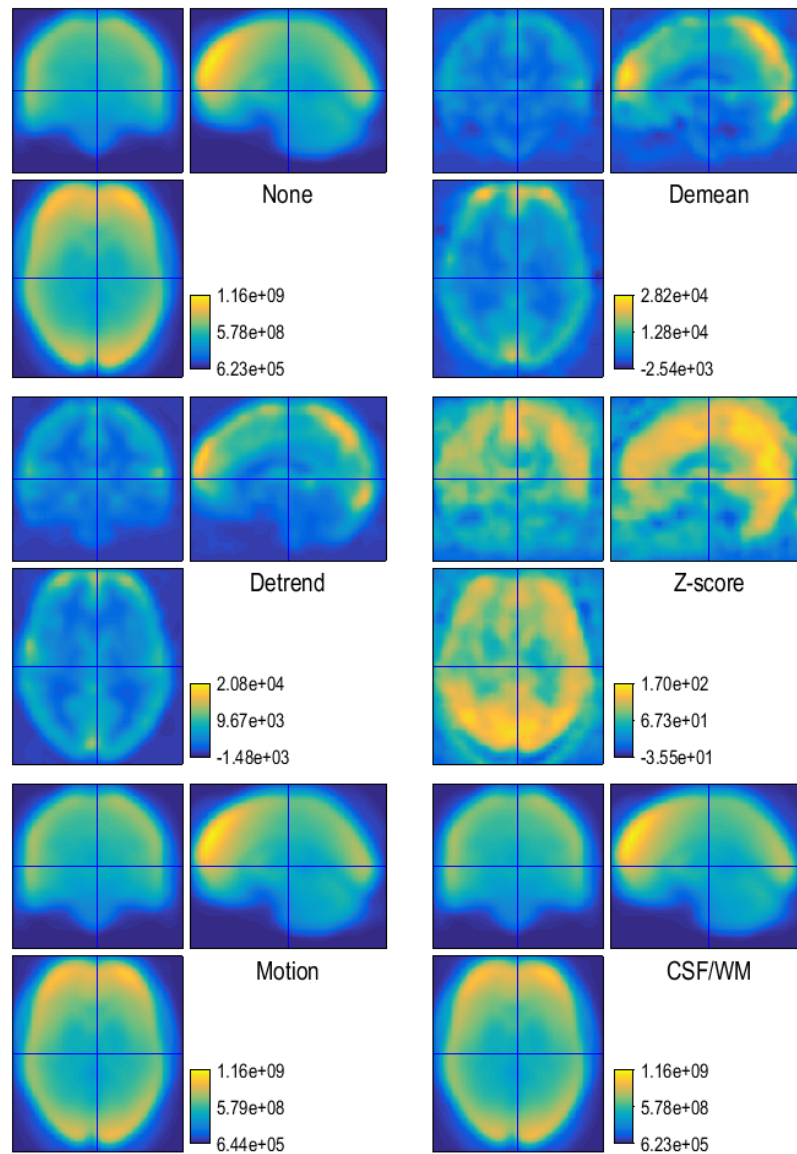


Figure 2.1: The correlation between voxel signals and the global signal (GS) is shown after various preprocessing strategies: minimal processing, demeaning, detrending,  $z$ -scoring, motion regression, and CSF/WM regression.  $Z$  scoring reduces the contribution from the anterior and posterior hot spots. After  $z$ -scoring, the contributions come primarily from the grey matter, with a particularly strong correlation between occipital grey matter and the GS.

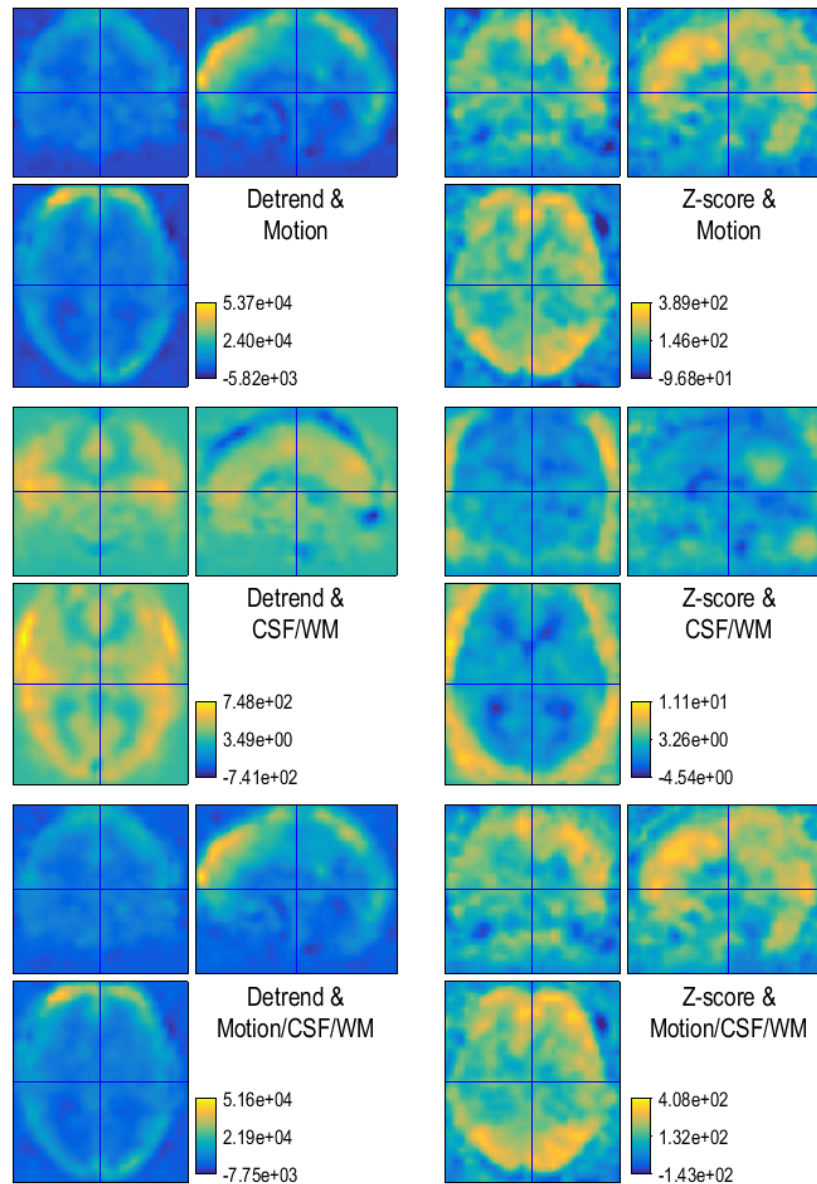


Figure 2.2: Voxel wise correlation with the global signal is shown after combining at least two preprocessing strategies: either of two types of time series normalization strategy—detrending or z-scoring—with combinations of at least one type of noise regression strategy—motion regression and/or CSF/ WM regression.

Figure 2.2 displays a series of correlation maps for datasets with various combinations of time series normalization and noise regression. Motion regression had the largest impact on correlation with fronto-dorsal and posterior tissues. On the other hand, CSF/WM regression largely inverted GS correlations. After simultaneous regression of CSF/WM and

motion noise signals from normalized data, the GSC produced is very similar to the correlation map after motion correction alone.

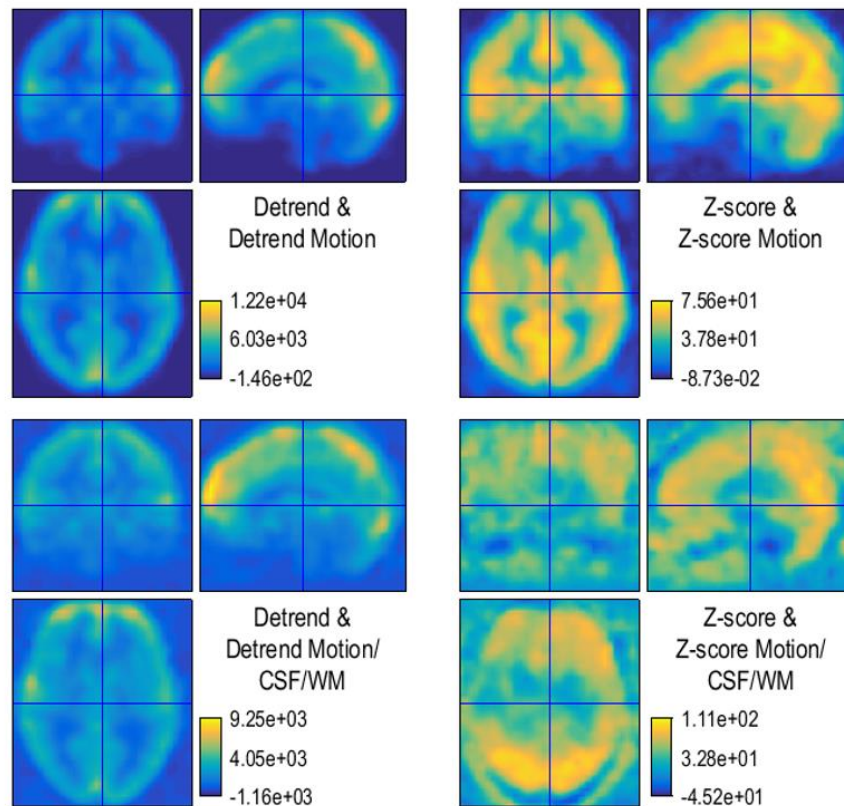


Figure 2.3: The effect, on voxel-wise global signal correlation (GSC), of normalizing volunteer motion parameters before regression is shown for the relevant preprocessing strategies from figure 2.2. Localization of GSC to the gray matter after normalization by both detrending and z-scoring is a strong outcome measure in support of discarding information about motion's absolute values.

The lack of a clear effect on the GSC distribution after simultaneous regression prompted an additional set of comparisons that normalized the motion time-series before motion regression (figure 2.3). Without CSF/WM regression, both normalization steps localize GSC to the gray matter. Maximal correlation is widely distributed across gray matter after z-scoring, but is localized to a few hot spots after detrending. CSF/WM regression blurs the distribution of GSC. The preference shown for gray matter is for the z-scored data set.

To better show the contributions to the GS from various tissue classes, figure 2.4 segments the group average time series normalized and noise regressed datasets across three

tissue masks: grey matter, white matter, and CSF. These and subsequent results focus on just two of the best performing preprocessing strategies detrending and detrended motion regression (conservative normalization) and z-scoring with z-scored motion regression (strong gray matter localization, strong denial that signal magnitudes are meaningful). CSF/WM regression was not further investigated as it's quantitative overlap with the GS makes the two techniques direct alternatives to one another rather than complimentary regression strategies.

Figure 2.5 provides an indication of the variation in the GS between individuals. After detrending and motion regression, prominent variations in the GS overlap rostral and caudal hot spot observed from the un-normalized correlation distributions in figure 2.1. This likely reflects the effects of large magnitude fluctuations from the head coil's sensitivity profile as the region extends from peripheral CSF into the gray matter. After z-scoring, large variations in GSC are observed in peripheral white matter as well. For both normalization strategies, the largest GSC variation occurs in the regions having the largest GSC magnitude after detrending and detrended motion correction.

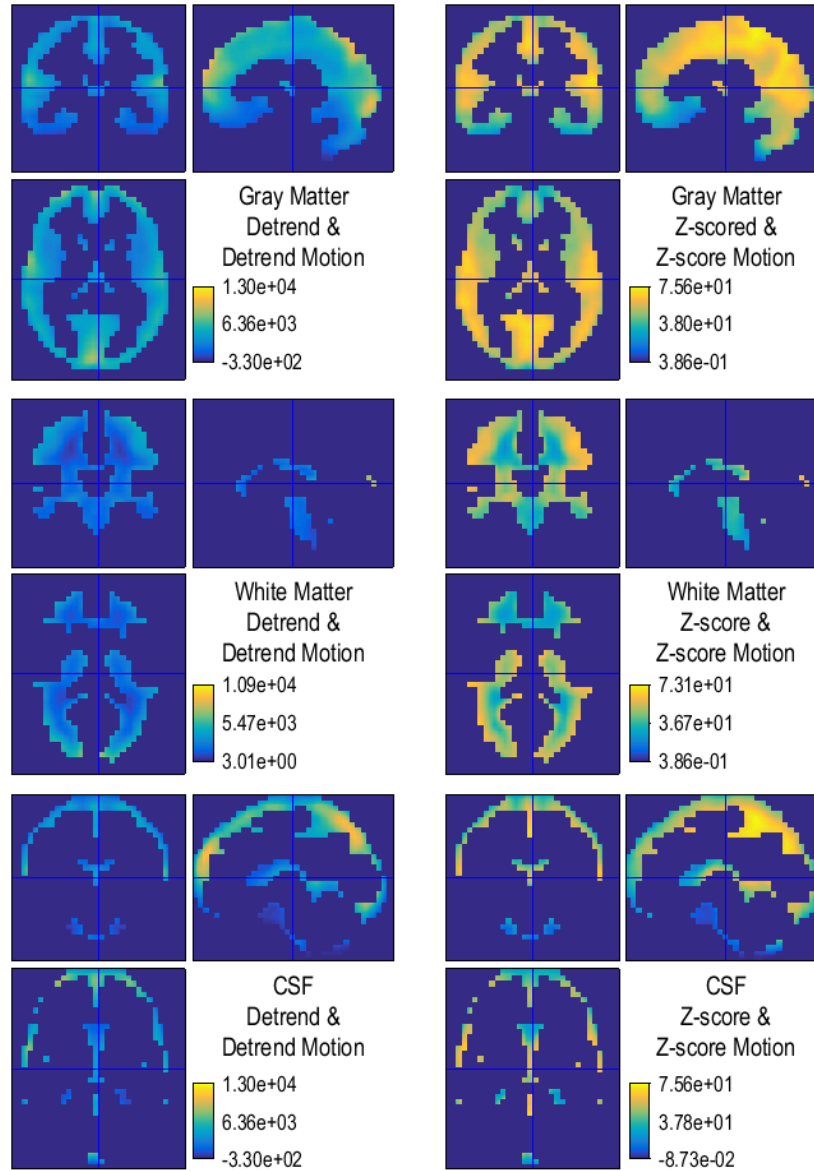


Figure 2.4: Correlation between the detrended, motion-regressed global BOLD signal and voxel-wise signals have, here, been separated by tissue type. After detrending and motion correction, the strongest correlation was in the CSF, and, grey matter. When data are normalized to unit variance (z-scored) the global signal was correlated with deeper white matter tissues as well.

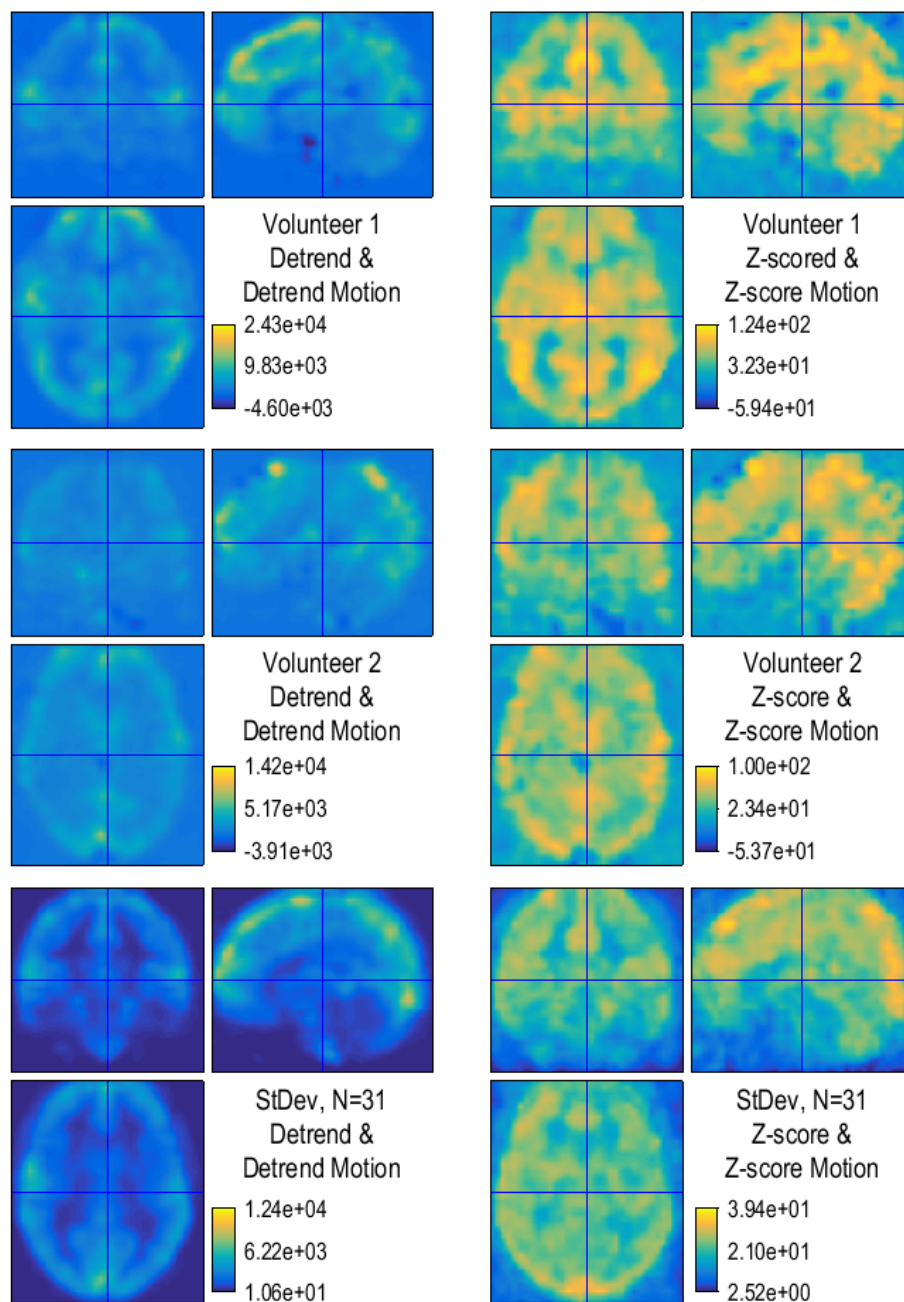


Figure 2.5: To gain an idea of the variation of global signal correlation (GSC) across volunteers, the GSC is displayed for volunteers 1 and 2. The standard deviation of GSC values is also displayed.

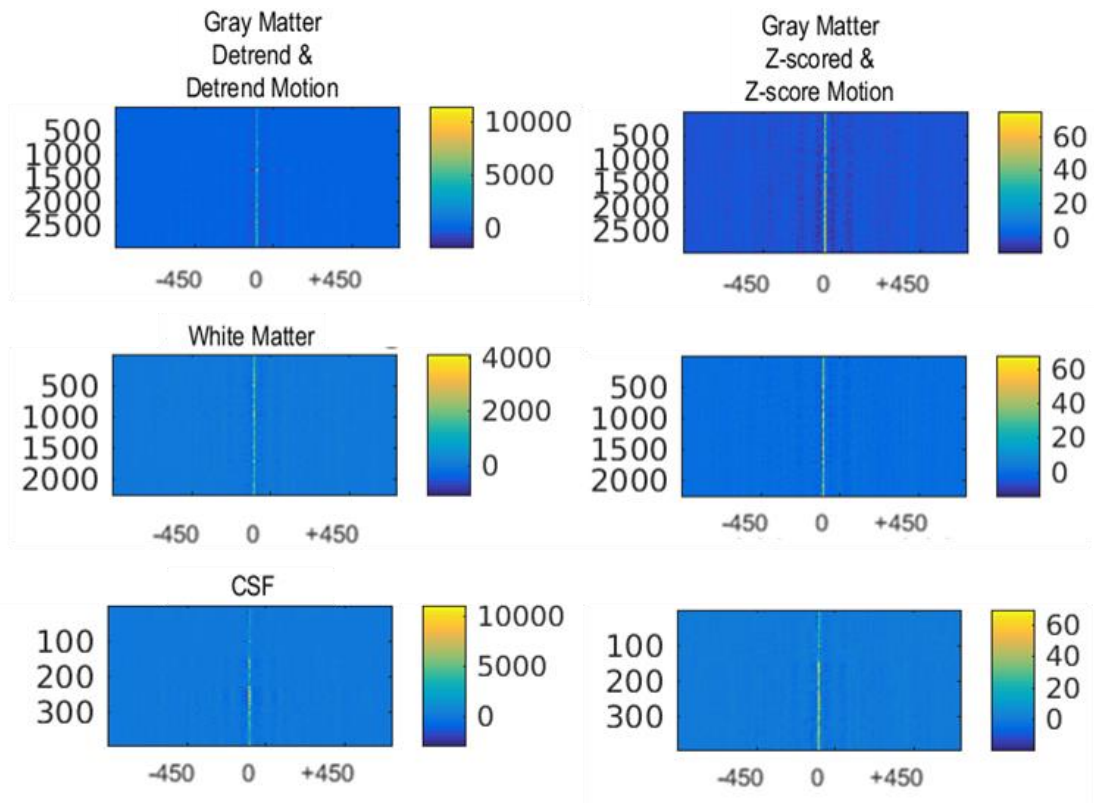


Figure 2.6: The time lag for maximum correlation between the global BOLD signal and each voxel was centered around 0 lag for all brain tissue classes. Some periodicity exists in cross-correlation

Figure 2.6 plots the non-normalized cross-correlation between the GS and each voxel as a function of time lag and of tissue class. By far, the strongest correlation is observed at zero time lag for all tissue classes, and both preprocessing strategies. Some periodicity in GSC is observed, especially in the gray matter after z-scoring.

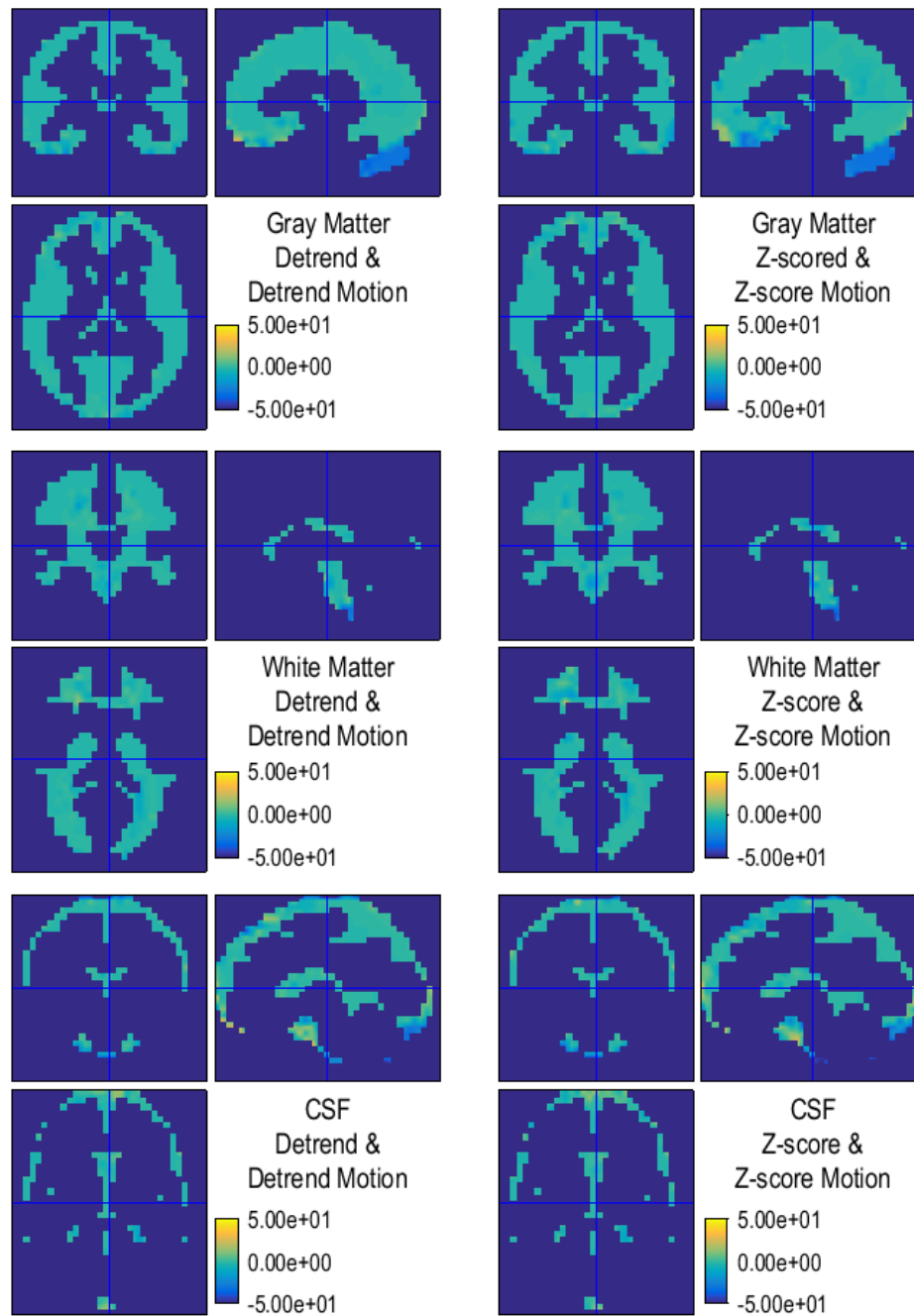


Figure 2.7: Time lag for maximum correlation between the global BOLD signal and each voxel. No pattern of delay was observed. Each lag unit is equivalent to 0.72 seconds. Lag range is limited to  $\pm 5$  lag units ( $\pm 3.6$  s) to highlight deviations from zero lag.

Maximum GSC may not lie precisely at zero lag time in all places. Figure 2.7 details the spatial distribution of lag time generating maximal GSC. Slight positive and negative

deviations were observed in ventral gray matter. No spatial or temporal structure that corresponded to cortical QPPs was observed.

The GS power spectrum, in both the detrended and the z-scored case, is smoothly distributed, with maximal amplitude at low frequencies (figure 2.8).

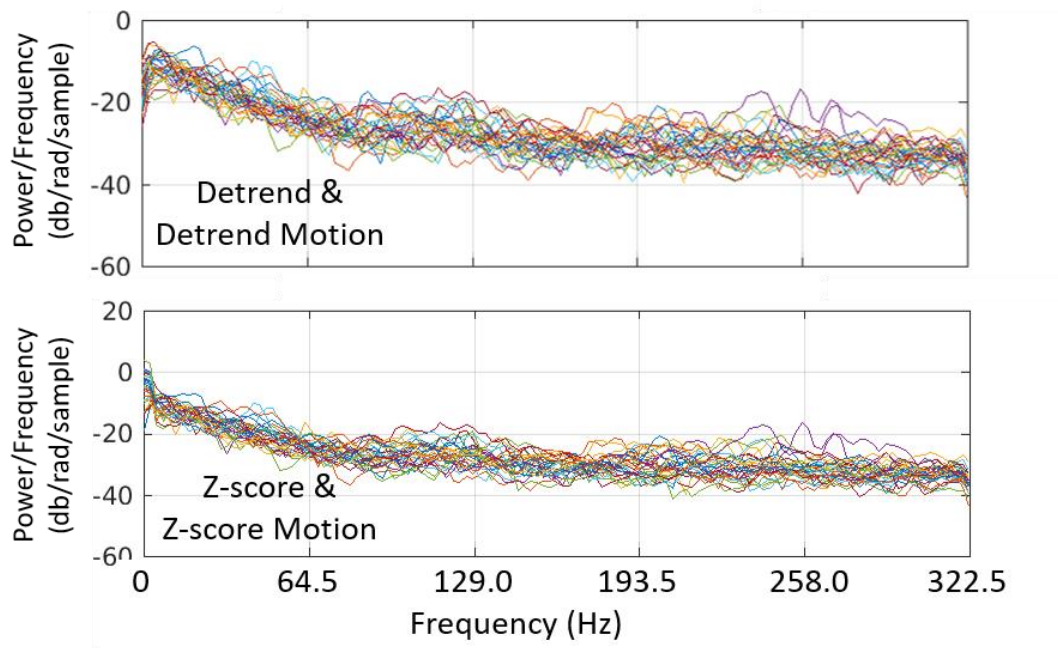


Figure 2.8: Frequency spectrum of the global signal from each volunteer. Plots differ based upon the labeled preprocessing strategy.

### 2.3. Discussion

*Spatial distribution of global signal.* The global BOLD signal contains strongest contributions from frontal and occipital areas. These regions likely correspond to the head coil's sensitivity profile. This distribution was maintained after noise regression, a fact that highlights the impact of the raw BOLD signal magnitude on latter processing strategies. The simple removal of the mean signal from each voxel reduces this bias. Even so, GSC remains strongest at the periphery, in agreement with previous research (Fox et al., 2009). The localization of GSC to hot spots at the boundary between CSF and gray matter denote the presence of large signal variance at the CSF/gray matter tissue boundary. This is in contrast to the dispersion of correlation deep into grey matter after z-scoring. The imposition of unit signal variance across the brain via z-scoring reduces the contribution from the high variance voxels and results in a fairly uniform GS contribution from the grey matter.

Noise regression also impacts the spatial distribution of the global BOLD signal. CSF/WM regression and GSR are overlapping procedures; with CSF/WM regression being equal to the GS minus an aggregate signal from non-CSF/WM image regions. The noted inversion of the spatial distribution of correlation intensities after CSF/WM regression is therefore not surprising. The CSF/WM correlation map represents a focal map of contributions from gray matter, bone, and soft tissue to the GS. Whereas the CSF/WM signal is a subset of the GS, the motion regressor is calculated from a series of rigid body manipulations. Thus, motion regression introduces outside information that is picked up during subsequent calculations of the GS. The mean magnitude of the motion regressor is appreciable while the mean magnitude of the CSF/WM signal fluctuates around 0, dual regression of motion and CSF/WM is strongly weighted on the motion regressor's side. This effect is minimized by normalizing motion regressors in the same way as the data are

normalized. Many studies have argued that additional parameters from motion, respiration, heart beating, and other yet-identified processes must be better characterized in order to more optimally clean global BOLD fluctuations from complex neuronal profiles (Power et al., 2012)(Power, Plitt et al. 2016).

From these data it is clear that even after intensity normalization and motion parameter regression, the GS, while widespread in all subjects, is not exactly global. The localization to the superior regions of the brain could arise from a combination of greater coil sensitivity in those locations, as well as from partial volume effects at the CSF/gray matter tissue boundary. Even after Z-scoring, the GS is primarily present in grey matter, with less contribution from white matter and subcortical areas.

*Role of QPPs in the global signal.* We did not observe evidence of large scale patterns or QPPs in the GS (Amemiya et al., 2016; Majeed et al., 2011). We expected that strong contributions from these patterns would result in 1) dominance of the DMN or TPN as contributors to the GS and/or 2) a spatially-structured distribution of lag times that mapped to the known propagation of the patterns. Because neither of these were observed, we conclude that QPPs are not major contributors to the GS and that GSR should not reduce sensitivity to the patterns. This is in line with our previous finding that infraslow electrical activity was correlated to the BOLD signal regardless of whether GSR was applied (Pan et al., 2013). The lack of a spatially-structured time lag is also in accordance with a NIRS/MRI study that found that hemodynamic lags varied by a second or less across the brain (Erdoğan et al., 2016).

*Vascular contributions.* So what is left in the GS after motion parameter regression? One possibility is a vascular component. Tong and de Frederick have published multiple papers showing that a peripheral measurement of hemodynamics is correlated with the BOLD signal

over large swaths of the brain at different time lags (Tong and Frederick, 2010, 2014). These fluctuations could conceivably contribute to the global BOLD signal. Other vascular processes could also contribute. Vasomotion involves vascular oscillations at frequencies of  $\sim 0.1$  Hz and remains poorly understood (Mayhew et al., 1996; Osol W., 1988). Mayer waves, related to sympathetic nervous system oscillations, are another potential source of GS oscillations (Julien, 2006). Future studies with other hemodynamic contrasts (CBV, CBF) may help to shed light on the relative contribution of the vasculature to the BOLD GS.

*Neurophysiological origins.* Recent work supports a neurophysiological origin for at least some portion of the GS. A PET and rs-fMRI study in humans showed that the GS amplitude was linked to changes in baseline FDG metabolism, while regional variance remaining relatively unchanged by baseline metabolism (Thompson et al., 2016). In animal models, GSR has been used to control for different levels of baseline blood flow and metabolism in the brain due to varying levels of isoflurane anesthesia (Liu et al., 2013). Changes in broadband EEG power are associated with changes in GS at delays approximating the hemodynamic delay (Wen and Liu, 2016). A number of EEG-MRI studies, particularly by Dr. Thomas Liu's group, have shown that the GS amplitude is related to EEG measures of vigilance (Wong et al., 2016, 2013). Thus the GS may reflect large-scale modulation of brain activity related to fluctuations in arousal or vigilance levels. In a study that compared simultaneously recorded bandlimited power and BOLD correlation from two sites in the brain, GSR improved the fidelity of the BOLD signal to the changes in coordinated neural activity (Thompson et al., 2013b). This suggests that its removal may improve sensitivity to the coordinated, time-varying modulations of neural activity that would ideally be detected with resting state MRI.

While various hotspots appear in the contribution of individual voxels to the global BOLD signal, in general the entire cortical grey matter contributes more strongly than the

white matter or subcortical regions, something that is particularly apparent after motion and physiological noise are minimized. Z-scoring makes this particularly prominent. This supports a potential global but neural source as one contributor to the global BOLD signal, and suggests that studies of the GS as a surrogate for widespread neural activity might wish to perform these processing steps to increase sensitivity to the hypothetical neural component.

### 3. Connected Brains: Multiscaler and Multispatial Functional Connectivity

Information about the brain's spatial scaling may be obtained by parcellating the anatomy into FC networks at finer scales. For instance, Buckner et al. used ROI-based FC-fMRI to identify homotopic maps of the body and the cerebrum (excluding the visual cortex) in a pair of regions in the cerebellum (Buckner 2011). Early successes with independent component analysis (ICA) for whole-brain FC-fMRI at low model orders inspired Kiviniemi *et al.* (2009) to parcellate the brain into as many as 42 independent networks at higher ICA model orders (Calhoun, Adali et al. 2001, Kiviniemi, Starck et al. 2009). Other studies have observed the choice of model order to have a direct bearing on the capacity to identify pathology related differences in FC-fMRI networks (Abou Elseoud, Littow et al. 2011).

Scaling may play an analogous role in brain physiology via trends in brain activity measures acquired through a span of time. In terms of fundamental brain signaling events, the minimum time between successive potentials is limited to  $\sim 1$  ms by an absolute refractory period in voltage gated sodium channels (Mitra and Bokil 2008). For mesoscopic measures, such as BOLD FC, individual neuronal activations combine to produce correlated signal properties at multiple frequencies. For instance, Kalcher *et al.* (2014) demonstrated large FC network variations among tissue types and grey-matter seed-regions when tissues and ROIs are filtered into different passbands ( $<0.1$  Hz; 0.1–0.25 Hz; 0.25–0.75 Hz; 0.75–1.4 Hz) (Kalcher, Boubela et al. 2014). Wu *et al.* (2008) showed that cortical networks tend to organize in the frequency range between 0.01-0.06 Hz while limbic networks organize between 0.01 – 0.14 Hz (Wu, Gu et al. 2008). Chang and Glover (2010) showed that the frequency band harboring maximal correlation strength within the default mode network changed over time (Chang and Glover 2010).

Given the multi-scale organization of brain networks and the spectral variability of their signals, it is valuable to pursue FC methods that autonomously segment brain data into

discrete frequency domains and nested spatial scales (Deco, Jirsa et al. 2011, Hutchison, Womelsdorf et al. 2013, Keilholz, Magnuson et al. 2013). To this end, the present study incorporates the wavelet packet transform (WPT) for ordered spectral segmentation of FC-fMRI, and hierarchical clustering for the autonomous aggregation of individual voxels into progressively more extended networks. We refine functionally relevant networks from this multi-scale representation through the use of two information theory-based classifiers: wavelet packet entropy for the identification of high-entropy domains, and variation in information to group similar spectral domains at a particular spatial scale. These data-driven methods result in the generation of well-formed, whole-brain FC-fMRI networks among groups and individuals.

## 3.1. Methods

### 3.1.1. *Data acquisition*

Neuroimaging data was downloaded from the 1000 Functional Connectomes Project website (Milham 2013), specifically, the *Enhanced Rockland Sample Multiband Imaging Test-Retest Pilot Dataset* uploaded by the Nathan Kline Institute for Psychiatric Research (Nooner, Colcombe et al. 2012, Nathan Kline Institute for Psychiatric Research 2013). This dataset was chosen as it was one of the first to make use of multiband imaging (Feinberg, Moeller et al. 2010) to produce BOLD scans with short repetition times,  $TR = 0.645$  s. Shorter  $TR$ 's enhance spectral resolution (Feinberg, Moeller et al. 2010, Moeller, Yacoub et al. 2010, Lee, Zahneisen et al. 2013).

Study data were derived from 112 individuals randomly chosen from the NKI Enhanced Rockland sample (n. female = 74, n. right handed = 95, mean age = 46.16 y, std. age = 19.89 y). These data include two 10 minute long resting-state fMRI scans and their associated 1 mm<sup>3</sup> structural images. With a  $TR$  of 0.645 s and 900 images per run, the sampled data span frequencies in the range between 0.003 Hz and 0.775 Hz.

### 3.1.2. *Preprocessing*

Spatial data preprocessing was conducted in MATLAB (Mathworks, Natick, Massachusetts), and the Statistical Parametric Mapping (SPM8) MATLAB software package (Friston, Ashburner et al. 2011). FC-fMRI data were first thresholded at an empirically derived value to exclude non-brain areas. The within-scan images were then realigned to correct for movement. The mean realigned images were then co-registered with the volunteer's structural image. Structural images were segmented and co-registered with the MNI template. The resulting warping matrix was used to normalize functional images into MNI space. Lastly,

functional images from all volunteers are realigned to their group mean, further increasing the spatial overlap between volunteers.

### 3.1.3. *WPT Theory*

The WPT is an expansion on multiresolution analysis where square integrable functions,  $f$ , are described as the limit of successive approximations of smoothed version of  $f$ . The definition of a multiresolution analysis proceeds as follows: Construct the vector space of real valued square integrable functions,  $L^2\mathbb{R}$ . Observe that this space may be assigned as equivalent to the union of a set of subspaces,  $\bigcup_{d \in \mathbb{Z}} V_d$ . If the various vector spaces,  $V_d$ , are a family of embedded closed subspaces

$$\dots \subset V_2 \subset V_1 \subset V_0 \subset V_{-1} \subset V_{-2} \dots, \quad (3.1)$$

then the subspace affects a multiresolution decomposition of  $L^2\mathbb{R}$ . the  $V_d$ . Note that the complete intersection of  $V_d$  is vanishingly small,  $\bigcap_{d \in \mathbb{Z}} V_d = \{0\}$ .

Information lost when going from a  $V_{d-1}$  to  $V_d$  can be accessed in the orthogonal space,  $W_d$ . The unsmoothed space  $V_{d-1}$  is thus equivalent to the direct sum,  $V_d \oplus W_d$ . We can capture the information in each orthogonal subspace with a pair of functions,  $\{\psi_{dk}; n \in \mathbb{Z}\}$  and  $\{\varphi_{dk}; n \in \mathbb{Z}\}$ . The  $\psi$  functions, termed the wavelet functions, span  $W_d$ . Likewise, the  $\varphi$ , termed the scaling functions, span  $V_d$ . They are related to each other through the recursive relations:

$$\phi_d(x) = \sum_k h_k \phi_{d-1}(-k) \quad (3.2)$$

and

$$\psi_d(x) = \sum_k (-1)^k h_{k+1} \phi_{d-1}(k) \quad (3.3)$$

If appropriate choices for  $h$  are made, then  $\phi$  is compactly supported by the vector,  $h$ . Thus:

$$h(k) = \sqrt{2} \int dx \phi_d \phi_{d-1}. \quad (3.4)$$

Likewise,  $\psi$  is defined by  $\phi$  and the quadrature mirror of  $h$ :  $g(k) = (-1)^k h(-k + 1)$ , and:

$$g(k) = \sqrt{2} \int dx \psi_d \phi_{d-1}. \quad (3.5)$$

The WPT filtering schema is a realization of successive applications of a filter,  $h$ , and its quadrature mirror,  $g$ . In practice,  $h$  is a low pass filter and  $g$  is its high pass quadrature mirror. The WPT iteratively applies the  $h(k)$  and  $g(k)$  to downsampled versions of  $f$ ,  $f(2^{-d} \cdot)$ . Note that the functions,  $f$ , are elements of  $V_d$  if and only if upsampled versions of  $f$ ,  $f(2 \cdot)$ , are elements of  $V_{d-1}$ . The process of downsampling between each filtering step accomplishes two things: 1) downsampling inflates the Fourier domain representation of the signal such that the filters,  $h$ , and  $g$ , may be used in accomplishing successive half-band filtering operations on previously filtered signals; and 2) according to the Nyquist rule, downsampling reduces two filtered signals to the minimum number of data points needed to reconstruct  $f$ . A pictorial depiction of the WPT process is provided in figure 3.1. A variety of  $h(k)$  exist, each with unique properties. Increasing the dimensionality of a particular  $h(k)$  (i.e., its number of vanishing moments, or “taps”) extends it over the domain of  $x$  while sharpening the filter attenuation and flattening the passband (Tian and Wells Jr 1996).

### 3.1.4. *Wavelet packet transform (WPT)*

The WPT is essentially a filter bank covering  $d \in [0, 1, 2, \dots, \infty]$  sets of  $2^d$  evenly segmented passbands. The application of the WPT filtering schema  $d$  times is called the ‘depth’ of WPT filtering. An ordered set,  $p \in [0, \dots, 2^d]$ , number the frequency order of packets from passbands including the signal’s DC components ( $p = 0$ ) to a passband including the signal’s fastest components ( $p = 2^d$ ). The range of each filter’s passband is roughly equivalent to  $\left[ \frac{p(f_s/2)}{2^d}, \frac{(p+1)(f_s/2)}{2^d} \right]$  (Hz), where  $f_s$  is the sampling frequency. The filtered data existing at depth  $d_i$  and position  $p_j$  is given the shorthand notation ‘ $Dd_iP_j$ ’. Thus, the D0P0 signal is the broadband signal. The D2P0 signal is quarter-band signal covering the lowest frequencies, and the D2P3 signal is the quarter-band signal covering the highest frequencies. For more details on WPT theory and usage, the reader is referred figure S1, the works of Daubechies (Daubechies 1988, Daubechies 1992), Mallat (Mallat 1989, Mallat 1999), and Meyer (Coifman, Meyer et al. 1992, Meyer 1993), as well as the technical notes of M. Misiti, Y. Misiti, Oppenheim, and Poggi (Misiti, Misiti et al. 2013).

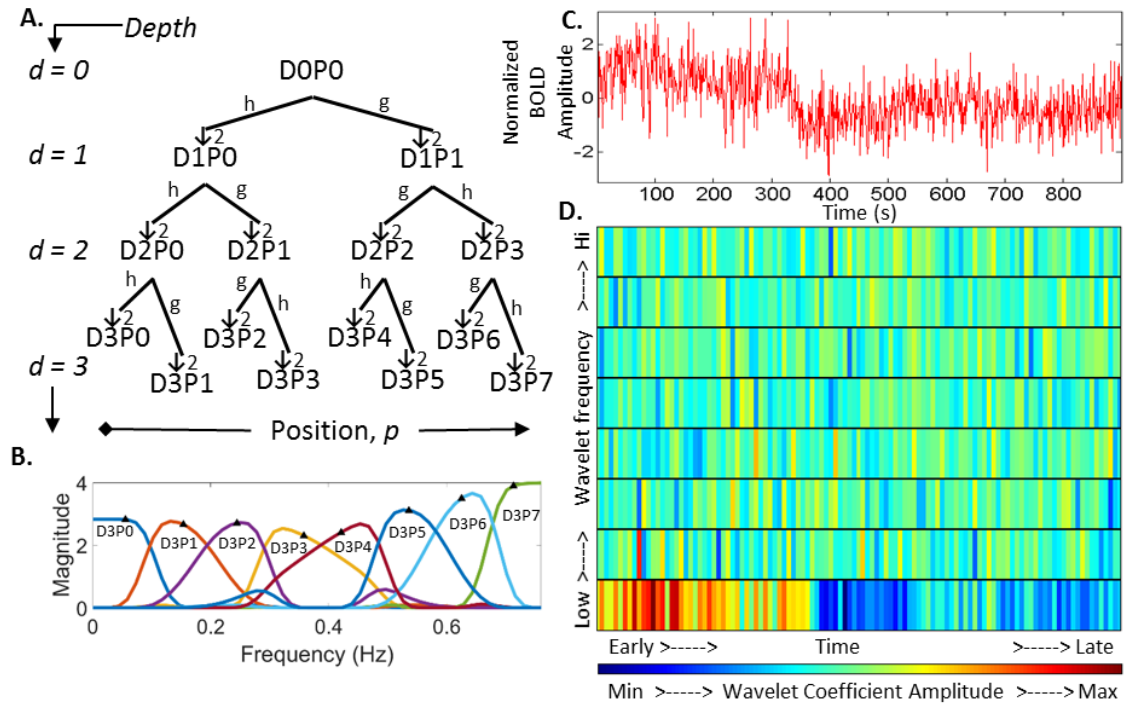


Figure 3.1: An outline of the methods employed in this study is shown in four parts. The dyadic construction of wavelet packet bases are shown in part A. Each row increments the application of pair of low pass ‘h’ and high pass ‘g’ filters. After each filtering step, the data are downsampled by 2,  $\downarrow 2$ . Rows are labeled by depth,  $d$ . Each row has  $2^d$  passbands, or positions,  $p$ . The effective  $d = 3$  wavelet packet filters for the Daubechies 7-tap wavelet are shown in part B. Part C provides an example BOLD signal, and part D plots the wavelet packet coefficients at positions 0-7 (counting upwards on the y-axis) for the  $d = 3$  wavelet packets. Note the larger magnitude fluctuations occurring at the lowest frequencies in the BOLD signal.

For this study, we chose Daubechies’ 7 tap wavelet (db7) for our WPT filters. At this dimensionality,  $\varphi$  and  $\psi$  define short duration filters with good separation between low and high frequencies. Each voxel signal was filtered to all positions of WPT depths 0 through 6, generating a total of 127 passbands. FC analysis was conducted for all voxels from each wavelet packet to produce a multispectral analysis of resting-state FC-fMRI networks.

### 3.1.5. Wavelet packet entropy

At each depth of filtration, the WPT schema acts to separate the total information in the signal between twice as many wavelet packets. The amount of information contained in each wavelet packet may be measured using one of several entropy criteria. For this manuscript, we chose to implement a variant of the well-known entropy metric, the Shannon

entropy, to measure the entropy of each wavelet packet. Because wavelet filters have roughly equal power over their respective ranges, they serve to normalize the relative entropy between wavelet packets. Thus, an appropriate measure for wavelet packet entropy is the non-normalized Shannon entropy:

$$H'(x) = - \sum_i x_i^2 \log(x_i^2), \quad (3.6)$$

with  $x_i$  being wavelet coefficient  $i$  of a particular wavelet packet  $x$  (Coifman and Wickerhauser 1992). Relatively lower entropies indicate that more of the signal's information is contained in the packet, while higher entropies indicate that the packet contains little of the original signal information. For signals such as the BOLD signal having a  $1/f$ -type distribution, the low frequency packets have the lowest entropies. And, at some high frequency position, the wavelet packet entropy is very high (greater than zero). Because fMRI data is expected to contain some amount of white noise (Greve, Brown et al. 2013), low magnitude wavelet packet data are expected to have a low signal to noise ratio.

### 3.1.6. *Multi-subject data*

Reorganization of individual datasets for multi-subject hierarchical clustering was performed by concatenating the coefficients of a single wavelet packet, voxel-by-voxel, from all brain voxels, and from all volunteers, into group level datasets. As described in section 3.1.6, HC metrics are calculated point by point across time, and, therefore, are not affected by the sharp discontinuities introduced upon concatenation. Voxels that did not contain signal for any single volunteer's dataset were removed from group-level analyses in order to circumvent issues with pairwise distance metrics. In addition to the largest dataset consisting of 112 individuals, individual datasets as well as multiple selections of groups of 5, and groups

of 30 individuals were taken from the *Rockland Sample* in order to judge the consistency of the study's results.

### 3.1.7. Hierarchical clustering (HC)

HC organizes a collection of data into distinctive groups via a rigidly structured approach. First, a distance metric,  $S1(i, j)$ , is calculated between all  $i$  and  $j$  indices of voxel signals. Voxels and/or clusters of voxels are then clustered together until only a single cluster exists. After each clustering step, an updated distance metric,  $S2(a, b)$ , is calculated between clusters  $a$  and  $b$  via any of several linkage metrics.

For any HC analysis, the internal consistency of the set of distance metric coefficients relative to linkage metric coefficients may be calculated via a Cophenetic correlation coefficient,

$$Coph = \frac{\sum_{i<j}(S1_{ij} - \overline{S1})(S2^*_{ij} - \overline{S2})}{\sqrt{\sum_{i<j}(S1_{ij} - \overline{S1})^2 \sum_{i<j}(S2^*_{ij} - \overline{S2})^2}}. \quad (3.7)$$

Variables,  $i$  and  $j$  are voxel indices,  $S1$  are a dataset's pairwise distances, and  $S2$  are the linkage distances. The overbar indicates the average, and the star beside  $S2$  indicates the first linkage distance at which voxels  $i$  and  $j$  are organized into the same cluster. Values of  $Coph$  close to 1 indicate consistent voxel-wise organization between distance method and linkage metric. Values approaching -1 indicate an inverted relationship, and values close to 0 indicate no relationship.

The decision for which pairwise distance-linkage combinations to use in this study was based upon the maximum  $Coph$  between multiple distance/linkage pairings (see supplemental table S1 for a complete list of distance/linkage  $Coph$  values). While the average  $Coph$  across pairings was 0.46 with a standard deviation equal to 0.13, the Euclidean-average pairing

exhibited the highest mean *Coph* at 0.77. The present study focuses exclusively on this pairing's results.

Table 3.1: *Cophenetic Coefficients from Multiple Hierarchical Clusterings of Filtered BOLD Data*

<b>Names</b>	<b>Mean</b>	<b>Std</b>	<b>Broadband</b>	<b>Min</b>	<b>Max</b>
Euclidean-Average	0.773	0.107	0.543	0.513	0.885
Euclidean-Centroid	0.763	0.132	0.349	0.349	0.880
Euclidean-Single	0.733	0.203	0.256	0.104	0.892
Euclidean-Weighted	0.647	0.153	0.327	0.296	0.832
Euclidean-Median	0.577	0.168	0.252	0.214	0.805
Correlation-Average	0.495	0.113	0.482	0.270	0.714
Euclidean-Complete	0.442	0.124	0.374	0.157	0.671
Correlation-Centroid	0.379	0.167	0.500	0.130	0.806
Correlation-Weighted	0.341	0.073	0.388	0.210	0.567
Correlation-Single	0.296	0.152	0.280	0.079	0.728
Correlation-Median	0.277	0.125	0.308	0.102	0.680
Correlation-Complete	0.275	0.112	0.339	0.100	0.630
Euclidean-Ward	0.254	0.111	0.352	0.013	0.503
Correlation-Ward	0.204	0.113	0.369	0.008	0.526
Overall Mean:	0.461	0.132	0.366	0.182	0.723
Overall Standard Dev:	0.203	0.033	0.089	0.139	0.133

The Euclidean distance metric is defined as:

$$S1(i, j) = \sqrt{(V_{i \neq j} - V_j)(V_{i \neq j} - V_j)^T}, \quad (3.8)$$

where  $V$  refers to the time series of a voxel  $i$  or  $j$ . The superscript  $T$  indicates the transpose operation. The 'average' linkage distance is defined as:

$$S2(a, b) = \frac{1}{(n_a n_b)} \sum_{i=1}^{n_a} \sum_{j=1}^{n_b} S1(i \in a, j \in b). \quad (3.9)$$

Variables  $n_a$  and  $n_b$  are the number of voxels contained within clusters  $a$  and  $b$ .

### 3.1.8. *FC networks constructed via dendrogram pruning*

An HC map's hierarchy may be visualized by plotting successive links as a dendrogram (see figure 3.2 and figure 3.5). For the dendrograms of the present study, voxels are ordered along the abscissa, and the linkage distance scales the ordinate axis. Horizontal lines are plotted between clusters joined at a given linkage distance. Vertical lines measure the linkage distance between successive clusters. Voxels are ordered along the abscissa in such a way as to minimize the length of each horizontal link. This arrangement results in the most related clusters being arranged adjacent to one another along the abscissa, i.e., the order of voxels along the abscissa is a linear projection of cluster relatedness. A pictorial description of this process may be found in figure 3.2.

FC maps are produced by pruning each HC map at one or several linkage points within the dendrogram. Pruning an HC map thus involves separating linked clusters at any of several points in the hierarchy. For this study, the choice of how to prune the HC map was informed by calculating the inconsistency of each link in the HC map. The inconsistency of a given link is an indication of the similarity of the elements connected below the link. The higher the value of this coefficient, the more dissimilar are the elements connected at that particular link relative to the elements connected beneath that link (Zahn 1971). For a given HC map, the  $k^{\text{th}}$  link's inconsistency is calculated as  $Y(k, 4) = (z(k) - Y(k, 1))/Y(k, 2)$ . Here,  $Y$  is an  $(m-1)$ -by-4 matrix whose first column,  $Y(k, 1)$ , is the mean of the linkage distances for the  $k^{\text{th}}$  link and the first  $G-1$  links beneath it. The quantity  $Y(k, 2)$  is the standard deviation of those linkage distances. The quantity  $z(k)$  is the linkage distance of the  $k^{\text{th}}$  link. Small values for the variable  $G$  bring the inconsistency algorithm to focus on locally inconsistent links in the HC map. Alternatively, larger values of  $G$  will search the area below each link to provide a more globally representative assessments of cluster inconsistency. Averaging effects quickly negate the

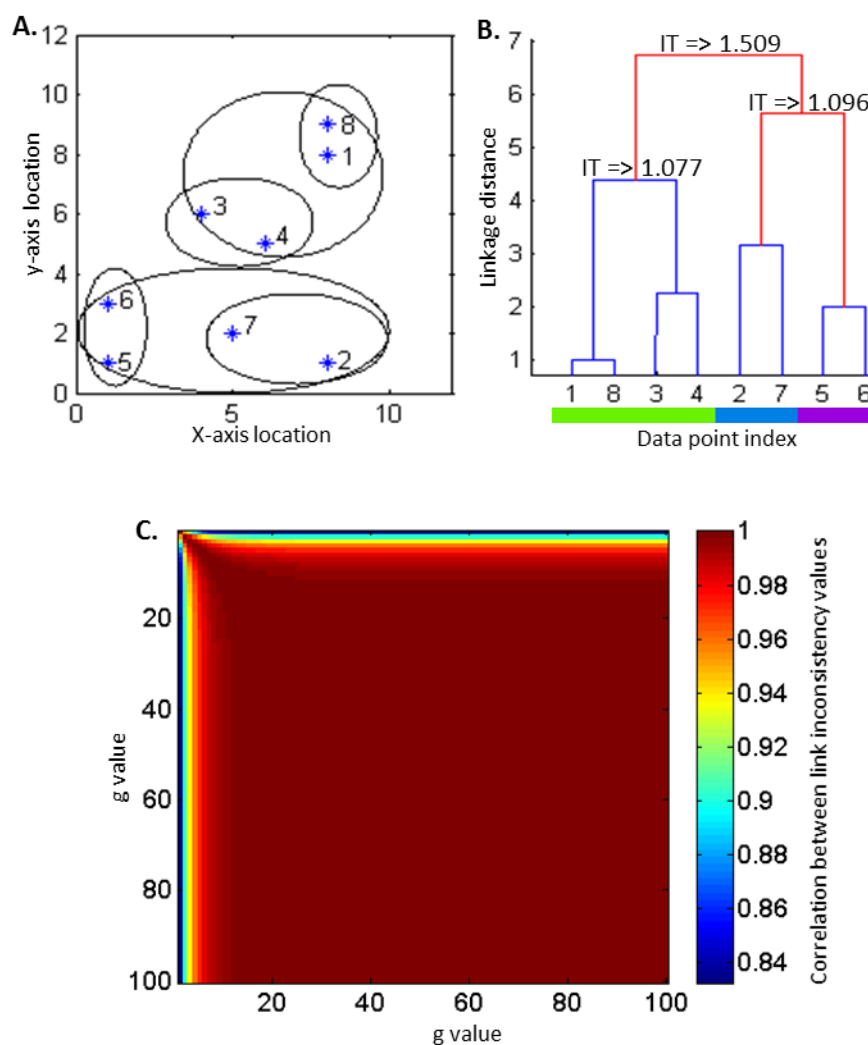


Figure 3.1: Here, we consider how a set of 8 points dispersed across two dimensions is arranged by hierarchical clustering. The pairwise distance here is the shortest line distance within the plain between each pair of points (part A). Points 1 and 8 are very close together. The linkage metric identified these points as having the shortest linkage distance ( $\sim 1$  unit), and clusters them together first. The average distance between each point in the new cluster and all other points is then calculated and the next lowest linkage distance is assessed. This process is iterated until the last two clusters are finally unified.

The hierarchy of clusters this process forms is conveniently displayed in its dendrogram (part B), where clusters are arranged along the abscissa with neighboring clusters joined together sooner than distant clusters. The ordinate contains linkage distances. Lines are drawn vertically from each cluster until they reach a linkage distance at which a cluster connects with a neighbor. A horizontal line then connects the two clusters. The process continues for increasing linkage distances until the final two clusters are linked.

To inform the choice of the clustering value  $G$  and the inconsistency threshold (IT), a plot of the correlation between the array of IT's for a range of  $G$ 's is provided in part C. As can be seen, differences among IT's quickly disappear at  $G > \sim 20$ .

impact of extremely large values of  $G$ . Part C of figure 3.2 provides a plot correlating the inconsistency values for  $G$  ranging from 2 to 101 from a prototypical HC map encountered in this study (specifically, the D5P1 HC map from a group of 5 volunteers). As can be seen,

large differences in the inconsistency values assigned to each link may be found in the lowest values for  $G$ . Changes in inconsistency values quickly even out such that around  $G = 20$ , few changes occur when increasing the sample size from which inconsistency values are derived.

Given a particular  $G$ , we select an inconsistency threshold ( $IT$ ) from which all links whose inconsistency lies above this threshold, and all clusters emerging from those identified links, are removed from the HC clustering tree. In this way, we can prune our HC tree so as to resolve internal features of the HC map's organization. If we choose the lowest value for  $G = 2$  and the largest  $IT$ , we resolve the data's organization to show an FC-fMRI network where the largest isolated jump in inter-cluster association, and all clusterings dependent on those associations, are removed. By removing the single most locally dissimilar link, this technique provides a reproducible technique for a coarse scale representation of some components of the whole FC-fMRI network. We can also observe the other extreme of cluster pruning, where a large  $G > 20$  and the lowest  $IT$  are chosen. This alternative provides a fine scale decimation of the FC-fMRI network that accounts for the global relationship between clusters. Following these contrasting approaches simultaneously allows us to detail complementary spatial scales of FC-fMRI network organization.

For any combination of the values  $G$  and  $IT$ , the dendrogram is pruned to a set of clusters,  $C$ . Because voxel order along the dendrogram's abscissa generally corresponds to voxel relatedness within the clustering hierarchy, the coloration of each element of  $C$  was pegged to cluster location on the dendrogram using a linear colormap spanning the range of the dendrogram's abscissa. The colormap is fixed to range across hues, red orange yellow green blue and violet, from left to right across the dendrogram. If the required number of hues exceeds 256 (a discrete limit in hue variation for many graphics processing systems), the saturation and color values (brightness) are varied to provide visual contrast between clusters.

### 3.1.9. Comparing WPT-HC networks

To compare the similarity between networks, we implement a mutual information-based criterion. Specifically, we use Marina Meila's normalization of inter-clustering mutual information called the *variation of information* (Meilă 2007):

$$\text{VarInf}(C, C') = [H(C) - I(C, C')] + [H(C') - I(C, C')] \quad (3.10)$$

Here,  $H$  is the entropy of each clustering,  $H(C) = -\sum_{i=1}^k P(i) \log_2 P(i)$ , with  $P(i)$  the probability,  $\frac{|C_i|}{n}$ , of choosing one of the voxels in the cluster  $C_i$  from all  $n$  voxels. The term  $I$  is the mutual information between clusterings,  $I(C', C'') = \sum_{i=1}^k \sum_{j=1}^l P(i, j) \log_2 \frac{P(i, j)}{P(i)P(j)}$ , where  $P(i, j) = \frac{|C'_i \cap C''_j|}{n}$ . The first term in equation (3.10) may be thought of as how much information is lost when going from FC network  $C'$  to  $C''$ . The second term is then how much information is left to be gained when going from  $C'$  to  $C''$  (Wagner and Wagner 2007). *VarInf* is an excellent choice for comparing whole-brain FC networks because it is a distance metric on multiple clusterings from the same dataset, a fact that enables several realizations of FC networks within the same individual or group-level brain to be compared.

## 3.2. Results

### 3.2.1. *Wavelet packet entropy*

If we look at the wavelet entropy of each packet signal, we can refine the search across spectra to only those packets characterized by low relative entropy, and hence, more signal. A plot of the non-normalized Shannon wavelet entropy from the group of 112 subjects' WPT filtered fMRI signals is provided in part A of figure 3.3. Two colorbars are used to better represent that entropies form two distinct zones: the negative entropy, powerful signal zone (cool colorbar), and the positive entropy, weak signal zone (hot colorbar). The designation of positive non-normalized Shannon entropies is important as it is an indication that the signal in these zones becomes very low in magnitude, fluctuating inside the range  $(-1, 1)$ . The distribution of positive entropy varies somewhat across data sets that include more or fewer volunteers, particularly for data sets including only one volunteer. The plot in part B of figure 3.3 shows, for each dot, wavelet packets, across all datasets, having positive entropy. Positive entropy, low signal magnitude packets are shifted to the right in the spectrum. Because fMRI data contains some white noise, high entropy wavelet packets have a low signal to noise ratio. The spread of positive entropy packets into lower frequencies increases among datasets having fewer individuals.

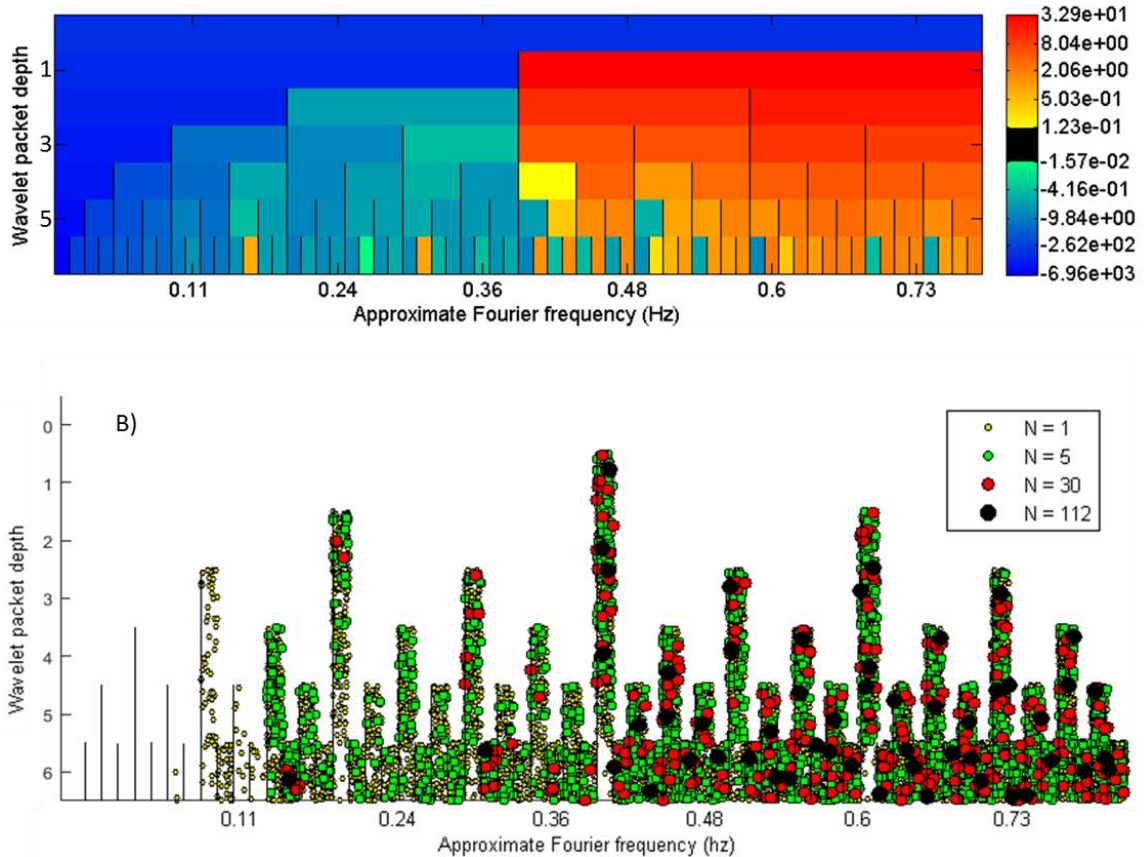


Figure 3.3: An assessment of the non-normalized Shannon wavelet entropy is given across all wavelet packets. Part A shows the non-normalized Shannon entropy of individual wavelet packets from the group dataset of 112 volunteers. Negative and positive entropy measures are visualized in hot and cool colors, respectively. Wavelet packet depths are arranged vertically, and positions horizontally. Each depth's wavelet packet positions spans a range of the horizontal axis proportional to that packet's spectral range. Part B identifies those wavelet packets having positive entropy across all datasets.

### 3.2.2. Variation in information ( $VarInf$ ) across spectra

The inter-spectral  $VarInf$  was calculated between WPT delimited FC networks having 2000 clusters ( $\pm 1\%$ ,  $G = 50$ ) from the group of 112 individuals. Inter-spectral  $VarInf$  values served as distance metrics for HC using the 'average' linkage metric, the best choice as determined by inter-spectral FC network HC map  $Coph = 0.810$ . The HC dendrogram is provided in part A of figure 3.4. Notice that the plot assembles wavelet packets into several groups having strong separation from one another. Efficient visualization of packet relatedness is provided by inconsistency-based network pruning. Part B visualizes wavelet packet groupings when the most locally inconsistent link is removed from the dataset. An oval

labeled ‘1’ is provided in part A showing where this link is located on the dendrogram. The link removes the association between the D3P1 packet and a frequency component internal to that packet—namely, the D5P4 packet spanning the approximate range [0.089 to 0.113 Hz]. When this link is pruned, we observe that the frequency domain of FC-fMRI networks separate very well into at least four systems: a system that includes a set of low frequency oscillations (LFOs) spanning  $\sim 0.01$  to 0.1 Hz, a ‘high’ frequency system above  $\sim 0.2$  Hz, a ‘transitional’ system lying between these two ranges, and a ‘DC’ frequency system that includes all packets having the lowest sampled frequencies (0.003 Hz). Because we are interested in the FC-fMRI network variations at finer spectral scales, we chose also to prune the dendrogram at the maximum  $IT$  for which a single packet in the LFO range (specifically, a single packet among the D6P1, D5P1, D4P1 packets and their finer scale subbands) appears in a different cluster from the others. For this, we used a global value of  $G = 50$ . This operation prunes the dendrogram in part C at the oval marked ‘2,’ separating the D5P1 and D6P1 packets (and their subdomains) from the D4P1 packet (and its subdomains). The  $IT$  at which separation occurs among LFOs is plotted across individual and group datasets in part D of the figure. The inset to the figure plots these same  $IT$ 's as a percentage between the maximum and minimum  $IT$  for each dataset. These results indicate that for group datasets, the  $IT$  at which the 0.01 to 0.1 Hz system breaks into smaller components falls at the 50% point of the dataset's  $IT$  range. That is, the increase in global internal dissimilarity (very high  $G$  value) linking the LFO packets into a single cluster is at about the median of all possible increases in global internal dissimilarity. The difference between networks in the LFO range is of ‘moderate’ strength.

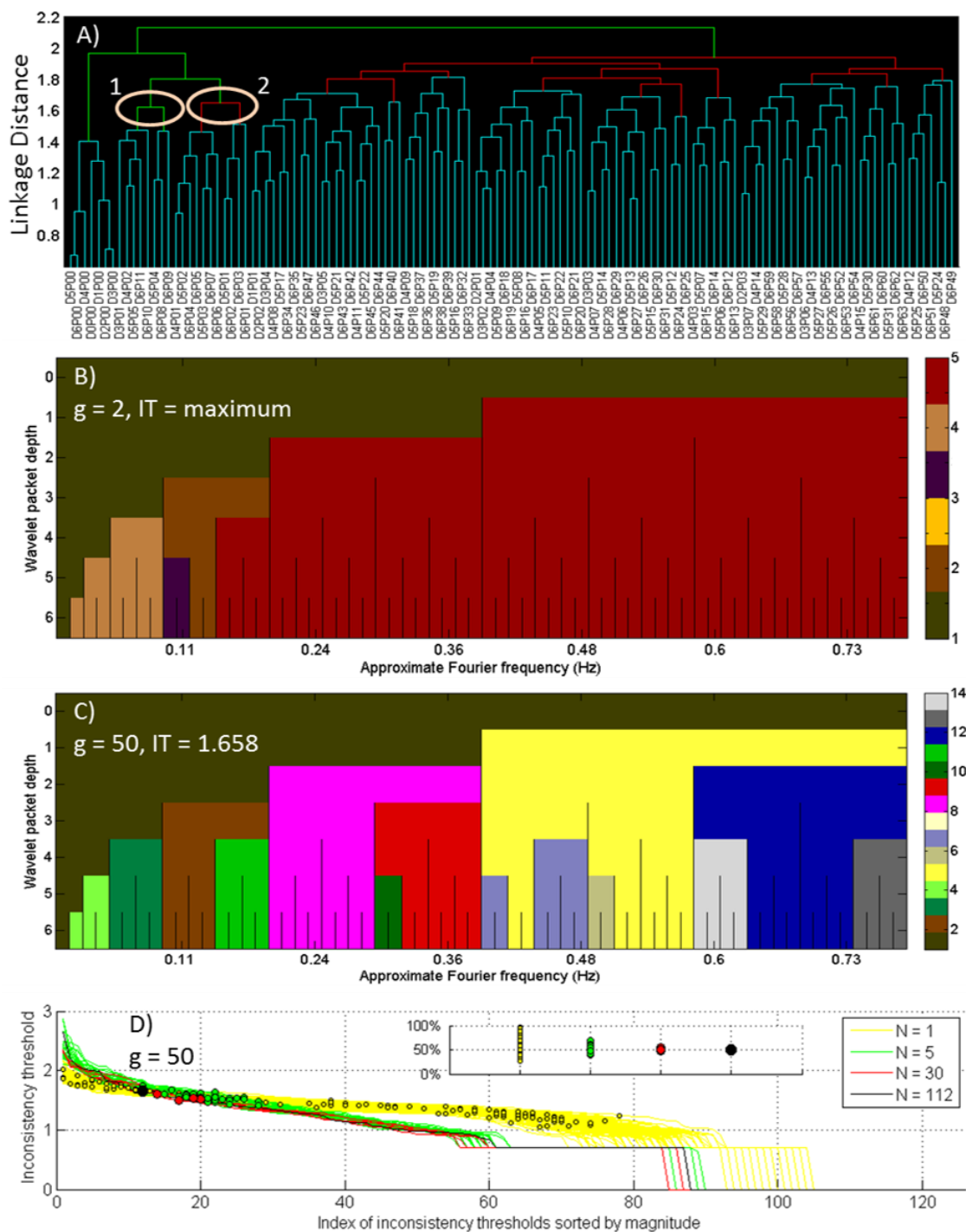


Figure 3.4: Variation in information (VarInf) groups similar functional connectivity (FC) networks across wavelet packets. The calculated VarInf is the distance metric in a hierarchical clustering (HC). Part A shows the dendrogram from HC. The dendrogram is pruned in two places: the most locally inconsistent link is removed (green links removed), and the top half of globally inconsistent links are removed (red links and dependent green links removed). Wavelet packet association maps are provided in parts B and C for the two levels of dendrogram pruning. Different colors represent the separation between packets. Part D plots the inconsistency thresholds (ITs) for each dataset for a  $G = 50$ . Filled circles indicate the IT at which a packet within the low frequency oscillation band ( $\sim 0.01$  to  $0.1$  Hz, specifically, the D6P1, D5P1, D4P1 packets and their subbands) is found in a different network. The inset shows, for each dataset, the percentage of ITs remaining after this link is removed.

### 3.2.3. Functional connectivity maps across spectra

To understand the overall variation of FC-fMRI networks across spectra, an example dendrogram from the D6P1 signal from the group of 112 volunteers is provided in figure 3.5. Figure 3.6 thru figure 3.8 then display cross-sectional views of FC-fMRI networks spanning the range of permissible wavelet packets. Datasets having differing numbers of volunteers were chosen to facilitate visual estimation of the network commonalities shared among groups and their variations. To inform network organization across spatial scales, contrasting and complimentary choices for the quantities  $G$  and  $IT$  are chosen.

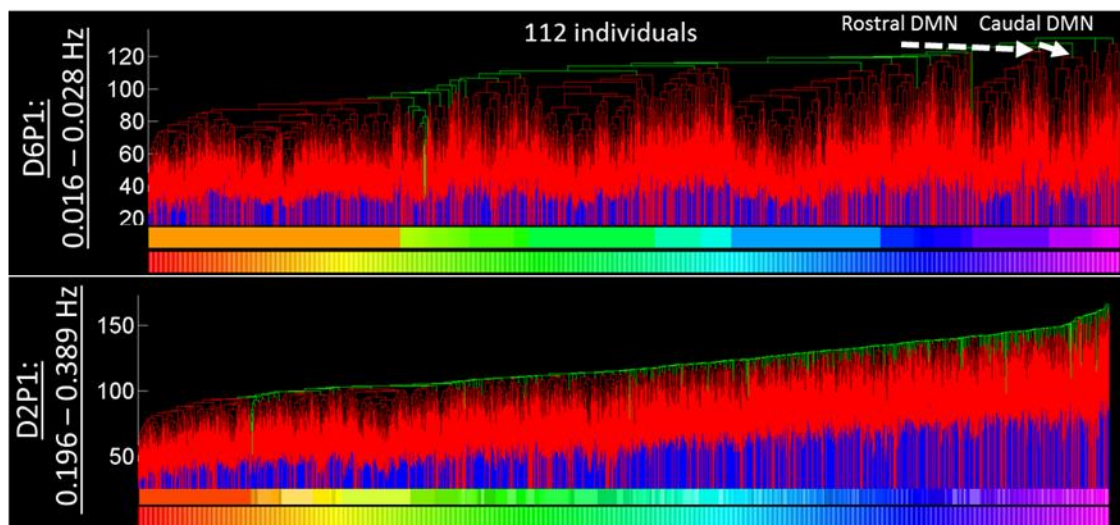
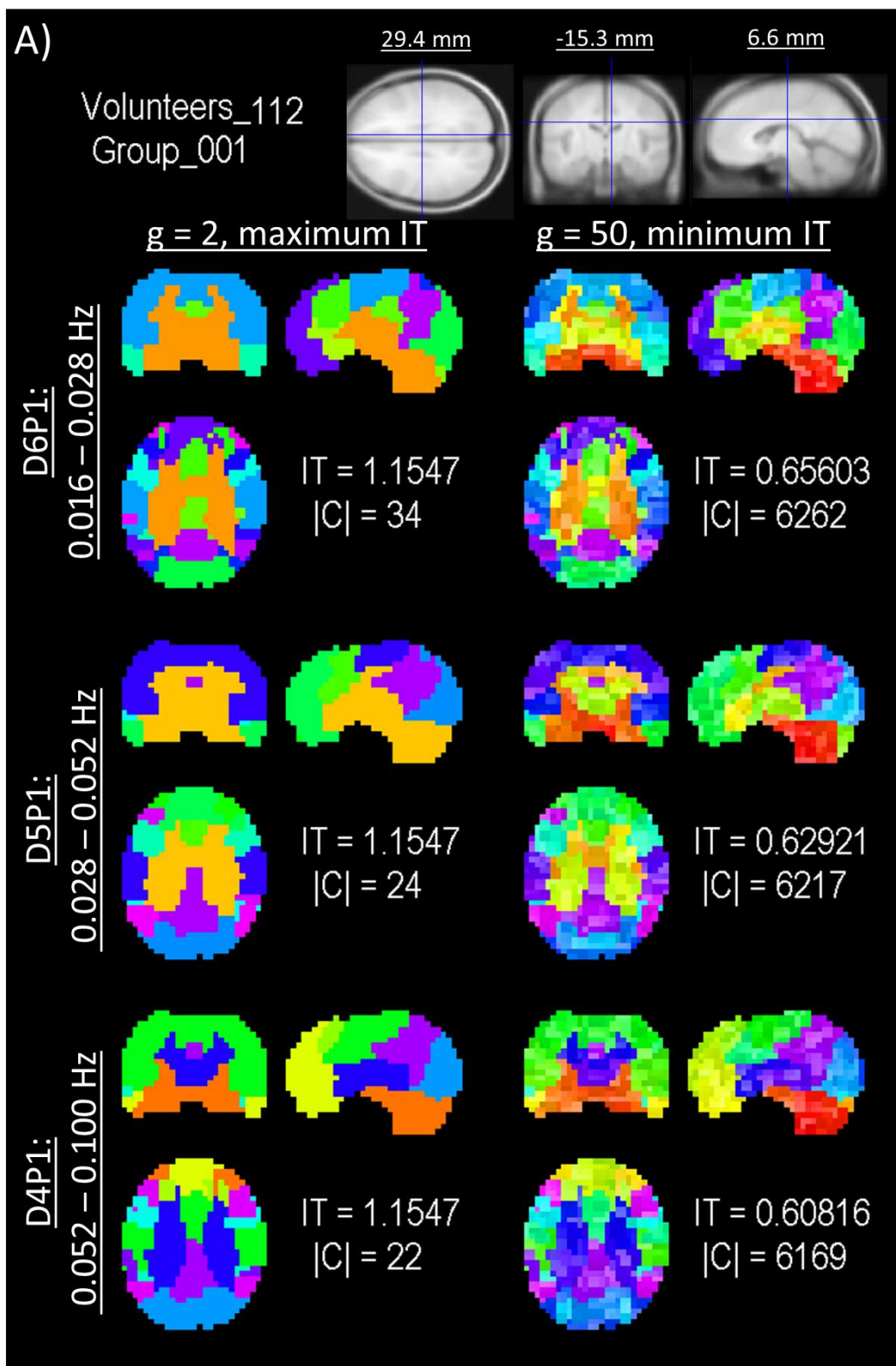


Figure 3.5: Dendrograms and colorbars for the whole-brain networks presented in figure 3.6 thru figure 3.11 are displayed. Green lines correspond to the coarse scale networks, while red lines correspond to the fine scale networks. Notice how the coarse scale network is formed by picking a single link and all dependent links to prune from the dendrogram, while the fine grained network make very many such removals of links set deep into the dendrogram. . Notice also the decrease in subnetwork grouping among high frequency dendrograms (like the D2P1 dendrogram). The loss of internal organization is prototypical of noisy datasets. The colorbars below (top – green/coarse, bottom – red/fine) each dendrogram map coloration between network clusters and dendrogram locations. Such correspondence is pointed out and labeled for rostral (dark purple) and caudal (purple) portions of the default mode network appearing in the D6P1 map from 112 volunteers (figure 3.6).



*\*Caption on next page*

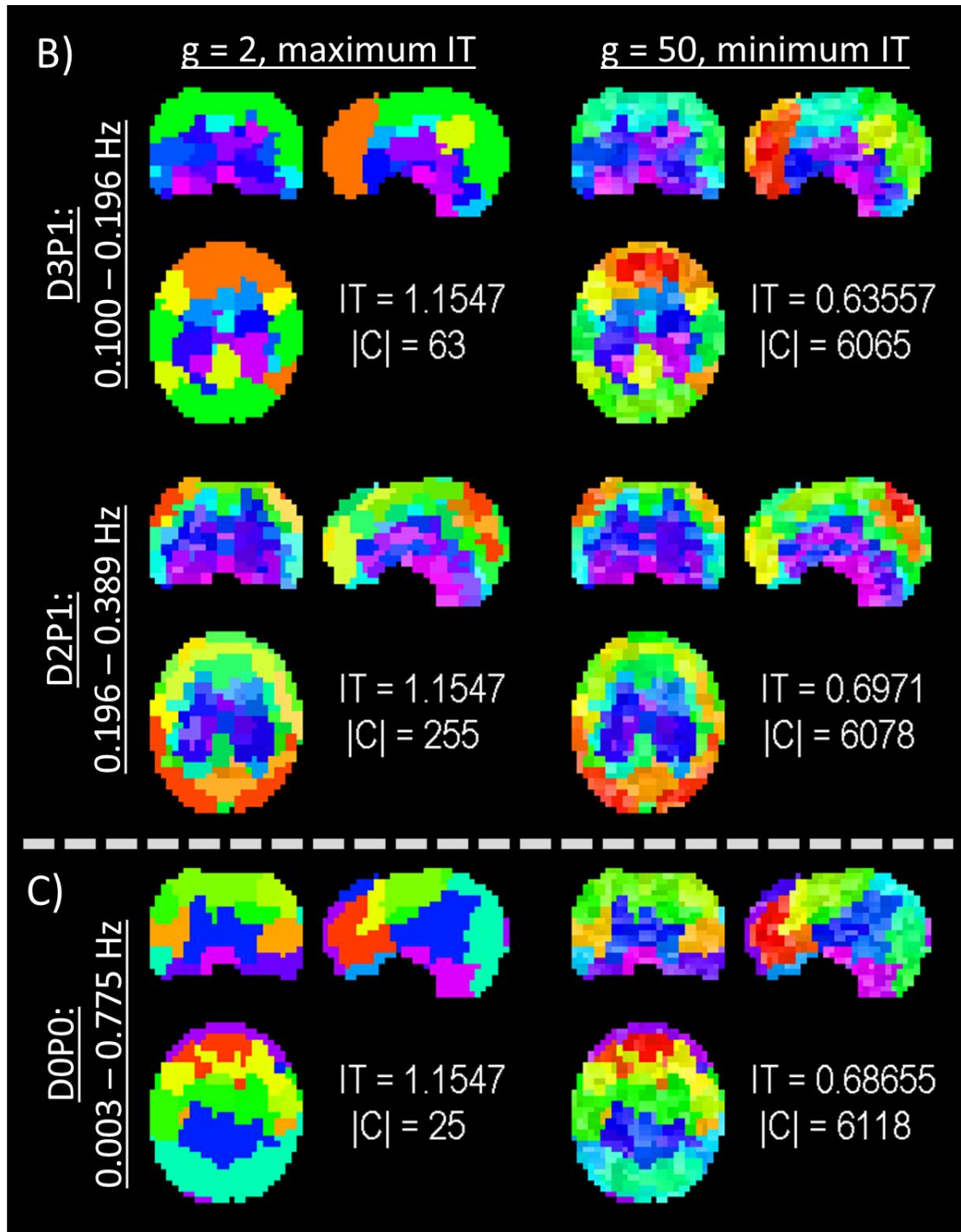
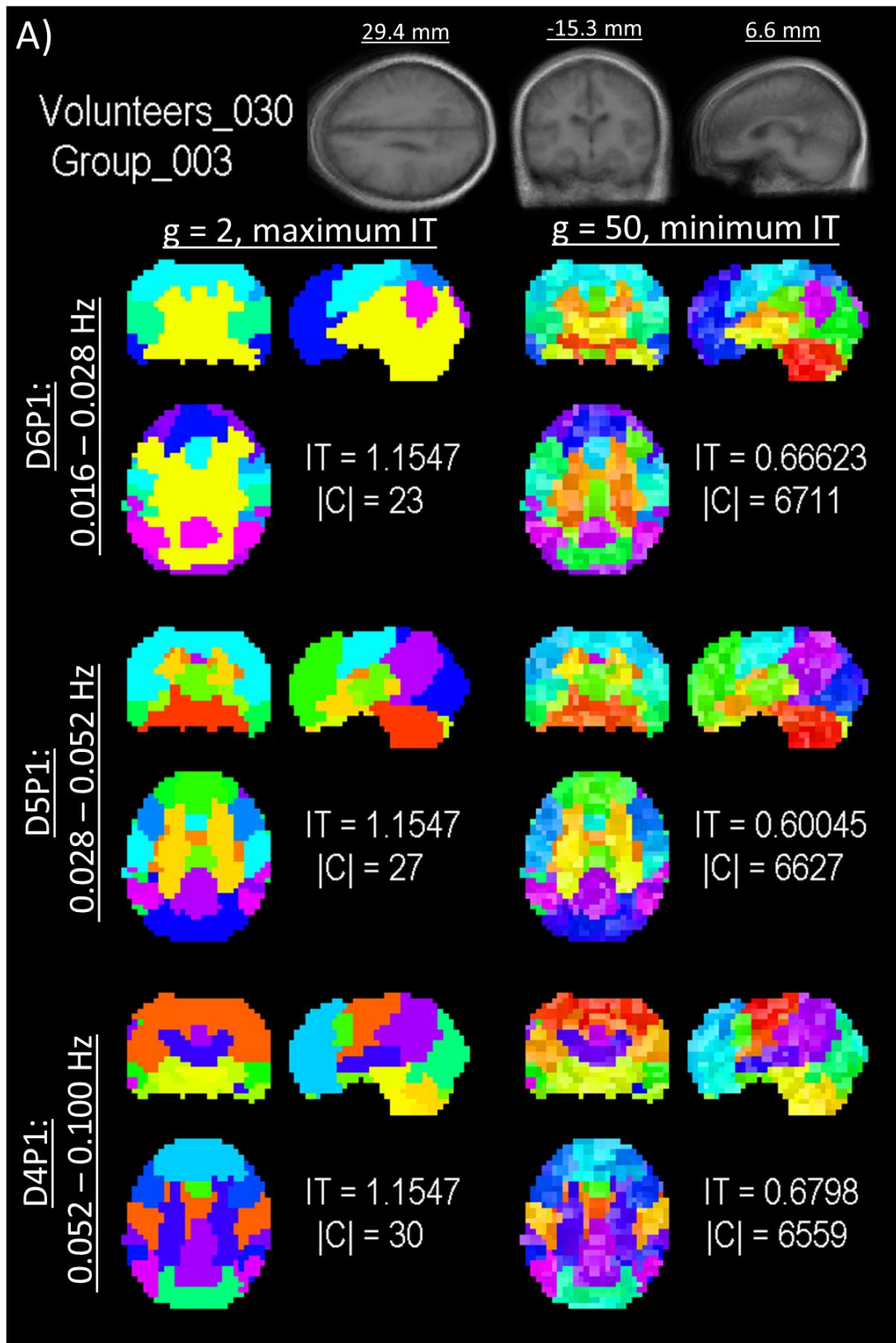


Figure 3.6: Similarities and differences between wavelet depth and position connectivity mappings from a group of 112 volunteers are illustrated. On each page whole-brain networks are arranged into columns and rows, with each row holding a different spectral range, and each column holding coarse (left) or a fine (right) spatial clustering. The anatomical image is the MNI average T1 brain from 305 volunteers. Coloration corresponds to the cluster each voxel is arranged into within the hierarchical clustering dendrogram. Part A is derived from the low frequency oscillation range, and shows the expected separation into functional networks including a somatomotor, frontal, visual, cerebellar, default mode network, etc. Part B is from the transitional and high frequency range, and shows varying degrees of corruption by high frequency noise, particularly in the brainstem. Part C is from the DC frequency range, particularly, the broadband network was chosen for display.



\*Caption on next page

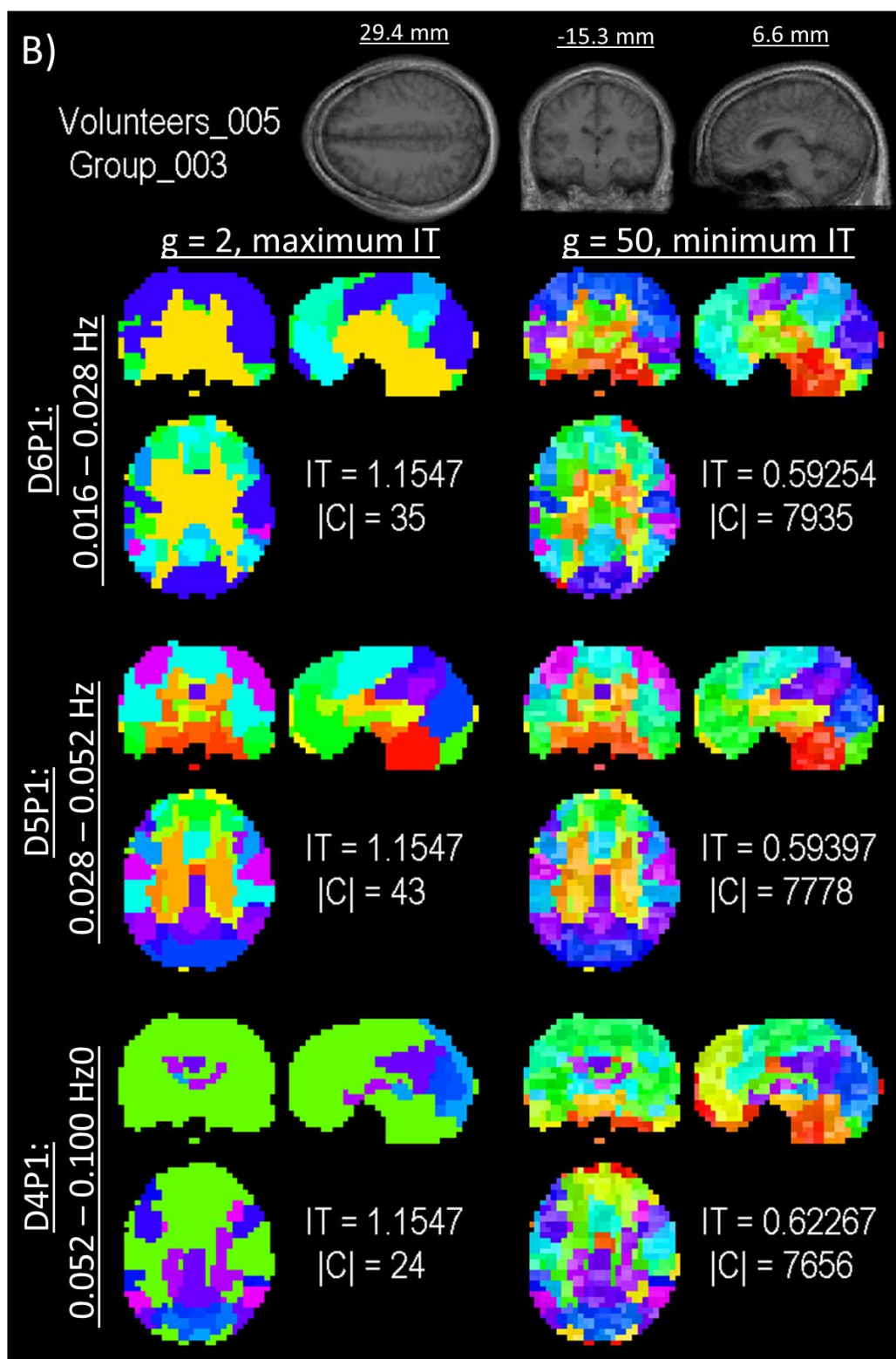
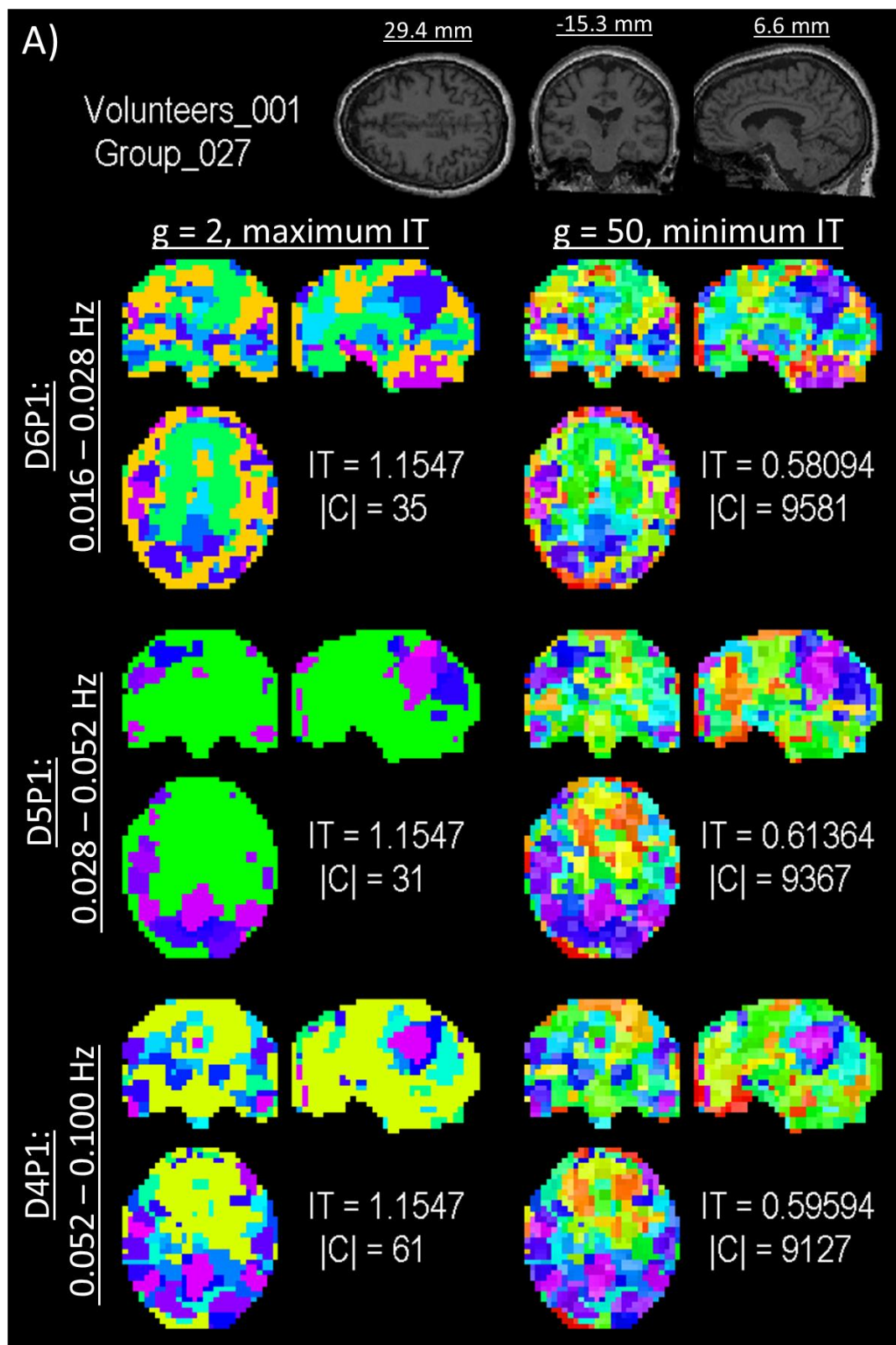


Figure 3.7: The same calculations as performed for figure 3.6 are applied here, albeit from a group dataset having 30 volunteers (part A), and from a group dataset having 5 volunteers (part B). Only packets from the low frequency oscillation range are displayed for each dataset. Each mapping produces the set of expected functional networks, somatomotor, default mode, etc. Inter-spectral network variability increases with decreasing numbers of volunteers.



\*Caption on next page

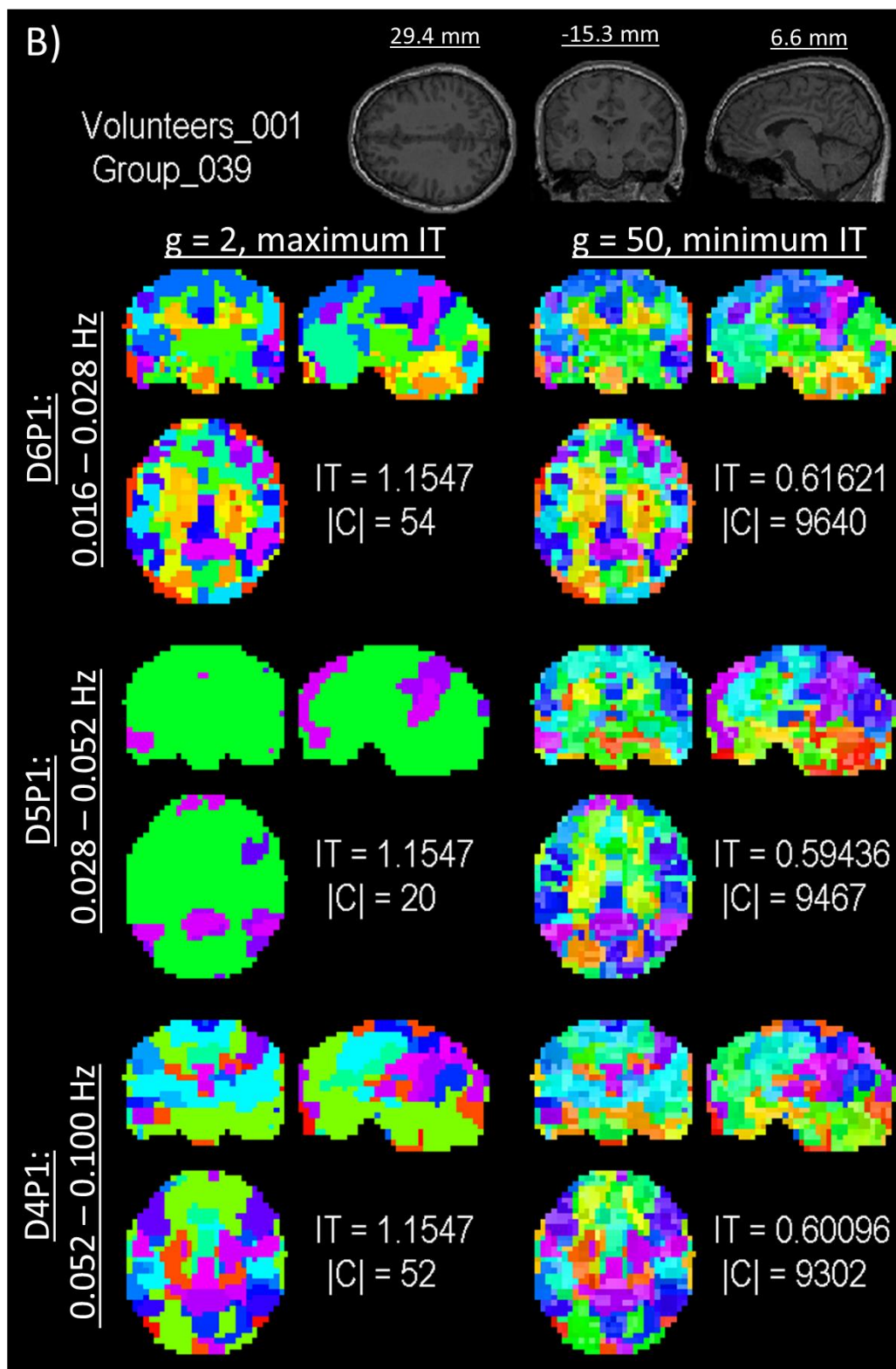


Figure 3.8: The same analysis as presented in figure 3.6 and figure 3.7 are conducted for individual 27 (part A) and individual 39 (part B). While many functional networks are difficult to fully discern, notice the prominence of the default mode network at both coarse and fine spatial scales, and its spectral variation.

### 3.2.4. *Functional connectivity maps across scan type*

Data from 32 volunteers were randomly selected for a second analysis conducted across variations in scan parameters. In addition to a data set with a TR = 0.645 s, data were acquired at TR = 1.400 s with 2 mm isotropic voxels (10 minutes), and at TR = 2.500 s with 3 mm isotropic voxels (5 minutes). To address the hypothesis that noise in either a global signal or from volunteer motion plays a role in FC network organization, movement information and the mean CSF/WM signal were regressed from these data. To better facilitate analysis via wavelet packets These data were resampled to a common frequency of 0.6 Hz. Spectral information outside the data's native range should be considered spurious. FC maps in three low-frequency fluctuation ranges are shown in figure 3.9 through figure 3.11.

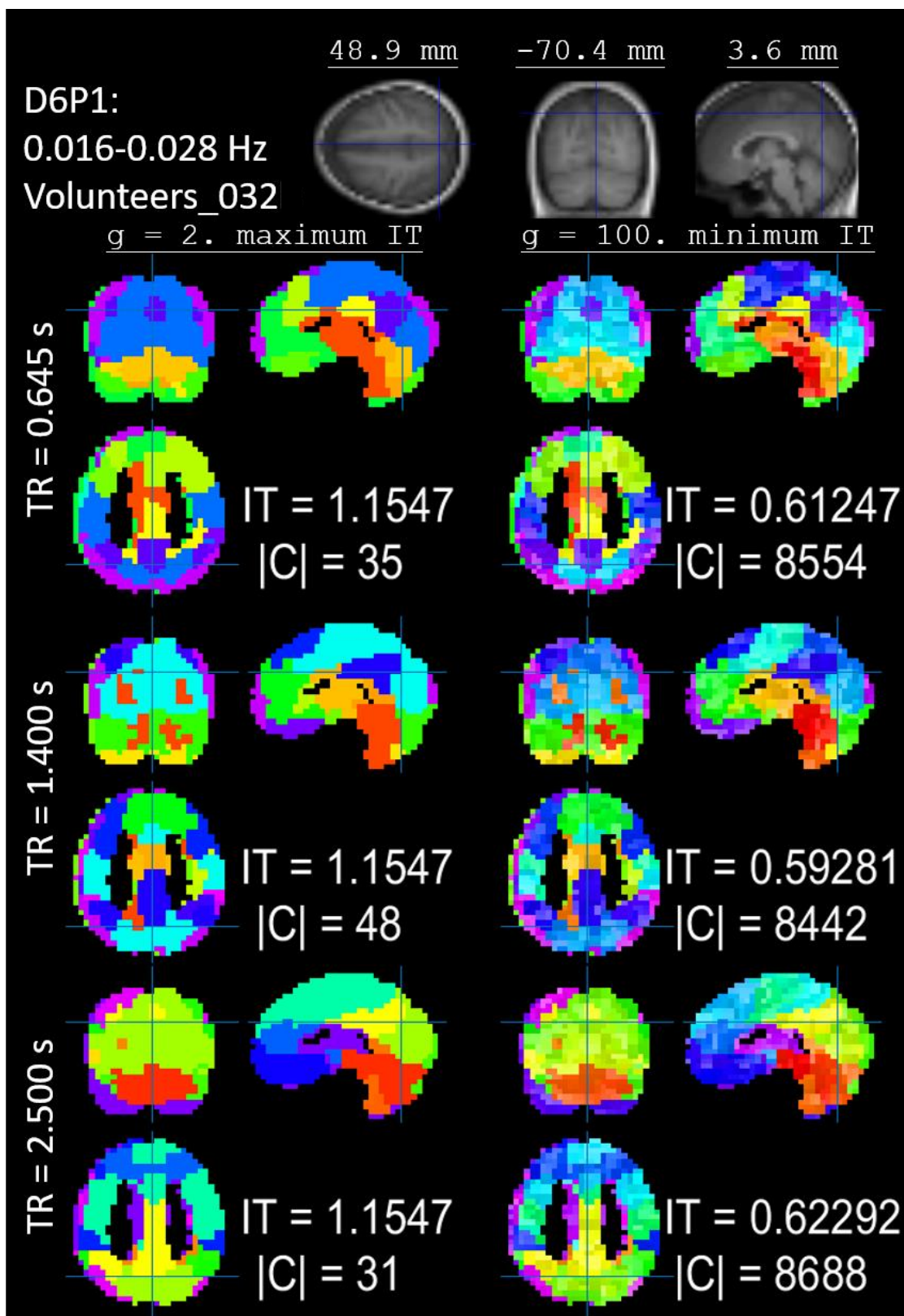


Figure 3.9: Functional connectivity networks from three qualities of scanning precision are displayed for the D6P1 packet.

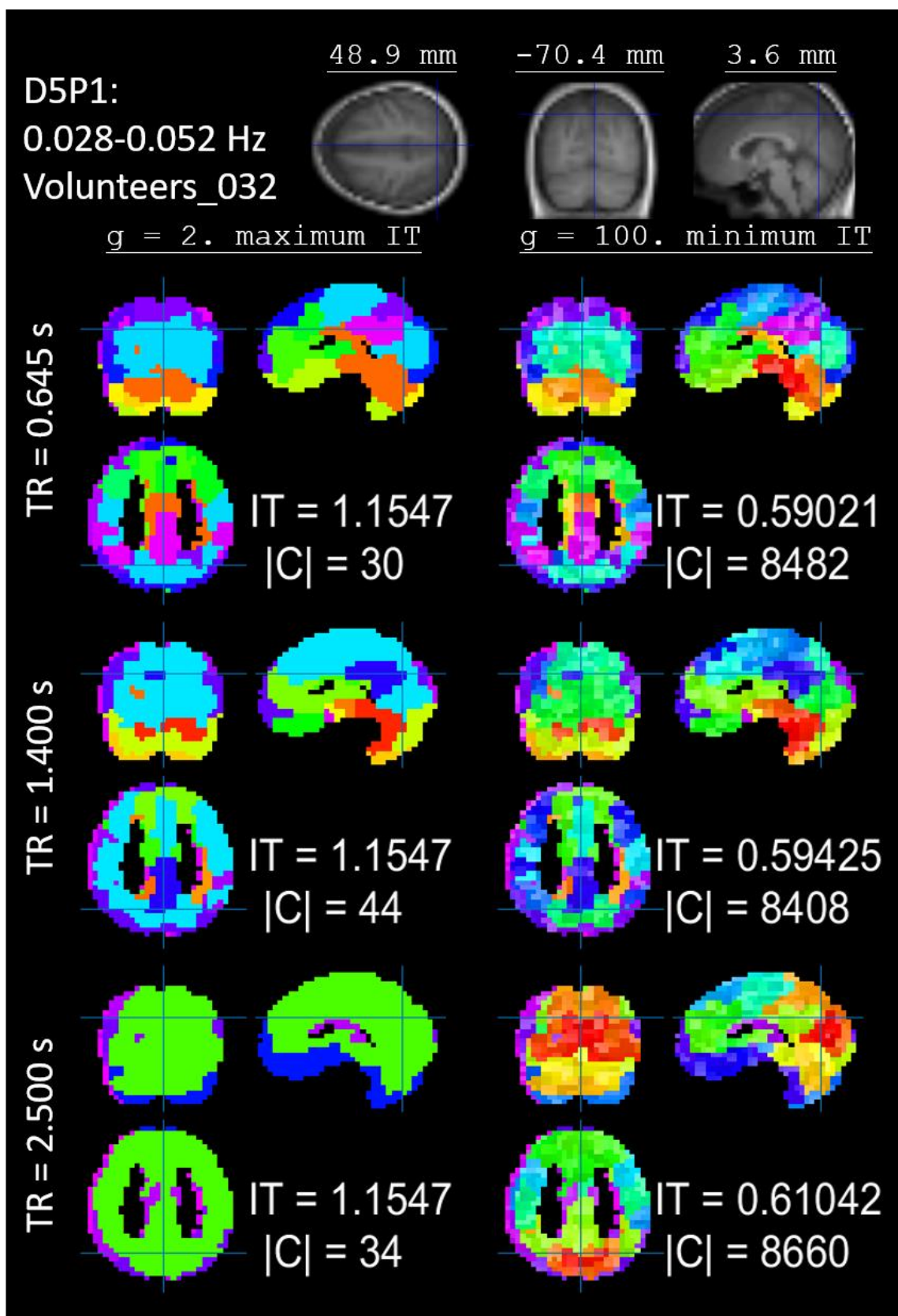


Figure 3.10: Functional connectivity networks from three qualities of scanning precision are displayed for the D5P1 packet.

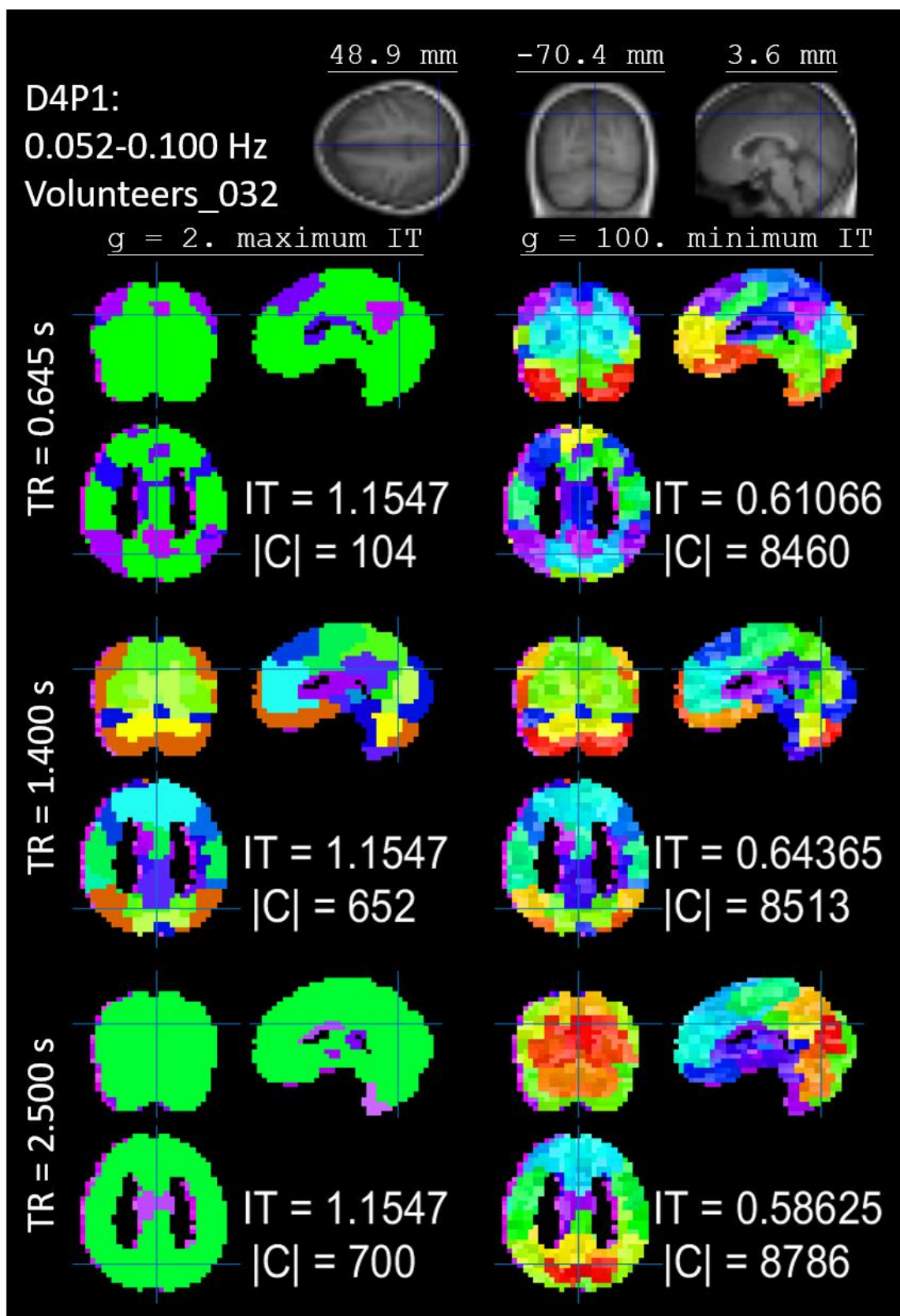


Figure 3.11: Functional connectivity networks from three qualities of scanning precision are displayed for the D4P1 packet.

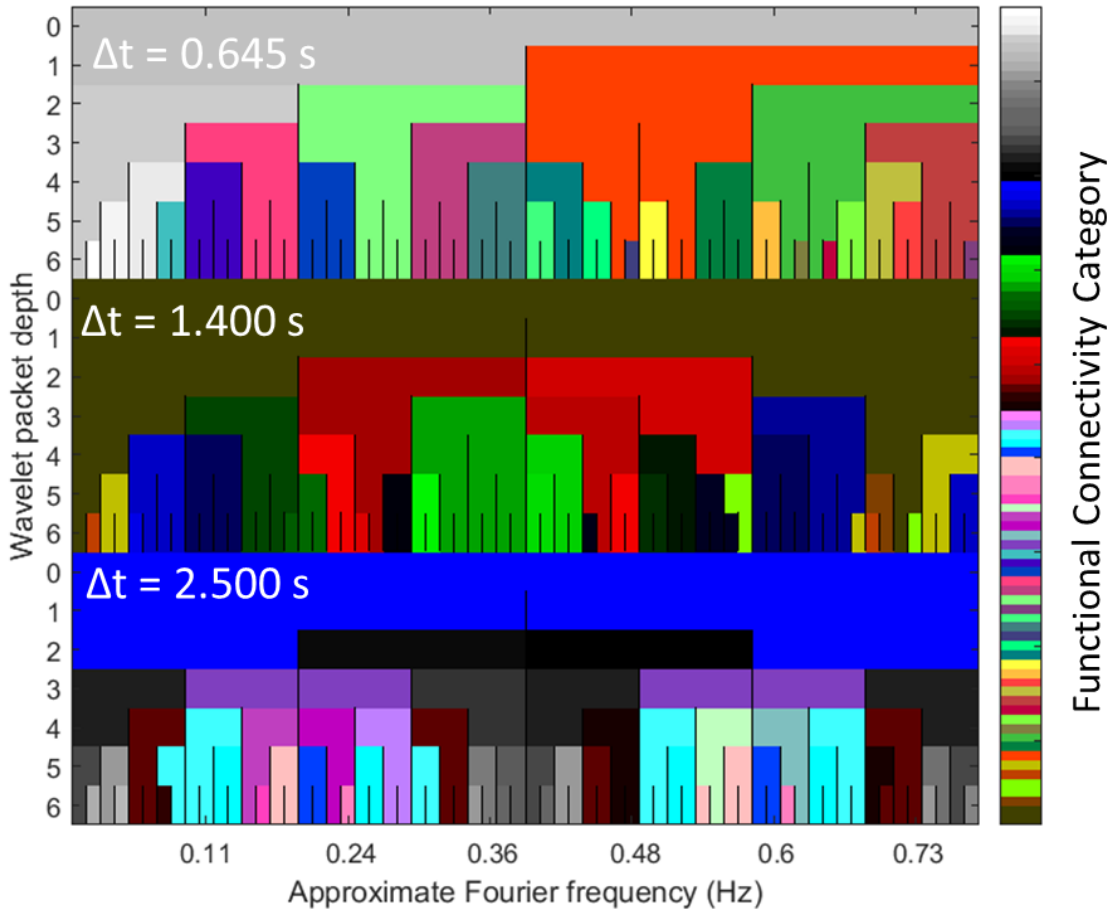


Figure 3.12: Spectrally delimited functional connectivity networks group according to pass-based range. The technique is identical to that from figure 3.4. Here, the analysis compares data at three different scan qualities. Coloration indicates group association. All data were upsampled to  $\Delta t = 0.600$  s. Note that, extrapolating high-frequency information from slowly sampled data causes the patterns of low frequency clustering to be reflected into higher frequency domains.

### 3.2.5. Packets in low frequency oscillation range

The entropy criterion confirms that FC-fMRI networks from packets at higher frequencies are more noise-ridden. The *VarInf* diagnostic indicates that packets in the LFO range tend to organize together at coarse scales (high *IT*), but may divide into individual components at finer scales (low *IT*). Part A of figure 3.6 presents the three uppermost depth packets lying in the LFO range —the D6P1 (0.016 – 0.028 Hz) D5P1 (0.028-0.052 Hz) and D4P1 (0.052 – 0.100) packets. Many commonalities are expected to appear across these networks. In all instances, the primary divisions observed in the coarsely-clustered data are

preserved during finer clustering, but additional gradations within the original coarse clusters appear. Both coarse and fine clusters are approximately bilaterally symmetric.

The somatomotor cortex (SMN) forms clear networks in the maps from all spectral and spatial scales. The network is efficiently visualized in each map's coronal slice. Amid fine scale maps, the SMN also subdivides into bilaterally symmetric subnetworks. The same holds for frontal, visual, and cerebellar cortices. Elements of the default mode network (DMN) appear in each of the LFO range packets, especially the precuneus and (bilateral) lateral parietal cortex. These two regions are functionally connected to one another in the very low frequency D6P1 map. Observing the location of this region on the dendrogram of figure 3.5, the caudal elements of the D6P1 network are directly connected to the rostral elements of the DMN in the medial frontal cortices.

Visual observation of the FC-fMRI networks produced by smaller groupings of 30 and 5 individuals produce similar results (figure 3.7) as in the larger group dataset. The SMN, visual, frontal, and cerebellar cortices, as well as the caudal DMN are apparent in each of the low frequency maps of each smaller group (see especially sagittal slices at fine scales). As with the larger group dataset of 112 individuals, there are variations in the boundaries of these brain networks across frequency bands. By visual observation, cross-spectral network variability increases with decreasing numbers of individuals. For instance, the DMN in the group of 112 individuals is always a piecewise construct, consisting of a posterior region and a medial frontal region. Conversely, whole DMN's are found in some of the wavelet packets among individuals, such as, the cyan region in the D6P1 packet from the five-volunteer group. Among individual network maps (figure 3.8), DMN connectivity is a particularly strong feature displayed across the selected slices. Large voxel-wise variations in the shape of this network

occur across sampled spectra. This is especially true of the medial caudal portion of the DMN that includes the precuneus.

### 3.2.6. *High frequency packets*

The entropy criteria predicts that FC-fMRI networks from high frequencies should contain a large amount of noise. High frequency information is present to varying degrees in the maps displayed in part B of figure 3.6. The D3P1 map spans the lower frequencies than the D2P1 map: 0.100 – 0.196 Hz, and 0.196-0.389 Hz respectively. While the D0P0 map spans the broadband spectra: 0.003 – 0.775 Hz. Noise appears in the D3P1 and D2P1 packets as a brainstem and other proximal regions that are grouped into a single mass (purple, blue). Domains in the distal occipital and parietal lobes exhibit less functional localization, probably due to noisy contributions (red). Whereas, functional domains are apparent in other regions of the lower frequency D3P1 packet, noise patterns extend into the higher frequency D2P1 map to preclude differentiation of other brain regions (green). The corruption in the D2P1 map is mirrored in the organization of its dendrogram (figure 3.5) in which single voxels of very small clusters are strung together, one-by-one, into a single cluster encompassing the whole brain. In all other maps having lower frequency components, subnetwork organization is a prominent feature of the dendrogram.

### 3.2.7. *The broadband network*

If an FC-fMRI network is built using broadband data (D0P0), the resulting network includes many of the features appearing in networks from the LFO spectra. This is especially true for the group having 112 volunteers (figure 3.6, part C). But, whereas in networks containing only low frequencies the precuneus is disconnected from deeper, non-neuronal regions—the lateral ventricles, and corpus callosum—the D0P0 map connects these regions.

This observation is most apparent when comparing the coarse FC-fMRI maps from the D4P1 and D0P0 packets (figure 3.6 parts A and C, sagittal as well as horizontal slices). The same blurring of regions including the precuneus is observed in datasets from smaller groups. Among individual maps, much of the coarse scale map is blurred into a single cluster. Conversely; individual fine scale broadband maps have amorphous and variegated network shapes. Frontal networks, none-the-less, form a distinct zone in the D0P0 maps from all datasets. Brainstem regions in D0P0 appear less pixilated than the same regions mapped with high-frequency data.

### 3.2.8. *Network stability after additional noise regression*

FC network independence between spectral passbands remained conserved after additional preprocessing procedures, as well as after perturbations to the data's acquisition parameters. Good definition in known functional networks is observed across all low-frequency fluctuation (passbands figure 3.9 thru figure 3.11). The highest frequency data (D4P1 packet, figure 3.11) lost definition in the brain stem at low frequencies. Despite attempts to place the spectral information from each scan in a common time-scale, spectral bands did not cluster together across different scan types. None-the-less, data from each scan type agglomerates into clusters based upon the input signal's spectral pass-band (see figure 3.12).

### 3.3. Discussion

Multiple avenues of inquiry converge to indicate that functional networks are best formed within a low frequency passband of the BOLD signal centered amid the decade 0.01 to 0.1 Hz. The entropy-based cost function indicates that high frequency data contain a large proportion of low amplitude fluctuations (figure 3.3). Hierarchically clustering the  $VarInf$  distance between multi-spectral FC networks again isolates the high frequency data from the low frequency data. At finer scales, this metric indicates that low frequency data are separable into at least three additional components: an LFO range (0.01 to 0.1 Hz), a transitional zone between the LFO and high-frequency ranges (0.1 to 0.2 Hz), as well as a range including all wavelet packets that include the data's DC frequency (0.003 Hz).

When visualizing these systems, the highest frequency networks do not appear to contain functional parcellation. Rather, the high frequency data segments the brain into ventral and posterior-dorsal regions. This segmentation may relate to differential fluctuations in the blood supply from the large arteries and veins that pool together at those locations. The cardiac and respiratory rhythms occur at relatively high frequencies of  $\sim 2$  Hz and  $\sim 0.2$  Hz, respectively. Recall that physiological noise artifacts were not regressed from the present dataset before analysis. FC-fMRI networks contain progressively clearer functional parcellation among packets containing information from the transitional band and from the LFO band. Because of the large structural differences between the high and low frequency networks, it is likely that there is not a true broadband network, but rather that networks built from broadband data mix signals that are many times functional data as well as correlated noise.

A common heuristic in fMRI studies is to filter signals to the LFO range before analysis (Biswal, Deyoe et al. 1996, Murphy, Birn et al. 2013). The present study confirms the

utility of this practice while providing insights into its limitations. Whereas the application of optical methods to measure blood and blood-oxygenation identify the LFO range as containing the maximum correlation between tissue oxygenation and calcium signals recorded from the same sites (Du, Volkow et al. 2014); and whereas electrochemical methods identify the LFO range as containing the maximum correlation when comparing blood oxygenation signals from grey matter sites in two different networks (Li, Bentley et al. 2015); the identification of correlation maxima within a frequency band is strong evidence for spectral variation, but it is weak evidence for the isolation of FC networks to only that frequency range. Indeed, many researchers offer accounts of the brain's activity as a concerted and coordinated signaling process carried out across multiple frequencies simultaneously (Berger 1929, Bullock 1948, Buzsáki and Draguhn 2004, Wu, Gu et al. 2008, Buzsaki 2009, Gu, Pasqualetti et al. 2015). The data driven spectral segmentation offered by the present study is a confirmation that differential FC networks develop within the LFO range. And whereas network structures lying above this range tend to appear less and less related to neuronal activity, the appearance of network structures in the DC frequency range indicates that some FC networks develop over longer time scales than measured during these scans (10 minutes) (Birn, Molloy et al. 2013).

The multi-spectral nature of brain signals in FC-fMRI was first motivated by similar findings in electroencephalographic measurements (Lu, Zuo et al. 2007, Mantini, Perrucci et al. 2007). Wu *et al.* (2008) found that the overall size of individual networks diminished as the analyzed pass-band shifted into higher frequencies (Wu, Gu et al. 2008). The study further noted that cortical networks were only present in lower frequencies (0.01-0.06 Hz), while limbic system networks were maintained over a broader frequency range (0.01-0.14 Hz). Zuo *et al.* (2010) found differential activation patterns manifested by slow-4 (0.027-0.073 Hz ~

D6P1) vs slow-5 (0.01-0.027 Hz  $\sim$  D5P1+D5P2) FC-fMRI activity (Zuo, Di Martino et al. 2010, Xue, Li et al. 2014). Like Wu *et al.* (2008) these authors also found an overall trend of weakened FC strength in the higher frequency, slow-4 spectrum. Likewise, in the present study, for packets that include higher frequency information, such as the broadband and D2P1 packets, the distinct organization of functionally relevant structures is obscured or lost.

Because wavelets are time-limited filters, the wavelet schema may be used as both a spectral and a temporal filter. Chang and Glover (2010) implemented wavelet coherence and sliding window analysis to demarcate times of frequency delimited network dynamics amid ROIs of the DMN (Cheng, Yan et al. 2013). The present work establishes preliminary results regarding the capacity to utilize data-driven, whole brain FC metrics alongside multi-spectral decomposition. Future studies aim to incorporate an enunciation of the present metrics to include whole-brain network variation over time.

Multispectral analyses supports the notion that the spectra of information included in FC analysis is a variable that mediates the architecture of FC within and across many brain regions (Buzsaki 2009). Because the capacity to detail this network architecture is directly related to the detail of the acquired data, the present study benefits from the availability of a large dataset containing highly temporally and spatially resolved BOLD scans. The present capacity to distinguish spectrally specific network architectures in multiple cortical regions may be the result of the use of fast multiband fMRI sequences (Xue, Li et al. 2014). The 300% increase in speed reduces aliasing of high frequency noise into lower frequencies, to improve the range of frequencies sampled. A similar benefit is theoretically gleaned from longer resting state scans.

In terms of spatial scaling of FC-fMRI networks, the present study presents two extremes of network organization, coarse and fine. The two scales depict similar overall

organization, with the fine scale map including added gradations that show degrees of similarity within the larger coarse clusters. For example, the robust segmentation of the SMN at the coarse scale informs the observation of bilaterally-symmetric SMN subnetworks. Such subnetworks may relate to internally distinctive processing systems. In the case of the SMN, these systems may correspond to the brain's somatotopic map of the body's sensory and motor units.

Studies using techniques such as ICA have evoked an ongoing debate as to how many components to divide brain networks into (Kiviniemi, Starck et al. 2009, Abou Elseoud, Littow et al. 2011). HC is well suited to multi-scale functional brain network analysis because it imposes an order to the relationship between brain signals. Previous studies implementing HC naturally lead up to this multi-scalar approach. Cordes (2002) reported that multi-spectral HC analysis presents bilaterally symmetric networks in the low frequency range (Cordes, Haughton et al. 2002). The study surveyed HC-based FC networks at one scale of  $IV$ , realizing 10 bilaterally symmetric clusters across four slices. A dendrogram sharpening method applied to the same dataset improved to make it possible to observe a representative portion of the DMN in the data (Stanberry, Nandy et al. 2003). Concomitant with recent advances in computing power, several studies have demonstrated that the networks produced by voxel-wise, whole-brain HC compared favorably with alternative measures of network organization (especially, independent component analysis) (Billings, Medda et al. 2013, Wang and Li 2013). In a similar study, visual methods for splitting the cluster tree enabled the 3D rendering of several large-scale networks including the SMN, frontal network, visual network, and others (Medda, Billings et al. 2014). The present study furthers these results to represent whole brain networks at multiple spatial scales. The use of contrasting and complimentary methods for

HC pruning provides a depiction of the brain as a gestalt of both local and large-scale networks.

### 3.4. Limitations and Future Directions

A primary limitation of this study is the difficulty of drawing systematic relationships or differences between networks based upon visual inspection. Because there is no gold standard for brain parcellation to which all parcellation methods can be compared—indeed, the search for such a standard is one of the goals of FC research (Rubinov and Bullmore 2013)—it may be worthwhile to refocus future analyses from the comparison of whole networks between groups to the direct comparison of the stability of subnetworks within and across groups. This variety of analysis is also fruitful for the analysis of time-varying connectivity which relies on the capacity to detect internal changes in network architecture over time (Keilholz, Magnuson et al. 2013).

A second limitation concerns the problems drawing robust conclusions after group level smoothing given individual anatomical and physiological variation. At the group level: some anatomical variations exist between individuals. These variations produce a number of spatial distortions between datasets. Normalization and realignment produce roughly similar, if slightly warped brain overlays between volunteers. And the hard cutoff of non-overlapping voxels biased networks to those central to deleted segments at the periphery. Even so, both cortical and sub-cortical functional networks are rendered. Future studies may implement additional strategies to improve parameter selection when registering parity between individuals as well as strategies for assessing individual variability. At the individual level: A large proportion of the network structure of individual datasets remains to be clearly interpreted. However, some regions, such as the DMN and SMN, are robustly identified at the individual level. Additional information about individual network architecture, for example, from diffusion tensor imaging structural data, might assist in applying some

constraints regarding possible inter regional communications, and thus enhance the interpretation of individual FC.

#### 4. Mammalian Brains: Comparative Functional Connectivity

Despite fMRI's wide spatial range and good spatial resolution, intrinsic limitations in fMRI minimize what FC-fMRI can detail about brain connectomics. These limitations include fMRI's low temporal resolution. Additionally, fMRI is an indirect measure of neuronal activity; measuring the positive/negative hemodynamic response to increased/decreased neuronal activity, respectively. While the evoked Blood Oxygen Level-Dependent (BOLD) response corresponds, most strongly, to neuronal activity in the Gamma band, the direct correspondence between spontaneous fMRI and spontaneous neuronal activity remains uncertain (Logothetis, Pauls et al. 2001, Logothetis 2008).

The BOLD response requires metabolic signals to be conveyed to the cardiovascular system. This transduction is believed to occur via multiple signaling molecules, utilizing both bulk diffusion and direct translocation via the glia. Predicting whether and how coordinated metabolic support corresponds to coordinated neuronal signaling benefits from direct measurements of neuronal activity. Previous studies have thus sought the use of rodent models (Pan, Thompson et al. 2013, Magnuson, Thompson et al. 2014). Simultaneous fMRI and LFP recordings in the rat identified strong correlation between the BOLD signal and LFP's in the somatomotor network (SMN) (Pan, Thompson et al. 2011). A follow-up study found bilateral SMN LFP sliding-window correlation to be strongly correlated with bilateral SMN BOLD sliding-window correlation. interhemispheric low frequency (0.01 to 0.1 Hz) BOLD and simultaneous LFP recording in the gamma (40-100 Hz), beta (14-40 Hz), and theta (4-8 Hz) frequencies. To discern the interaction between LFP and BOLD networks, the present study observed multi-scale network coordination among eight cortical sites from contiguous LFP and BOLD recordings in the rat. Because this gap in knowledge complicates the interpretation of BOLD-FC, knowing the neuronal origins of BOLD-FC confirms the theoretical utility of BOLD-FC to address the brain's neuronal communication.

FC-fMRI is used to identify the boundaries of familiar brain networks, like the somatomotor network (SMN), while identifying possible new ones, like the default mode network (DMN) (Raichle, MacLeod et al. 2001). The SMN serves to coordinate bodily sensation and motion through the primary and secondary somatic and motor cortices. The DMN is observed as a coordination among regions of the brain involved in self-relevant decision making (the medial prefrontal and posterior cingulate cortices), recollection (the hippocampus and lateral parietal cortex), and social awareness (auditory and temporal association cortices) (van Oort, van Cappellen van Walsum et al. 2014). It is habitually active when subjects are in a resting state, and remains connected, albeit in a reduced form, when mammals are under light sedation (Greicius, Kiviniemi et al. 2008, Upadhyay, Baker et al. 2011). The DMN becomes disconnected when subjects engage in an externally directed task. Short-term variations in DMN connectivity may indicate qualitatively different mentation (Keilholz, Magnuson et al. 2013). Alterations in DMN connectivity observed among psychopathological patients may serve as disease biomarkers (Whitfield-Gabrieli and Ford 2012). The presence of a DMN-like network among rodents means that we can test hypotheses about fundamental properties of neuro-vascular network coupling in rodent models (see figure 4.1) (Lu, Zou et al. 2012, Barks, Parr et al. 2013).

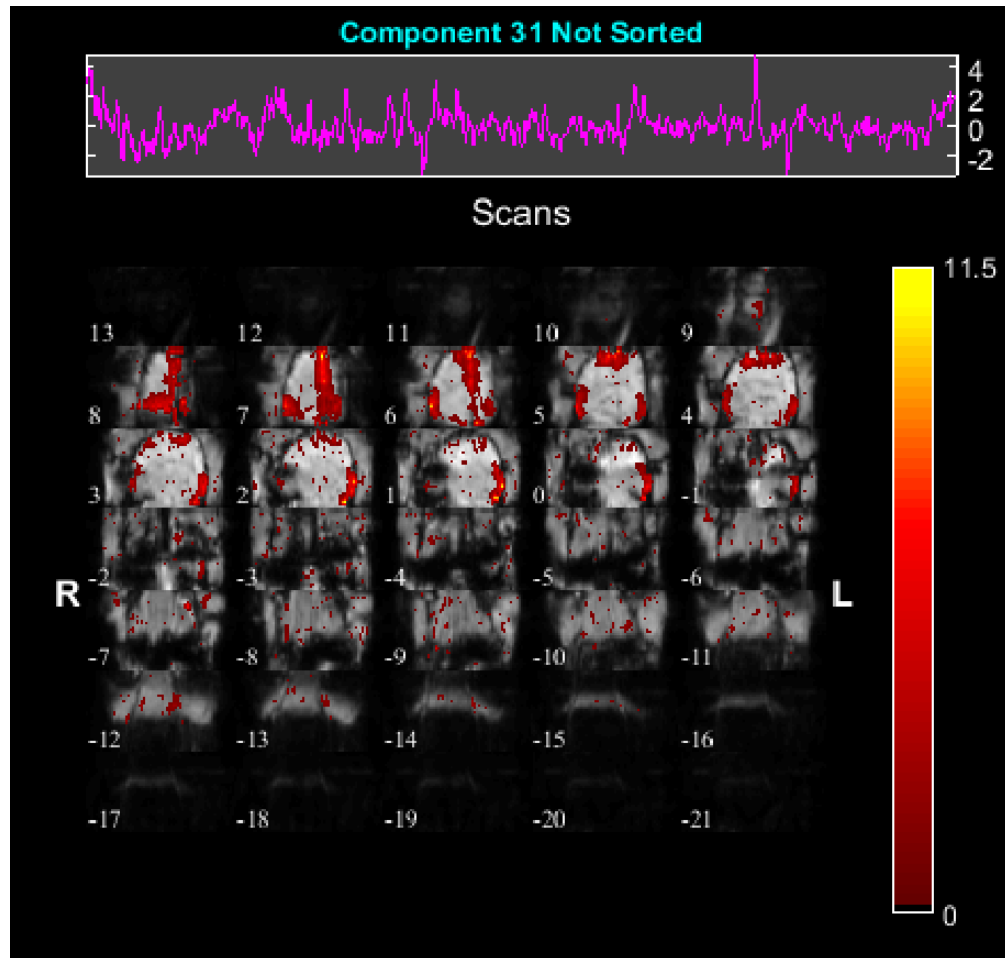


Figure 4.1: The rodent default mode network is revealed after an independent components analysis ( $N=4$ , 32 total components). Connected regions include the rodent hippocampus, cingulate cortex, and orbitofrontal cortex.

#### 4.1. Evolutionary Foundations of Comparative Neuroscience

Human beings are not the only encephalized organism. Indeed, the human nervous system required at least 3.5 Gya to be built from the first monocellular life. Throughout this time, a multitude of lifeforms developed from shared genetic instructions. Modern brains began as a diffuse neural nets communicating sensation and motor commands within cnidaria, a radially symmetric, jellyfish-like eumetazoa who formed before the Cambrian period 540 Mya (Garcia-Fernandez 2005). Evolved activation of conserved homeobox genes (HOX) guided the patterning of neurons into an anterior-posterior arrangement among bilateria (Wada, Saiga et al. 1998, Butler 2000). Bilatera nervous systems take many forms including the derivation of a dorsal nerve cord and strengthening notochord among chordates. The Cambrian itself saw the emergence of the first craniates whose dorsal nerve cord segments into forebrain, midbrain, hindbrain, and spinal cord and became encased in a hardened skull (Pani, Mullarkey et al. 2012). Cladistic analysis demonstrates that the craniate forebrain segments into telencephalon and diencephalon, which further segments into functionally specific regions such as an olfactory bulb, hippocampus, striatum, thalamus, hypothalamus, and other conserved regions (Wicht and Northcutt 1992). Amniotes, who adapted to terrestrial life approximately 312 Mya conserve this general body plan (Benton and Donoghue 2007).

Further encephalization took divergent trajectories among aves, and mammals. This is especially evident in the dorsal telencephalon where, approximately 150 Mya, mammals developed a six-layered neocortex and aves developed a nucleated neocortex (Jarvis, Gunturkun et al. 2005, Nomura, Gotoh et al. 2013). The mammalian neocortex always contains at least the following sensory and motor modules: primary and secondary visual, auditory, and somatosensory cortices (SII is sometimes replaced with a parietal ventral area), as well as a rostral deep field and a primary motor cortex. Euarchontoglires, the clad of

mammals including primates, rodents, tree shrews, and hares, diverged just after the Cretaceous-Paleogene extinction event 65 Mya (O'Leary, Bloch et al. 2013). These and future divergences are associated with the alteration in dedicated brain modules that conduct multisensory integration, and that manipulate differentiated somatic adaptations (e.g. whisking among rats, manual dexterity among humans, etc.) (Krubitzer 1995). The conserved organization of the mammalian brain allows researchers to effectively utilize rodent models in comparative neuroscientific studies.

## 4.2. Methods

Any measured brain signal is the product of many underlying processes. For instance: A single timepoint of a single LFP measurement is a parallel sum of all charge carriers. Each charge's contributions to the LFP measurement is weighted according to the product of distance from the electrodes and the tissue's impedance (Einevoll, Kayser et al. 2013). These potentials change with time as populations of neurons convey different bits of information. The amount of information shared between brain regions is reflected in their temporal correlations (Deco, Jirsa et al. 2011). Correlations between brain sites are also a function of the rate, or frequency, at which that information is shared. For example, it is thought that spectrally-dependent correlation between brain regions allows low-frequency signaling from one region to modulate high-frequency signaling from another brain region by locking each region's membrane potentials to the phasic variations of the low frequency fluctuation (Buzsáki, Anastassiou et al. 2012, Lisman and Jensen 2013, Thompson GJ 2014). Thus, a thorough examination of brain function should take into account elements of time, space, and spectra.

### 4.2.1. *Animal selection*

The study's invasive nature makes an animal model the only moderately ethical option. Rodents were selected because their extensive use in fundamental and pre-clinical science facilitates the direct application of this study's findings to the plethora of existing models. A rat's relatively large size among rodents makes the rat model better suited for fMRI. Sprague-Dawley rats are bred to tolerate being handled during research used in this experiment (Johnson 2012). Data are examined from 8 adult male rats.

#### 4.2.2. MRI acquisition

MRI images were acquired to identify the rat's FC networks. To do so, animals are first anesthetized with isoflurane (ISO). Anatomical data from each rat is acquired using a FLASH sequence (TR 70 ms; TE 4 ms; resolution 200  $\mu\text{m}$  isotropic). Because of the close relationship between DMN connectivity and animal wakefulness, it is necessary to bring the animal to a near waking state, rather than an anesthetized state, before it is possible to view the DMN in a functional brain scan (Upadhyay, Baker et al. 2011). To accomplish this, a solidifying fluid is used to temporarily ensure that the animal's head always finds the same resting orientation, even if periods of wakefulness at low anesthetic levels bring the animal to move. Whole brain functional images were then acquired (GE-EPI; 64 x 64 matrix, 3.5 cm FOV; 20, 1 mm slices; TR 1000 ms; TE 14.3 ms; 1000 images). Cardiac and pulmonary rhythms were continuously monitored during the scans to ensure physiological stability and for use in later noise regressions. An example, preprocessed, GE-EPI image is shown in figure 4.2.

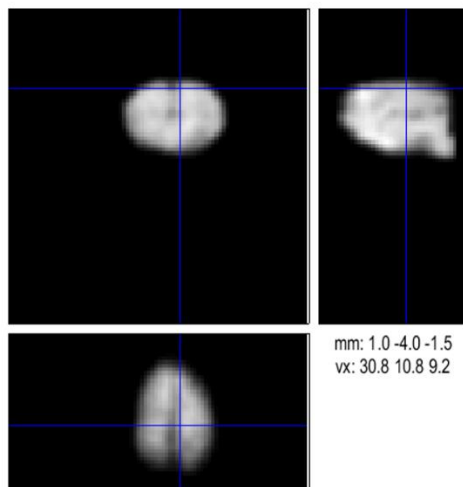


Figure 4.2: An example gradient-echo echo-planar image is shown after preprocessing.

#### 4.2.3. *Regions of Interest*

Six primary nodes of the DMN were chosen for network analysis. These include bilateral orbitofrontal cortex (OFC; from Bregma,  $\pm 0.5$  mm LR, 4 mm RC, -4 mm DV), bilateral retrosplenial cortex (RS;  $\pm 0.5$ , -5, -1.5), and bilateral hippocampus (HF;  $\pm 4.5$ , -5, -3). Sites were selected to represent distinct functional nodes of the DMN (Schwarz, Gass et al. 2013). An additional pair of electrodes were positioned in the somatomotor cortex (SMN;  $\pm 3$ , -2, -1).

#### 4.2.4. *LFP Acquisition*

The contribution that infra-slow LFP signals make to FC-fMRI networks was assessed by acquiring LFP data from Ag/AgCl electrodes in pulled glass pipets. LFP data was amplified to 1000x via a 10x headstage and 100x DC rated amplifier (*A-M Systems*). A common reference electrode was placed in the exposed subcutaneous tissue. Measurement of the LFP activity from each source proceeded for twenty minutes at 1000 Hz. An example LFP dataset is shown in figure 4.3. Because animals and their implanted electrodes remain in a stereotaxic apparatus during LFP recording, any movement would be catastrophic. Thus, rather than using additional restraints for recordings during light sedation, animals were given the sedative dexmedetomidine (DEX).

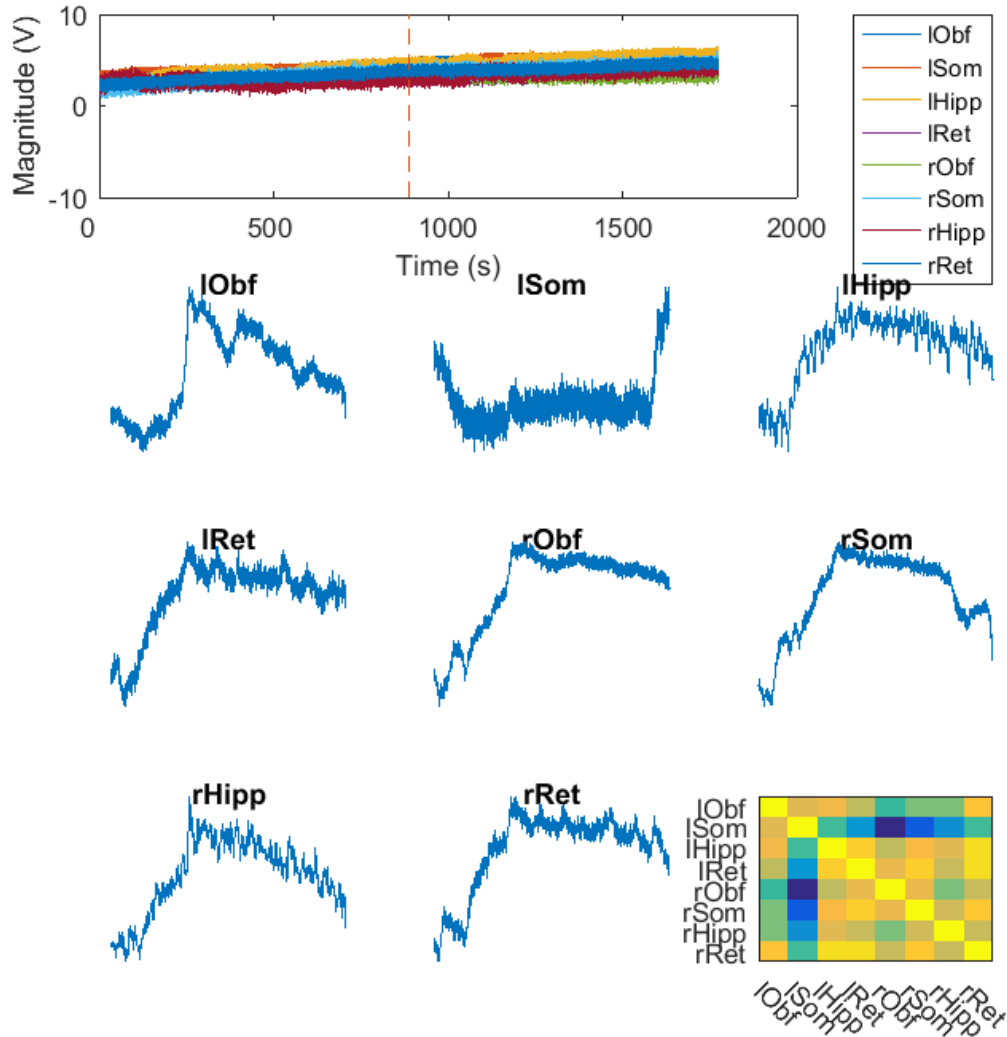


Figure 4.3: Examples of the local field potential signals (LFP) are shown after preprocessing. Inset data span 5 seconds. The lower left plot depicts correlation values between broadband LFP traces.

#### 4.2.5. Data Analysis

BOLD fMRI data were preprocessed via slice-time correction, movement correction, and physiological noise regression. They are spatially smoothed to 1 mm isotropic voxels. Locations corresponding to the LFP recording sites were visually identified in an aligned anatomical scan. An average from each site was taken for further analysis. LFP preprocessing involved visually identifying and removing sharp discontinuities from DC offset corrections made during data acquisition.

To compare FC networks between modalities, signals were decomposed by continuous wavelet filter banks. Wavelet-based frequency decomposition offers the advantage over traditional Fourier-based filtration methods in that wavelets are better suited for describing non-stationary signals like fMRI and LFP (Daubechies 1988). Spectrally delimited signals from each modality were concatenated across time and compared, pairwise, between each site, using the correlation distance. Figure 4.4 displays the spectrally delimited correlation between sites modal sites. Each spectrally delimited vector of distance metrics was compared, for each spectral band, between modalities, using the correlation distance.

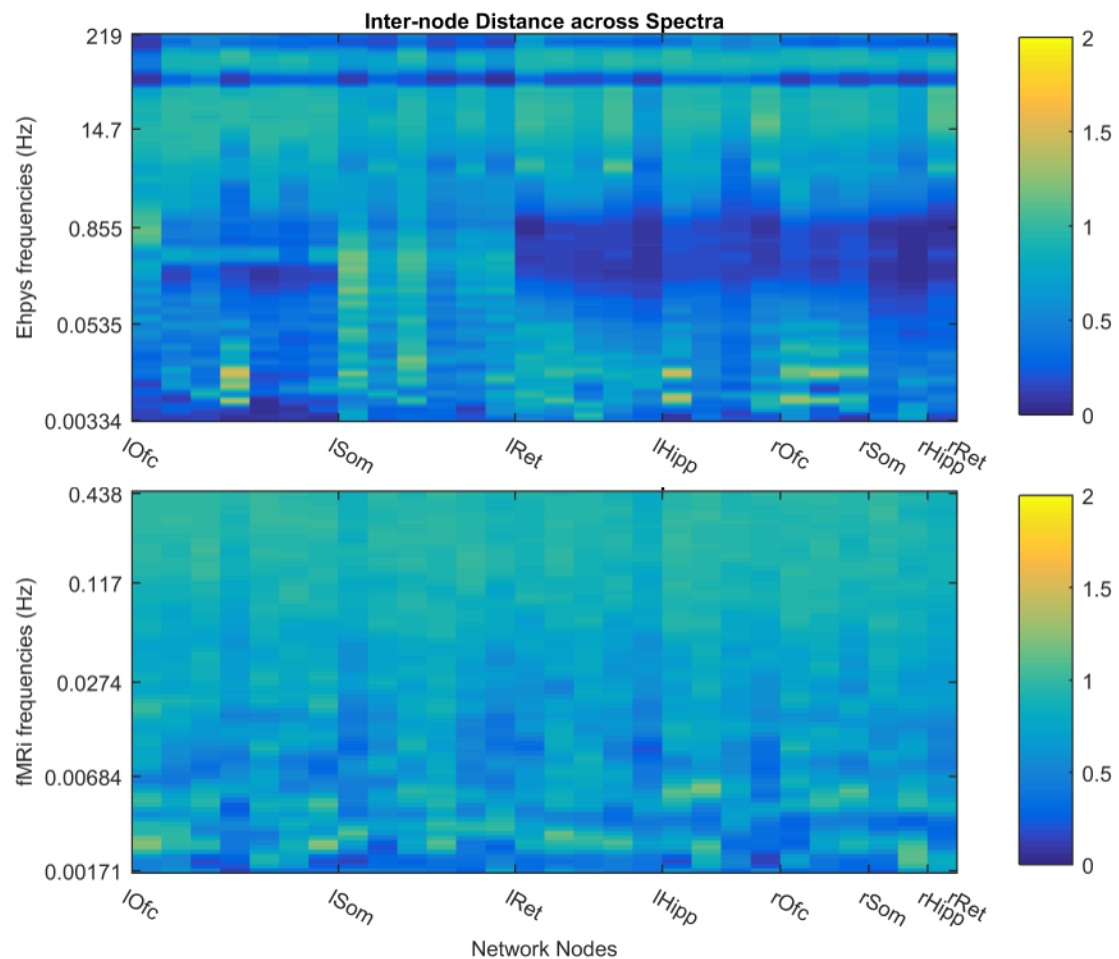


Figure 4.4: Spectrally delimited correlation distances between regions of interest (ROI). Top and bottom plots correspond, respectively, to ROIs from electrophysiology and magnetic resonance imaging. Columns to the left of each node label include that node in the pairwise distance operation. The second node in the pair is read out, in order, from the subsequently labeled nodes.

### 4.3. Results

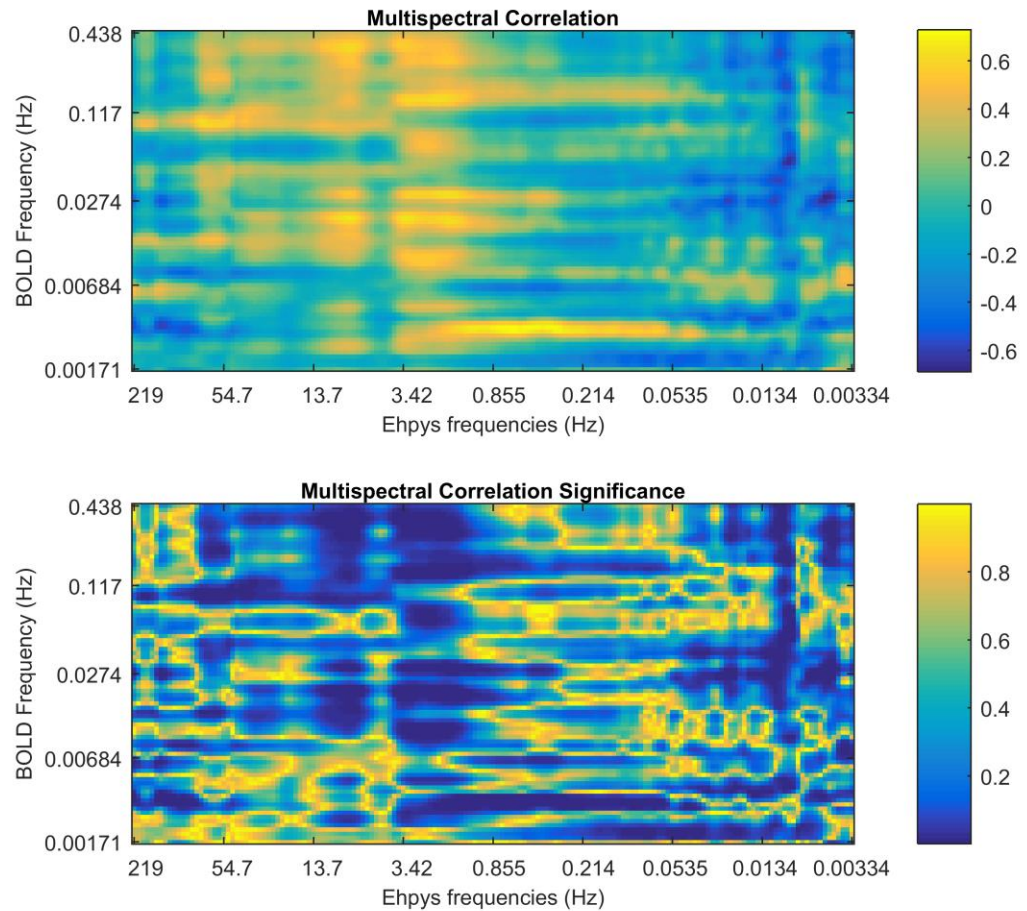


Figure 4.5: The correlation between multimodal functional connectivity graphs is plotted for multiple spectral combinations. The significance of each correlation value is included at bottom.

Cross-modal, multispectral functional connectivity network comparisons are plotted in figure 4.5. Inter-modal correlation reached a maximum magnitude of  $\pm 0.6$  (min/max  $\pm 1$ ). Many of these strongly (anti-) correlated areas have a p-value less than 0.05. Strongly (anti-) correlated and statistically significant regions are distributed across multiple spectral scales. BOLD networks between 0.01 and 0.4 Hz are positively correlated with LFP networks in delta (1-4 Hz) and alpha (8-12 Hz) bands. BOLD activity at  $\sim 0.1$  Hz is strongly correlated with gamma-band LFP (40-60 Hz). An additional band of strong correlation is found in very low

frequency BOLD and low frequency ephys (0.1 to 1 Hz). Significant infraslow (0.1 to 0.01 Hz) LFP network configuration is largely anticorrelated with BOLD inter-node distance.

#### 4.4. Discussion

The results demonstrate the existence of strong network correspondence between neuroelectric and hemodynamic signals. Results confirm findings from Pan and Thompson showing 1) broad coherence of LFP traces to simultaneous BOLD signals previous studies, and 2) strong correspondence between multi-modal sliding window correlation at delta and gamma bands (Pan, Thompson et al. 2011, Thompson, Merritt et al. 2013). Interestingly, infraslow BOLD network correlation decreases in the LFP gamma band relative to LFP activity in alpha and delta bands. Gamma band LFP is strongly correlated evoked BOLD potentials (Logothetis, Pauls et al. 2001). The reduction in gamma band correlation here may reflect the focus on ongoing network communication.

The broad anti-correlation observed in infra-slow LFP networks vs BOLD networks at most frequencies denotes that the magnitude of the modal network distances are the same, while their signs are different. Given strong positive correlations at higher frequencies, and the long-standing evidence from other neuroelectric studies that these higher frequency rhythms are directly involved in perception and cognition, low frequency LFP fluctuations may be demonstrating a lateralized oscillation of long-term membrane potentials.

FC rests upon a relationship between correlated blood supply and correlated signaling between brain sites. One foundational principle of this model is that the inter-regional communication picked up by the BOLD signal is conveyed via inter-regional white matter tracts. However, recent evidence that FC is maintained after complete resection of neuronal tissue between the temporal pole and the remainder of the caudal temporal lobe in 5 human epilepsy patients casts doubt on this prediction (Glomb, Ponce-Alvarez et al. 2017). Given that the evidence from Glomb et al. (2017) shows significantly reduced connectivity after resection, it may be that the remaining FC is sustained by an alternative mechanism than

neuroelectric signaling. One possibility is that neuromodulatory hormones diffuse throughout the cardiovascular system and tune spontaneous neuroelectric activity to share similar temporal properties. From the observations in the present study that neuroelectric activity is instantiated in BOLD networks at multiple frequencies, it may be that FC pre- and post-resection is derived from different spectral rhythms. Whereas fast, gamma-band connectivity may be lost after severing white matter connections, slower frequency coordination amenable to neuromodulatory fluctuations may yet remain. If such is the case, then BOLD FC may yet be a good representation of neuronal signaling rather than simply being a reflection of confounding events.

#### 4.5. Limitations and Future Directions

The DMN is associated with internal mental activity. And, the strength of DMN connectivity is responsive to the level of anesthetic, with decreased connectivity as humans and animals are drawn deeper into unconsciousness (Nallasamy and Tsao 2011). Network FC is also related to the type of anesthetic used (Magnuson, Thompson et al. 2014). This may be explained by each anesthetic's unique mechanism of action. While ISO is a GABA-agonist, DEX is an alpha-2 adrenergic receptor agonist (Peltier, Kerssens et al. 2005, Samuels and Szabadi 2008). In addition, DEX has vasoconstrictive properties, while ISO shows vasodilatory properties. This difference in state may account for the loss in the coordination of slow relationships between nodes. Future experiments should further investigate the effect of differing sedative conditions on network interaction.

## 5. Dynamic Brains: Visualizations through multiscale embedding

The advent of functional Magnetic Resonance Imaging (fMRI) has launched the brain sciences into an exciting frontier by allowing the direct observation of systems-wide activity from healthy human brains (Rosen and Savoy 2012). The richness of data this technology generates is the subject of cutting-edge research to interpret spontaneous signal fluctuations as indicators of preferential information exchange among the brain's intrinsic networks—i.e., its functional connectivity (FC) (Biswal, Yetkin et al. 1995, Hutchison, Womelsdorf et al. 2013). Brain FC networks were first defined over relatively long periods of time. Such *static* FC studies reveal that brain FC naturally develops a small-world topology, where densely connected local modules communicate with one another via richly interconnected hubs (Achard, Salvador et al. 2006, Bullmore and Sporns 2009). But the brain is not a static system. Rather, differential information exchange among neurons, circuits, and networks enable brains to deal flexibly with ever-changing environmental stimuli. The availability of rapid ( $< 1$  s), whole-brain imaging prompted researchers to look for shorter term *dynamics* of brain FC (Deco, Jirsa et al. 2011).

Early efforts to characterize brain dynamics observed that intra-network membership and inter-network communication possessed statistically significant differences when samples were drawn from short time windows during various epochs of an fMRI scan (Chang and Glover 2010, Smith, Miller et al. 2012, Keilholz, Magnuson et al. 2013, Zalesky, Fornito et al. 2014). While these short time window studies confirmed the expectation that the Blood-Oxygen Level Dependent (BOLD) fMRI signal may convey information about short-term brain-state dynamics, the large effect that *a priori* choices in window length had on study results lessened the method's analytic utility (Shakil, Lee et al. 2016). The effort to identify rapidly changing dynamics is also hampered by the drop-off in bold SNR at short window lengths.

To avoid the problems inherent in windowed analysis techniques, we present a method that provides a 2D map of the relative similarity of the brain's activity for all time points in the scan. The signal from each voxel first undergoes wavelet decomposition, making use of the BOLD signal's natural spectral scaling to characterize each time point as a summation of activations at multiple frequencies (Chang and Glover 2010, Billings, Medda et al. 2015, Yaesoubi, Allen et al. 2015). This multispectral interpretation has been suggested to provide a parsimonious representation of the dynamic properties of complex systems like brains (Mandelbrot 1983, Mallat 1989, Bullmore, Fadili et al. 2004, Ciuciu, Varoquaux et al. 2012). To reduce the redundancy of spatial information and improve the SNR, voxel-wise signals are aggregated into a lower-dimensional spatial parcellation using Independent Component Analysis (ICA). In the present study, we treat the collected vectors of multispectral activations from all of the ICA networks at each time point as samples of instantaneous brain states.

The dimensionality of the resulting data set is high (equal to the product of the number of functional networks and the number of spectral filters) and difficult to interpret. In order to explore the dynamics of brain activity, we apply t-distributed stochastic neighbor embedding (t-SNE) to represent the data from each time point in a two dimensional space (van der Maaten and Hinton 2008), using correlation as a distance measure to ensure that similar states are grouped together. t-SNE is a state of the art data-driven dimensionality reduction algorithm that maintains local distance structure and has found wide application in the data-driven sciences to produce visualizations of *drosophila* behavior, machine learning hidden layers, static functional connectivity networks, and a host of other multidimensional structures (Berman, Choi et al. 2014, Plis, Hjelm et al. 2014, Mnih, Kavukcuoglu et al. 2015). In comparison to clustering based approaches that segment the time course into a number of predefined states, the map created by t-SNE produces a continuous distribution that can then

be segmented empirically (using the watershed algorithm in this study). Information about the timing and the relative similarity of different states is preserved.

Towards the goal of detailing a map of brain-state dynamics, the present study analyzes the wide-ranging states 446 normal volunteers adopt as part of the Human Connectome Project (HCP)(Van Essen, Ugurbil et al. 2012). BOLD fMRI scans from 7 distinct tasks (EMOTION, GAMBLING, LANGUAGE, MOTOR, RELATIONAL, SOCIAL, and WORKING MEMORY (WM)), and from repeated resting conditions (REST1, and REST2) provide a basis to segment a t-SNE embedding of brain-state dynamics across experimentally defined events. We demonstrate the utility of the t-SNE mapping to characterize the human brain's coordination across time, space, and spectra during rest and in the negotiation of changing experimental stimuli.

## 5.1. Methods

### 5.1.1. *Data Acquisition*

The data for this study was obtained by leveraging the library of resting-state and task fMRI images from the Human Connectome Project (HCP), a joint project between Washington University and the University of Minnesota (Van Essen, Ugurbil et al. 2012). These data were acquired using a customized Siemens 3T “Connectome Skyra” and the 32 channel, anterior/posterior, head receive coil. T1 weighted anatomical scans were acquired via a 3D MPRAGE sequence with  $TR = 2400$  ms,  $TE = 2.14$  ms,  $TI = 1000$  ms, flip angle of  $8^\circ$ ,  $FOV = 224 \times 224$  mm, and voxel size 0.7 mm isotropic. BOLD-weighted fMRI images were acquired via a gradient-echo EPI sequence with  $TR = 720$  ms,  $TE = 33.1$  ms, flip angle of  $52^\circ$ ,  $FOV = 208 \times 180$  mm, 72 slices, 2.0 mm isotropic voxels, and multiband factor of 8. Functional scans imaged individuals while they adopted a comprehensive battery of states. These states may be subdivided into the 9 scans named as follows: REST1, REST2, EMOTION, GAMBLING, LANGUAGE, MOTOR, RELATIONAL, SOCIAL, and WORKING MEMORY (WM). Each scan was performed twice for each volunteer, each time with an opposite phase encoding gradient (left to right, vs right to left). In total, each individual contributed 8,680 temporal and 91,282 spatial data points. REST scans spanned 4,800 time points. All data were de-identified before download.

### 5.1.2. *Data Preprocessing*

Data preprocessing include spatial artifact and distortion removal, surface generation, anatomical registration, and alignment to grayordinate space (gray-matter vertices or voxels). Subsequent use of spatial filters from a separate Independent Component Analysis (ICA) assume that data follow an isotropic noise model; thus, all voxel time series are normalized to

zero mean and unit variance. To reduce the influence of edge effects during spectral filtering, contiguous, 300 image segments from a volunteer’s REST scans were placed in-between their task scans. The remaining 900 REST images capped the beginning and the end of the concatenated series with 450 time points each. The order of concatenated rest and task images were randomized across volunteers.

### 5.1.3. *Spectral and Spatial Filtering*

The BOLD signal bears a log linear relationship between power spectrum and frequency:  $\log S(f) = c + \gamma \log f$ ; alternatively,  $S(f) \sim 1/f^\gamma$ . For the average BOLD signal in brains, the power law exponent,  $\gamma \cong -1$ . The variable  $c$  is a constant. Such ‘1/f-type’ systems denote that the system’s high-frequency realizations establish and maintain its low-frequency structure (Wornell 1993). The simplest 1/f-type systems are termed, ‘scale-free,’ that is, one observes rescaled versions of some elementary process, a “fractal”, at all observable scales. On the other hand, complex 1/f-type systems exhibit emergent properties at multiple scales (Ciuciu, Varoquaux et al. 2012, He 2014, Liu, Ward et al. 2014). A theoretically optimal method for observing 1/f-type processes is to transform them using a scale-free, or multiresolution, basis set (Bullmore, Fadili et al. 2004, Ciuciu, Varoquaux et al. 2012). Coefficient variance in the scale-free domain is thus a representation of the emergence of novel signal characteristics resolved to one or more scales (Daubechies 1992). Wavelet transforms are especially useful multiresolution transforms as their kernel functions reduce to zero over a finite time-span. By convolving a 1/f-type signal with a finite, scale-free kernel, wavelet transforms highlight the signal’s dynamical properties in both the temporal and the spectral domains.

Previous studies demonstrated that BOLD data segment into static FC subnetworks from the application of multiscale filter banks (Billings, Medda et al. 2015). In the present study, spectral filtering utilized the continuous wavelet transform with a Daubechies 4-tap wavelet. This continuous wavelet filterbank segmented BOLD signals into an octave of 8 frequency bands log-spaced across the decade [0.01, 0.1] Hz. This frequency range corresponds to the low-frequency fluctuation range in which BOLD fluctuations bear maximal information about neuronal activity. The mother wavelet, Daubechies 4-tap, was chosen to achieve a relatively short temporal window over each spectral band, while the number of bands is sufficient to capture the inter scale network variation observed by Billings et al. (2015).

Spatial filtering utilized a 50-component ICA decomposition. The ICA transform matrix was calculated as part of the HCP beta-release of group-ICA maps (Human Connectome Project 2014). The number of components was chosen by identifying the intersection between the eigenvalues of a volunteer’s real concatenated input data matrix, and a randomly shuffled version of that matrix, and choosing a number of components that just exceeded this point of intersect (data not shown).

#### 5.1.4. *Manifold Embedding*

Each temporal sample for each volunteer’s high-dimensional state descriptor (50 spatial components by 8 spectral components) was pairwise compared using the Pearson correlation distance,

$$\begin{aligned}
 d_{ij} &= \|x_i - x_j\| \\
 &= 1 - \frac{(x_i - \bar{x}_i)(x_j - \bar{x}_j)'}{\sqrt{(x_i - \bar{x}_i)(x_i - \bar{x}_i)'}\sqrt{(x_j - \bar{x}_j)(x_j - \bar{x}_j)'}}
 \end{aligned} \tag{5.1}$$

Because of the theoretically optimal whitening properties of the wavelet transform, and because we have normalized time series via z-scoring, the Pearson correlation distance highlights coordinated deviations from normative spectral intensities.

Manifold embedding was performed with the algorithm t-Distributed Stochastic Neighborhood Embedding (t-SNE) (van der Maaten and Hinton 2008, van der Maaten, Postma et al. 2009, Berman, Choi et al. 2014). The algorithm begins by transforming high-dimensional pairwise distances into conditional probabilities,  $p_{j|i}$ , along a Gaussian probability distribution,

$$p_{j|i} = \frac{\exp\left(-\frac{\|x_i - x_j\|^2}{2\sigma_i^2}\right)}{\sum_{k \neq i} \exp\left(-\frac{\|x_i - x_k\|^2}{2\sigma_i^2}\right)}. \quad (5.2)$$

The variable  $\sigma_i$  is equal to the variance of the high-dimensional data when multiplied by a Gaussian centered over point  $i$ . The width of each Gaussian is adjusted to cover an equivalent amount of points. Formally, the width is adjusted until the base 2 exponent of the Shannon entropy measured in the stochastic distribution around the  $i^{\text{th}}$  point achieves a fixed value termed the perplexity. For the present study, we follow the recommendation from van der Maaten & Hinton (2008) of a perplexity equal to 30. Collectively, the transformation from inter-sample distances to conditional probabilities emphasizes the natural associations of each sample to its neighbors. The authors of t-SNE also described a problem with previous implementations of SNE-based algorithms wherein moderately dissimilar samples, in the high-dimensional space, crowd together in the low-dimensional map (van der Maaten and Hinton 2008). Therefore, t-SNE calculates the low-dimensional probabilities,  $Q$ , using a distribution having a much longer tail than in the high-dimensional case. A good choice to avoid this problem was found to be the Student t-distribution with one degree of freedom:

$$q_{ij} = \frac{(1 + \|y_i - y_j\|^2)^{-1}}{\sum_{k \neq l} (1 + \|y_k - y_l\|^2)^{-1}}, \quad (5.3)$$

where  $\|y_i - y_j\|$  is the Euclidean distance between samples  $i$  and  $j$  in the low-dimensional space.

A natural cost function,  $\mathcal{C}$ , to calculate the fidelity of the low-dimensional representation relative to the high-dimensional data is the Kullback-Liebler (KL) divergence which is related to the cross-entropy between the two distributions. A symmetrized version of the KL divergence is used here to expedite computation time and to balance the cost of representing points that are close together in the high-dimensional space as distant points in the low-dimensional space, and vice-versa. Thus,

$$\mathcal{C} = \sum_i \text{KL}(P||Q) = \sum_i \sum_j p_{ij} \log \frac{p_{ij}}{q_{ij}}. \quad (5.4)$$

The joint probabilities in the high-dimensional space are calculated as  $p_{ij} = \frac{p_{ji} + p_{ij}}{2n}$ , where  $n$  are the number of samples.

This collective description of high-dimensional and low-dimensional spaces, as well as the relationship between them, emphasizes both that similar map points are modeled by small pairwise distances and that dissimilar map points are modeled by large pairwise distances. This is the case at all but the finest scales, at which point, the numerator of equation (5.3) is dominated by a constant rather than by variations from the input data. The t-SNE algorithm is implemented as a gradient descent process. The form of the gradient, as well as detailed notes on methods to improve the speed of convergence may be found in van der Maaten and Hinton (2008).

The initial construction of a t-SNE embedding is computationally expensive:  $O(n^2)$ . For a compute node having 256 GB of RAM, the maximum number of double precision data

points that may be included in a single t-SNE embedding is limited to about 90,000 samples. The full complement of 4 resting state scans and 14 task scans contains 8,680 images for each of the 446 included volunteers. To overcome the computational limits of embedding larger datasets, the present study follows the recommendations from Berman et al. for training a low-dimensional embedding space from a subsampling of data points (Berman, Choi et al. 2014). Briefly, t-SNE embeddings were generated from each of 446 volunteers, individually. Next, 200 sample points were pulled from each volunteer’s embedding, at random, and in proportion to the density of points within the embedding. A group-level embedding was then trained from each volunteer’s sample of 200 time points. The best low-dimensional locations of the remaining time points vis-à-vis the trained embedding were then calculated in two steps: 1) Approximate the out-of-sample point’s low dimensional location as a weighted sum of its nearest neighbors in the full high-dimensional space. 2) Determine the local KL divergence minimum by changing only the location of the out-of-sample point. As this minimization is not convex, it is worthwhile to jitter the out-of-sample point’s initial low-dimensional location by sampling from a range of its high-dimensional neighbors. This procedure reduces the computational load to  $O(n)$ . The subsampling procedure greatly increases the interpretability of the resulting map by removing the bias experienced among sequentially sampled points—and hence, temporally correlated points—when they are embedded simultaneously.

#### 5.1.5. *Sub-Space Identification and Characterization*

One method to summarize 2-dimensional point distributions is by convolution with a Gaussian filter. In order to account for both coarse and fine features of the embedded distribution, two filter radiuses were selected for the present study—one at  $1/32$  the maximum displacement from the map center and the other at  $1/256$ . Particularly dense map regions are

segmented from one another, in a data-driven fashion, by taking the watershed transform of the inverse of each density map (Meyer 1994).

#### 5.1.6. *Velocity Field*

Instantaneous velocities, were calculated by taking the difference in the embedded location of successive sample points. The group-level displacement magnitude was averaged, separately, in each of the 4 cardinal Euclidean directions,  $-i$ ,  $+j$ ,  $+i$ , and  $-j$ , for each point in a  $32 \times 32$  grid. Results were normalized to unit magnitude.

#### 5.1.7. *Comparing Embeddings*

Embeddings were segmented against the HCP’s experimentally defined states, i.e. the resting-state and the task-based scans. To test the inference that scan-segmented maps depicted distinct brain-state distributions, we conducted an ANOVA with multiple comparisons testing using a bootstrapped sample of each experimentally defined state. Points within each bootstrap realization were chosen from segmented group-level datasets. The lower bound to the number of points in each bootstrap realization sample was chosen to ensure a full coverage of the state’s embedded range. The upper bound was chosen to ensure that few points were sampled twice in any two bootstrap realizations.

Bootstrap realizations were pairwise compared using the Structural Similarity Index (SSIM) (Zhou, Bovik et al. 2004). SSIM measures the similarity between two images,  $x$  and  $y$ , as the multiplicative combination of three image quantities, the cross-luminance,  $I$ , cross-variance,  $c$ , and cross-structure,  $s$ . Thus:

$$SSIM(x, y) = [I(x, y)]^\alpha \cdot [c(x, y)]^\beta \cdot [s(x, y)]^\gamma, \quad (5.5)$$

where

$$I(x, y) = \frac{2\mu_x\mu_y + C_1}{\mu_x^2 + \mu_y^2 + C_1}, \quad (5.6)$$

$$c(x, y) = \frac{2\sigma_x\sigma_y + C_2}{\sigma_x^2 + \sigma_y^2 + C_2}, \quad (5.7)$$

$$s(x, y) = \frac{\sigma_{xy} + C_3}{\sigma_x\sigma_y + C_3}, \quad (5.8)$$

and where  $\mu_x, \mu_y, \sigma_x, \sigma_y,$  and  $\sigma_{xy}$  are the local means, standard deviations, and cross-covariance for images  $x, y$ . The values  $C_1, C_2,$  and  $C_3$  are small constants given by  $C_1 = (K_1L)^2, C_2 = (K_2L)^2,$  and  $C_3 = C_2/2$ . Here  $L$  is the dynamic range of pixel values. The variable  $K_1 \ll 1,$  and the variable  $K_2 \ll 1$ . The exponents over each SSIM term were set to 1 so as to weight each term equally. SSIM values range between 0, no image similarity, and 1, complete image similarity. SSIM statistical testing was conducted simultaneously for all SSIM pairs (50\*50/2 independent comparisons). Maps were deemed to provide insignificant segmentation if the 95% confidence interval of the within-state SSIM fell within or below the range of any of its between-state SSIM 95% confidence intervals. The multivariate construction of the SSIM algorithm makes it a useful technique for quantifying the differences between density maps. Density maps contained equal numbers of points to ensure that the SSIM metric to remain balanced.

#### 5.1.8. *Real-Time Dynamics*

Group level brain-state dynamics are characterized through map segmentation at the level of each task's block-design contrasts. For instance, MOTION task blocks are segmented into movement of the tongue, the left hand, right hands, etc. The total set of block-design contrasts, from all individuals and from each individual's task repetitions, are aligned at time  $t = 0s$ , the start of the block (including the cue, if present). Group level density images are then

calculated for each aligned image acquisition. The resting state was aligned to a single time point.

#### 5.1.9. *Permutation Testing for Labeling the Embedded map.*

To test the preference of labeled times and conditions for particular map regions, a null distribution was constructed by randomly permuting the labels assigned to each embedded point. Thereafter, it is possible to compare the mean number of points randomly assigned to each region, under a particular condition/time, with the actual number of points in that region, at that same condition/time. Map regions may then be labeled in terms of the preference of each region for particular condition/times.

## 5.2. Results

To test the degree to which resting and tasked brains develop distinct dynamics, we segmented time points during the REST1 and REST2 scans from all task-scan time points. The results are displayed as density maps in part A of figure 5.1. The resting brain tends to adopt a range of states in the map's periphery, while the task-active brain tends to develop brain states at the map's interior. To represent the brain's dynamic transitions across the embedded state space, part B displays point-to-point state changes as a velocity field. The results demonstrate that the resting brain's most rapid transitions occur in regions densely populated during tasks. In the task-active segmentation, the highest velocities are found at the map's center, between two interior regions densely populated during tasks. Regions of low velocity are distributed in patches throughout the task segmentation.

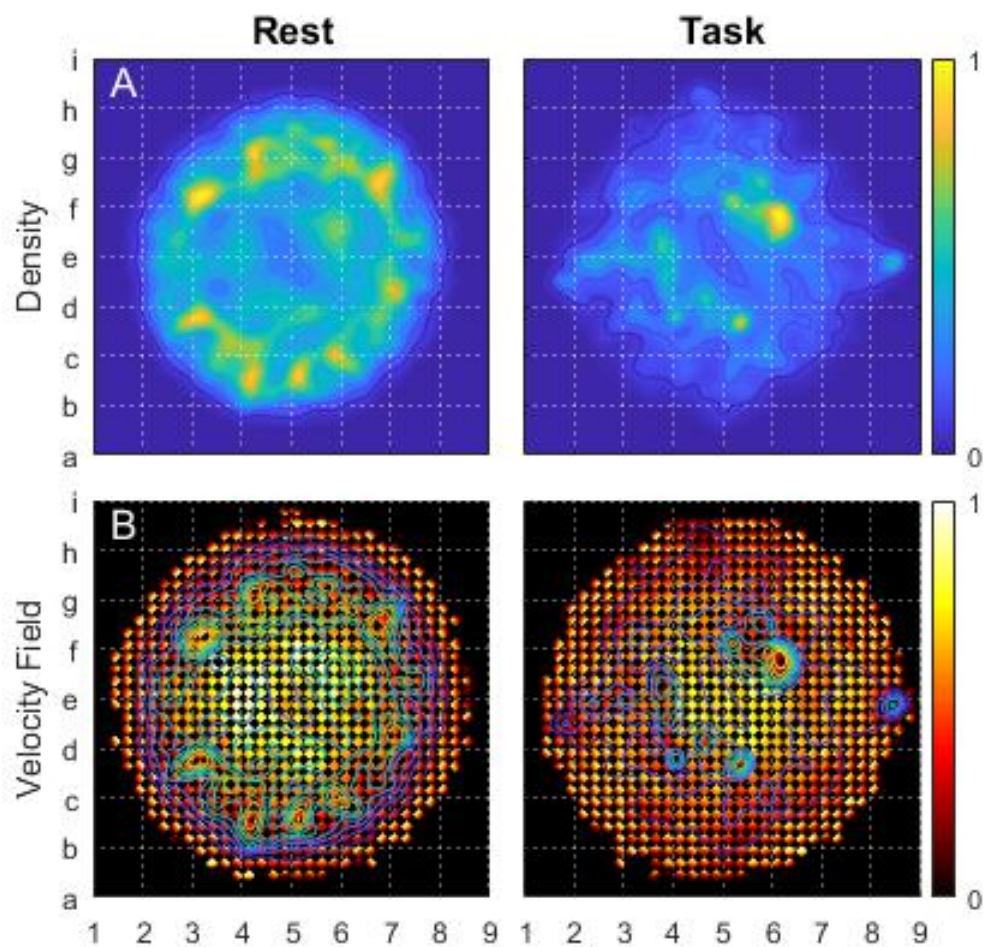


Figure 5.1 compares 2D Euclidean embeddings of instantaneous brain states, separated for the resting state and the task-active state. For ease of reference, the embedding space is divided into an  $8 \times 8$  grid. Alphanumeric labels mark grid vertices. Part A displays the distribution of embedded points as a Gaussian cloud. The Gaussian filter radius equaled  $1/32$  the maximum point displacement from the embedding's center. Part B displays the velocity field from an aggregation of points within a  $32 \times 32$  grid in each of the 4 cardinal directions across the map space. All results were normalized to unit magnitude.

While the embedding is a continuous state space, the presence of multiple densely populated regions suggests an ensemble of discrete states that the brain adopts. Figure 5.2 takes on a discretized perspective by tracing boundaries around the resting-state segmentation's dense regions. Formally, each state-space parcel is a catchment basin formed by taking the watershed transform of the density map's inverse (Meyer, 1994). Part A of the figure codes regions in terms of the percentage of points in each parcel. Owing to its sheer size, a sprawling domain in the map's interior contains the largest proportion of samples (4% to 5%, magenta boarder). The brain's propensity for adopting configurations within this parcel increases during task scans, when 6% to 7% of points form a similar density (see figure 5.3). The average brain state within this region sustains relatively slow ( $\sim 0.019$  Hz), low-amplitude, in-phase activations across most of the brain's static networks (part A, right) (see figure 5.4 for a description of each network). The region is often populated during the fixation periods of most tasks (see the supplemental movie).

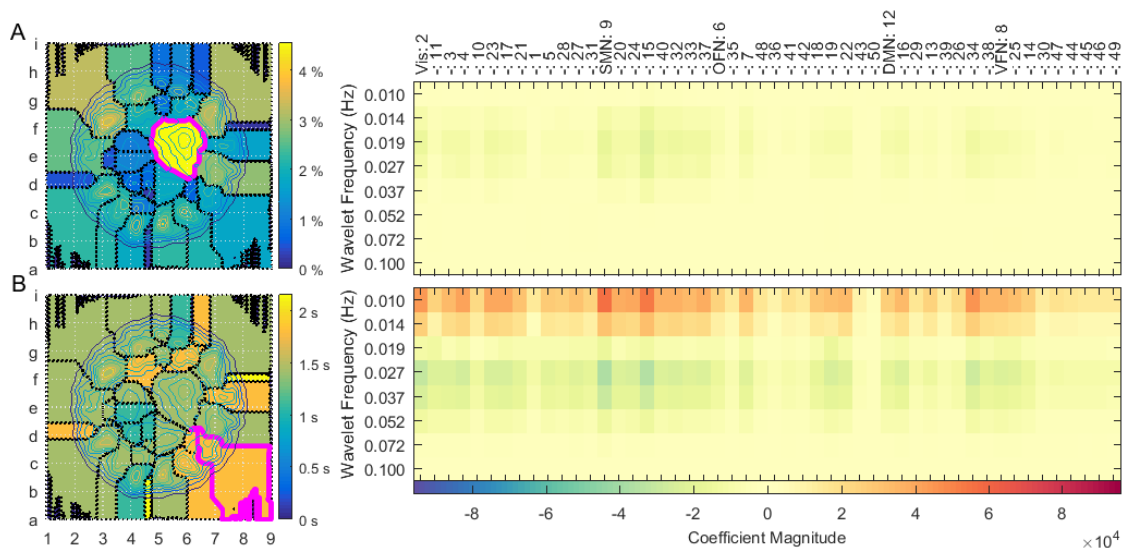


Figure 5.2 highlights the brain states adopted within watershed regions of the embedding space as participants reside in the resting-state. Part A (left) displays the percentage of points lying within each region. Part B (left) displays the median amount of time participants dwelled in each region. A similar analysis is performed for the task data in figure 5.3. The mean spatio-spectral brain state from the regions highlighted in magenta (left) are charted to the right. Each of the 50 ICA resting-state networks are categorized into one of five classes: 'Vis,' visual network; 'SMN,' somatomotor network; 'OFN,' orbito-frontal network; 'VFN,' ventral-frontal network.

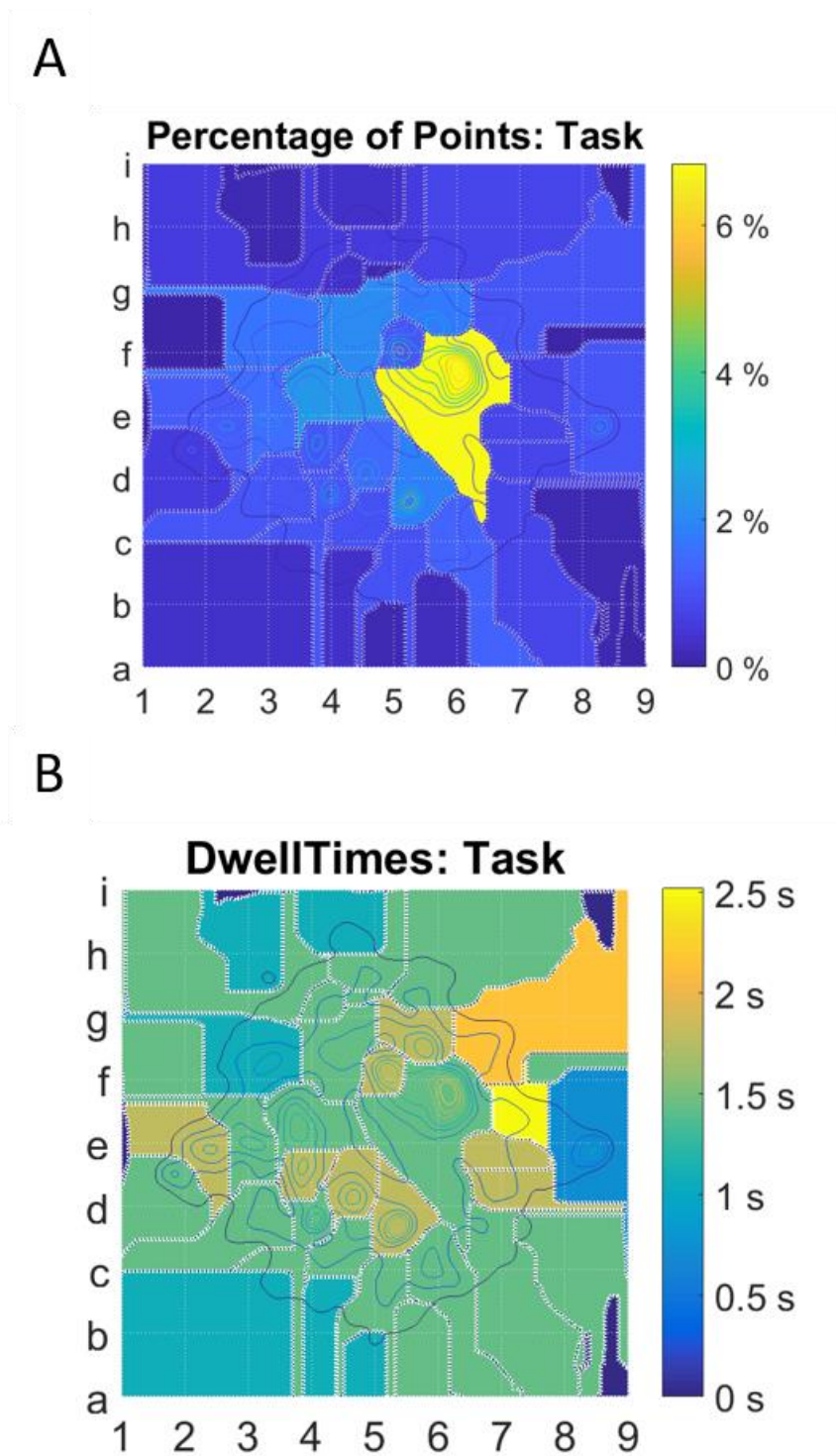


Figure 5.3 elaborates on the point distributions within watershed catchment-basins for task-active maps. Part A displays the percentage of points contained within each region. Part B displays the dwell-time for each region, reported as the mean number of temporally contiguous points contained within each region.

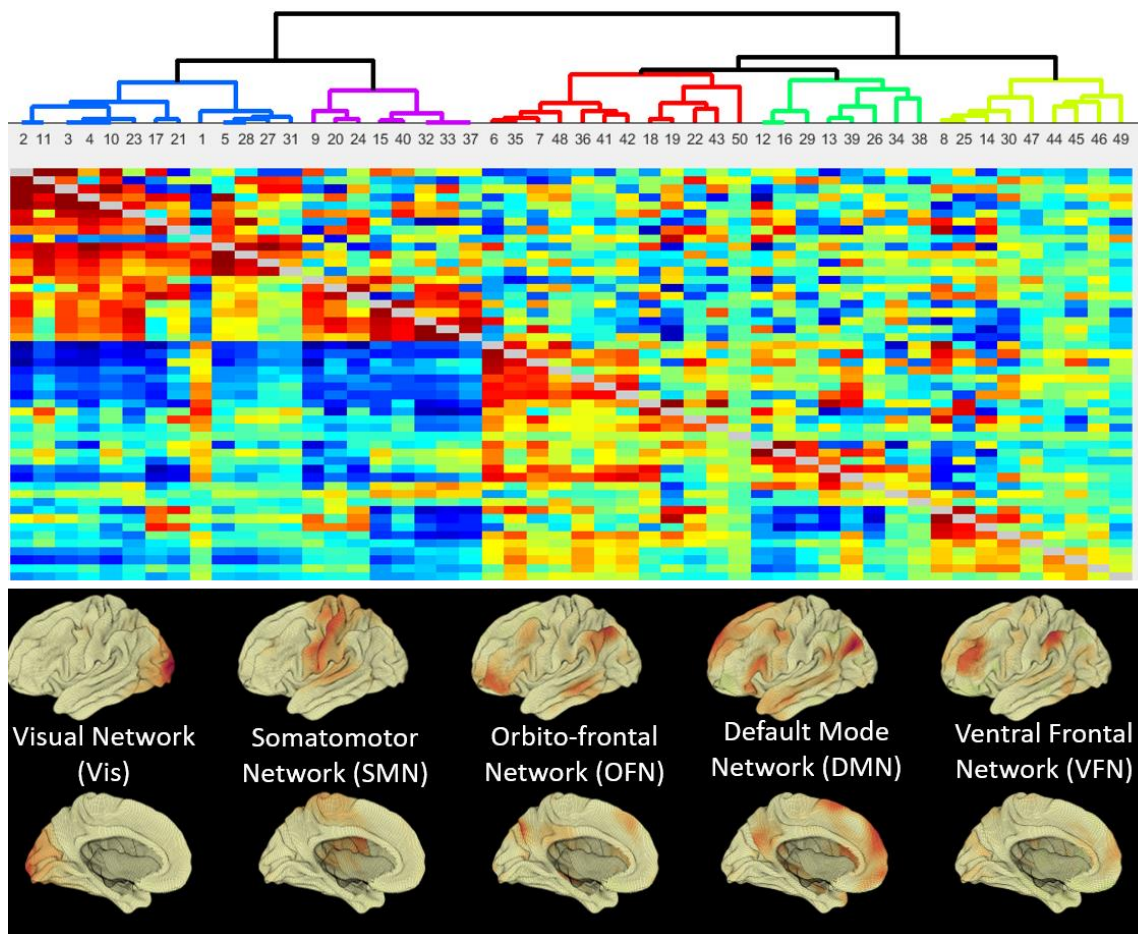


Figure 5.4 displays the relatedness between each of the 50 ICA components. Data were generated using the FSLNets toolbox provided through the HCP. The hierarchical clustering map was calculated from time-series from each ICA network back-projected for each volunteer included in the original analysis. The projection onto the brain of each of 5 ICA clusters is also shown.

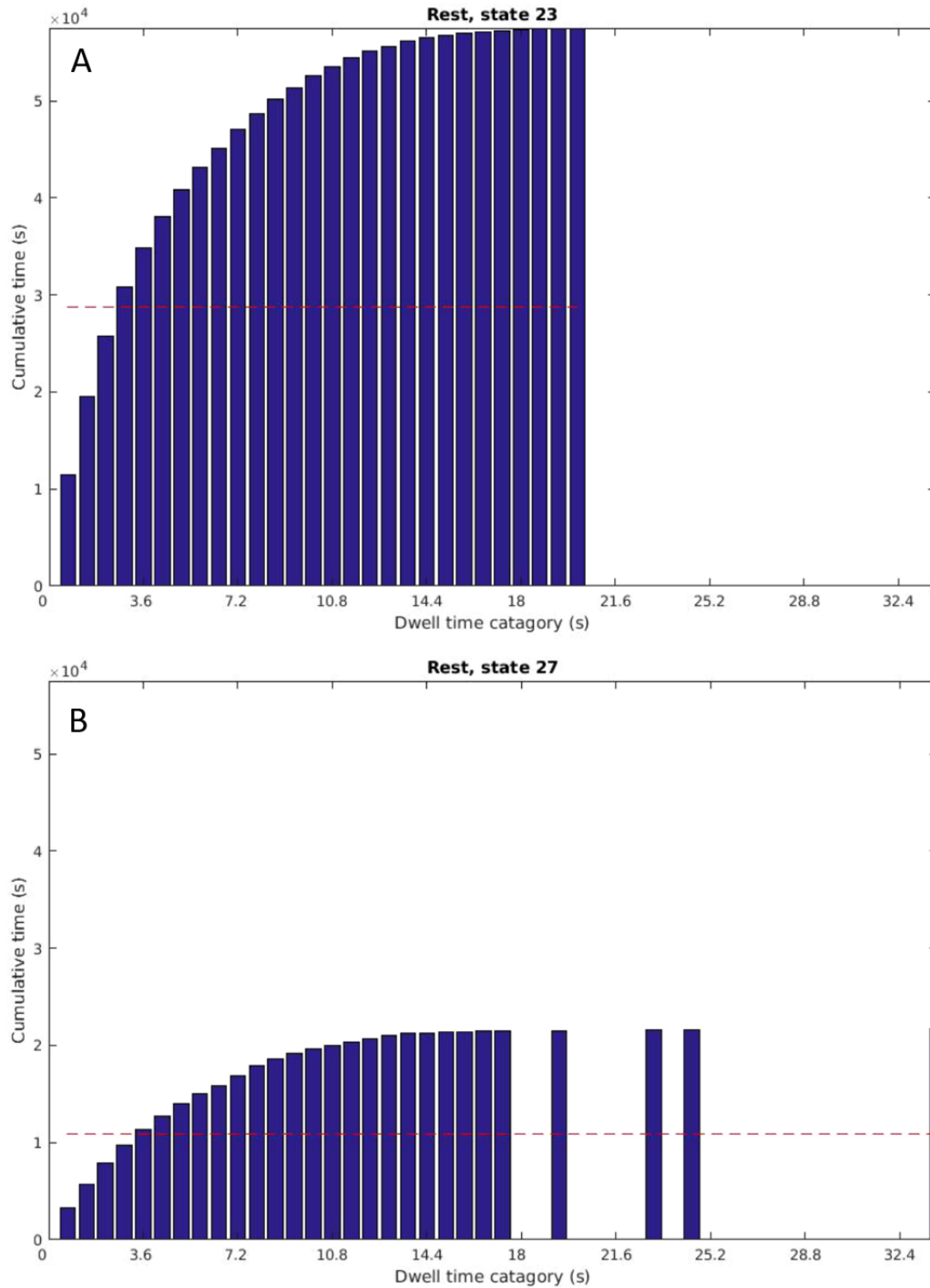
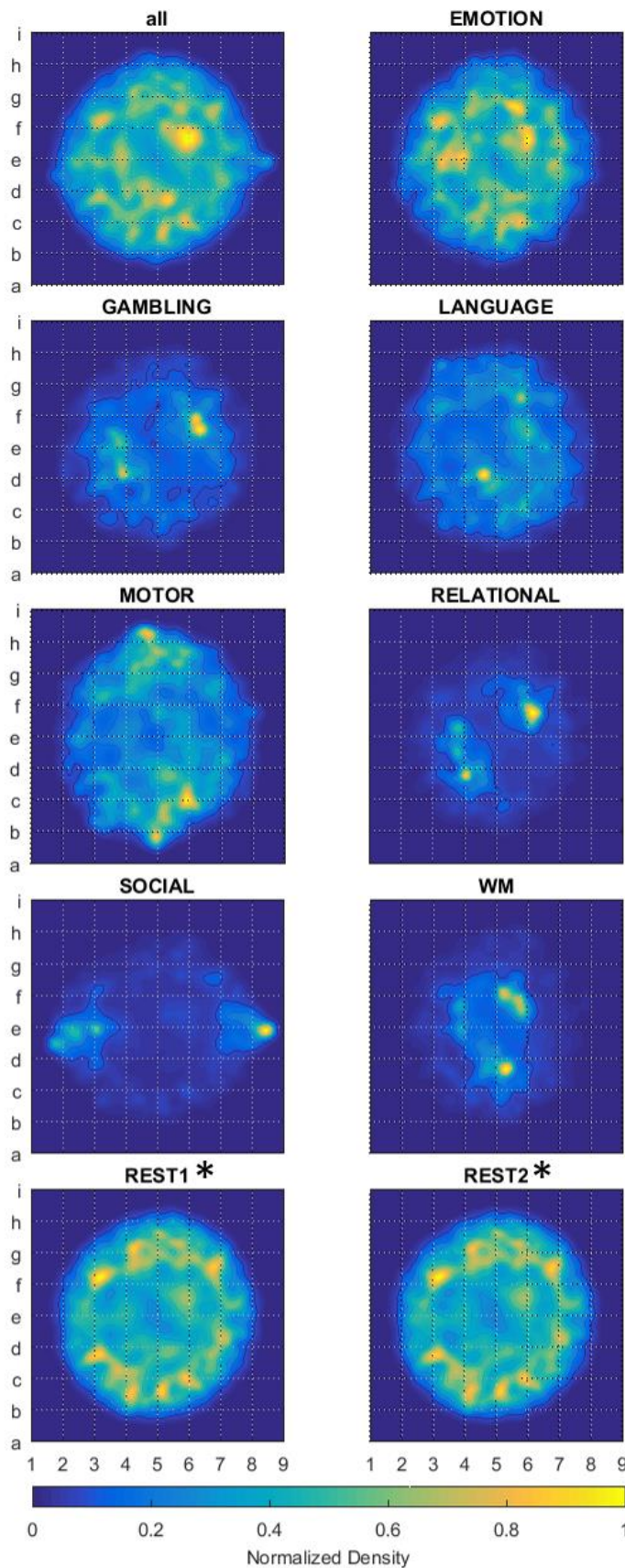


Figure 5.5 displays the dwell-time distribution for the highlighted regions in parts A and B (respectively) of figure 5.2.

To gain a better understanding of the dynamic characteristics of resting-state parcels, part B of figure 5.2 displays the median time volunteers continuously dwelt in each parcel. Although maximum resting-state dwell times reached as high as 30 s (see figure 5.5), median



dwell times did not exceed 2.5 s during rest. This finding is a confirmation that the resting brain often transitions between states. Dwell times tended to increase in duration during tasks (see figure 5.3). The mean brain state of one region having a long dwell time (magenta boarder) shows the brain to sustain activations in the same ICA networks as the state highlighted in part A. However, the second region's activations increase in magnitude. Further, they occur in two separate frequency bands, with either band's activations flipped to the opposite phase from the other.

The wide range of experimental states adopted

*Figure 5.1 displays t-SNE embeddings of instantaneous brain states, segmented by scan, and represented as the normalized density of each scan's embedded points. Task datasets include BOLD images during all periods of the scan, including any cue events, all contrasting task stimuli, any responses from volunteers, and any fixation blocks. The Gaussian filter radius equaled  $1/32$  the maximum point displacement from the embedding's center*

during HCP scans provides a natural means to segment instantaneous brain-states. Figure 5.6 displays group-level map densities produced by such a segmentation. Bootstrap sampling provided a sample distribution to assess structural image similarity within-states, and also between-states (figure 5.7). Larger within-scan SSIM values indicate that the brain adopts a tighter range of states during the scan. Comparatively large between-scan SSIM values indicate that the two scans evoke similar varieties of brain states. Multiple comparisons statistics performed on these results determined that the repeated resting-state scans, alone, bear statistically similar continuous state distributions (see figure 5.8). Figure 5.9 displays the results of the same analysis when data are segmented against all block-design contrasts and task-related events.

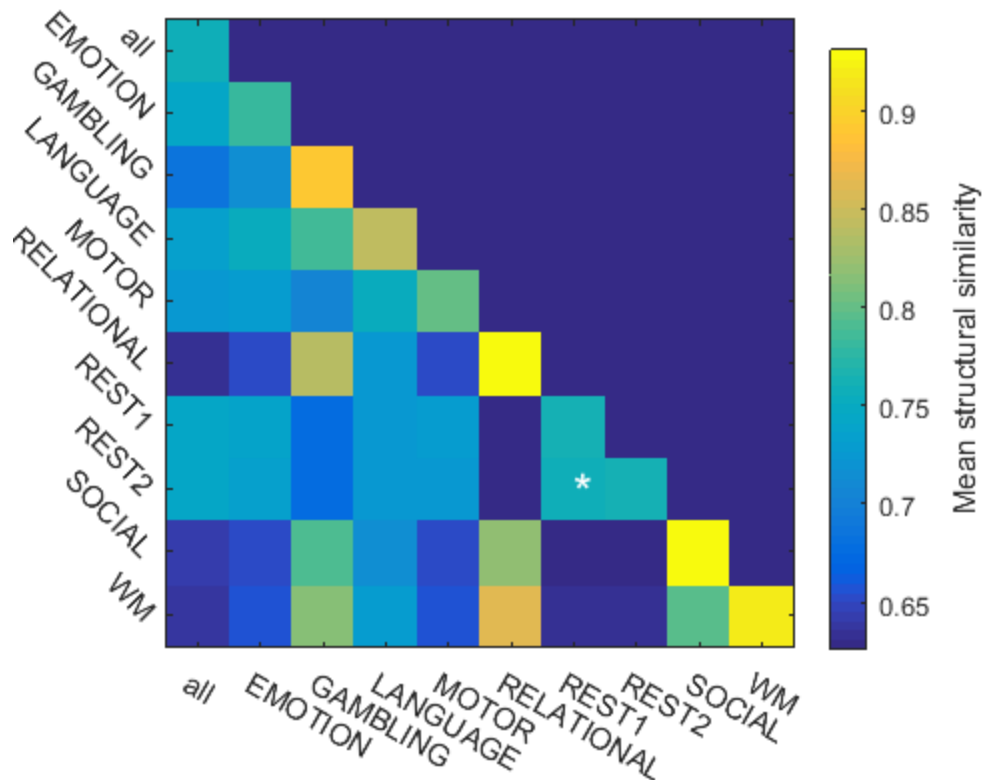


Figure 5.7 plots the mean structural similarity index (SSIM) between normalized density embeddings, segmented across scans. For each scan type, the sample distribution was bootstrapped from 50 realizations of 2500 timepoints, randomly sampled from the group-level data set. The number of time points provides a representative sampling of each scan's embedded distribution. Asterisks indicate between-scan comparisons whose mean SSIM was not significantly less than either within-scan mean SSIM.

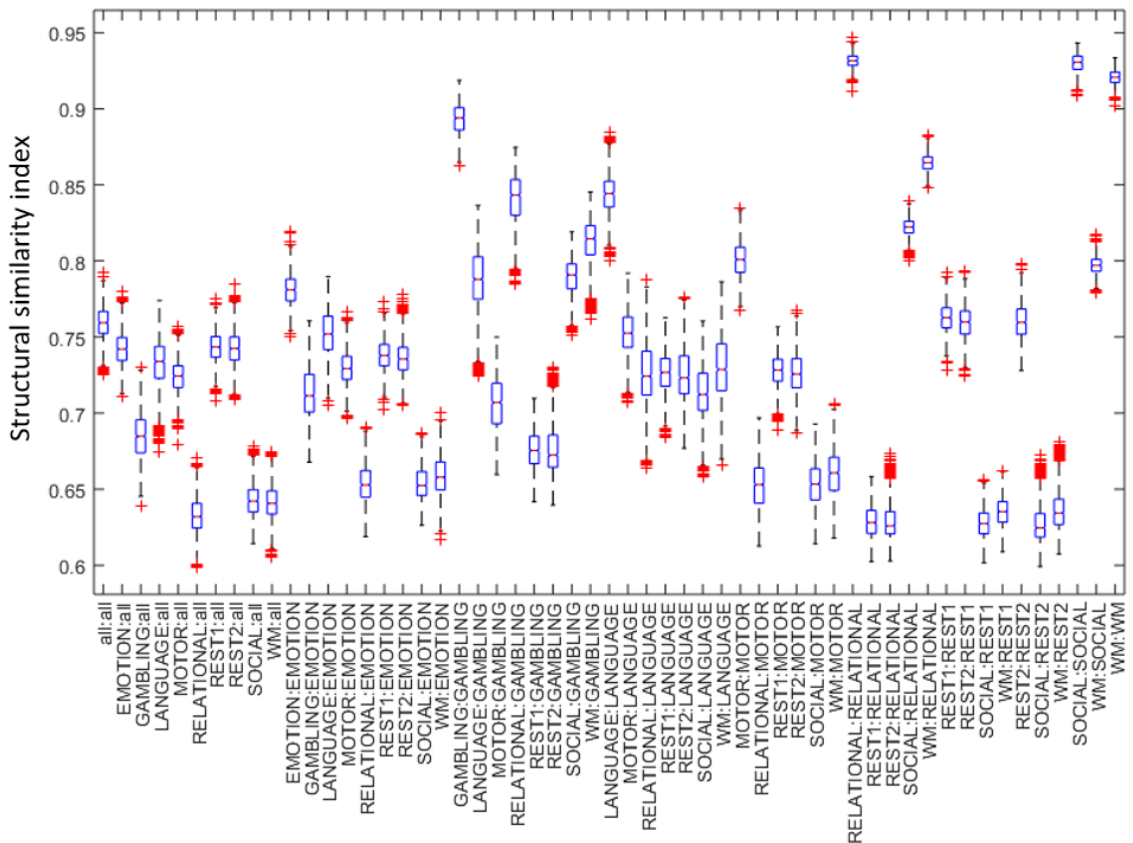
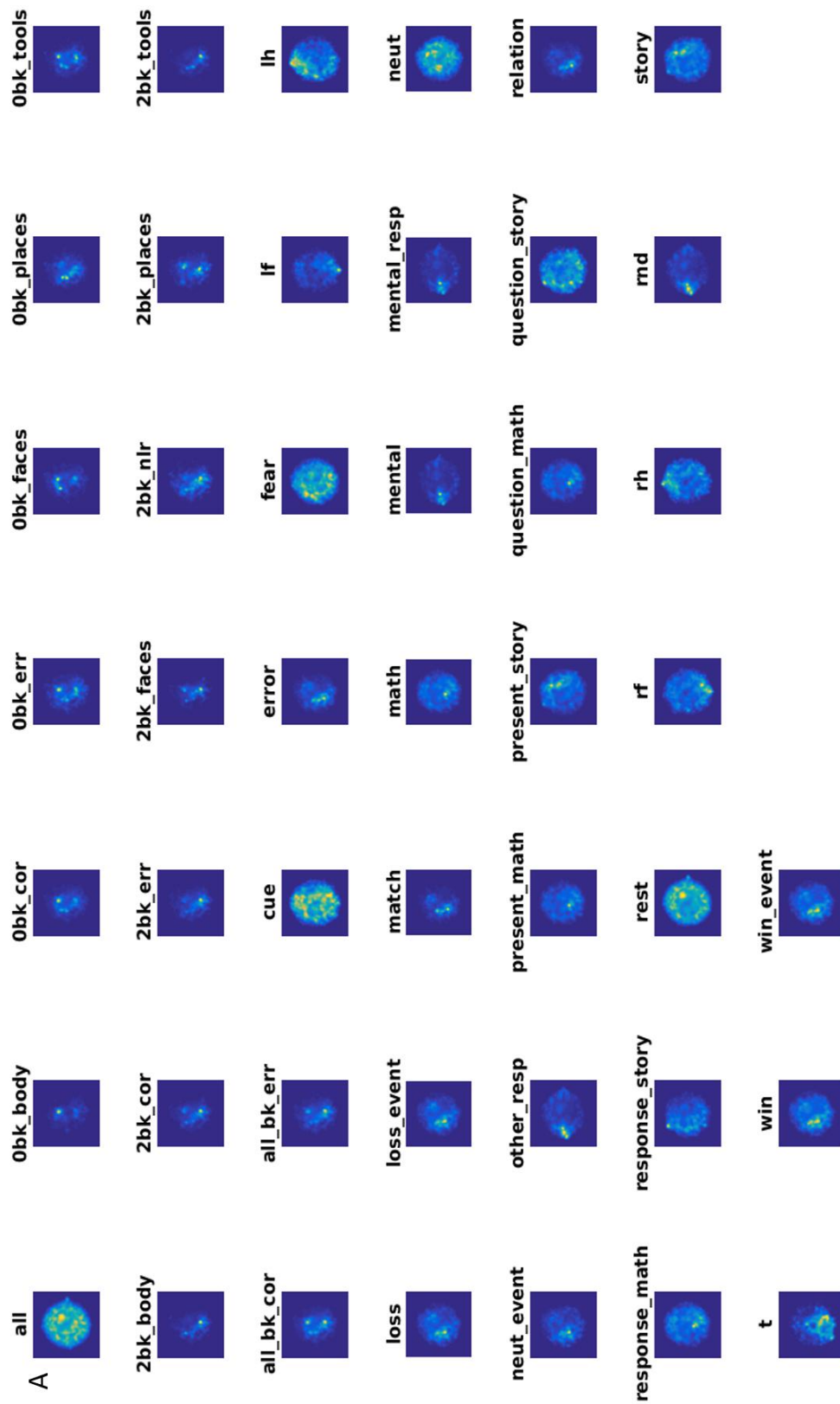


Figure 5.8 displays the descriptive statistics from bootstrap, between-scan, structural similarity index testing as a box-stem plot.



\* Caption appears on next page

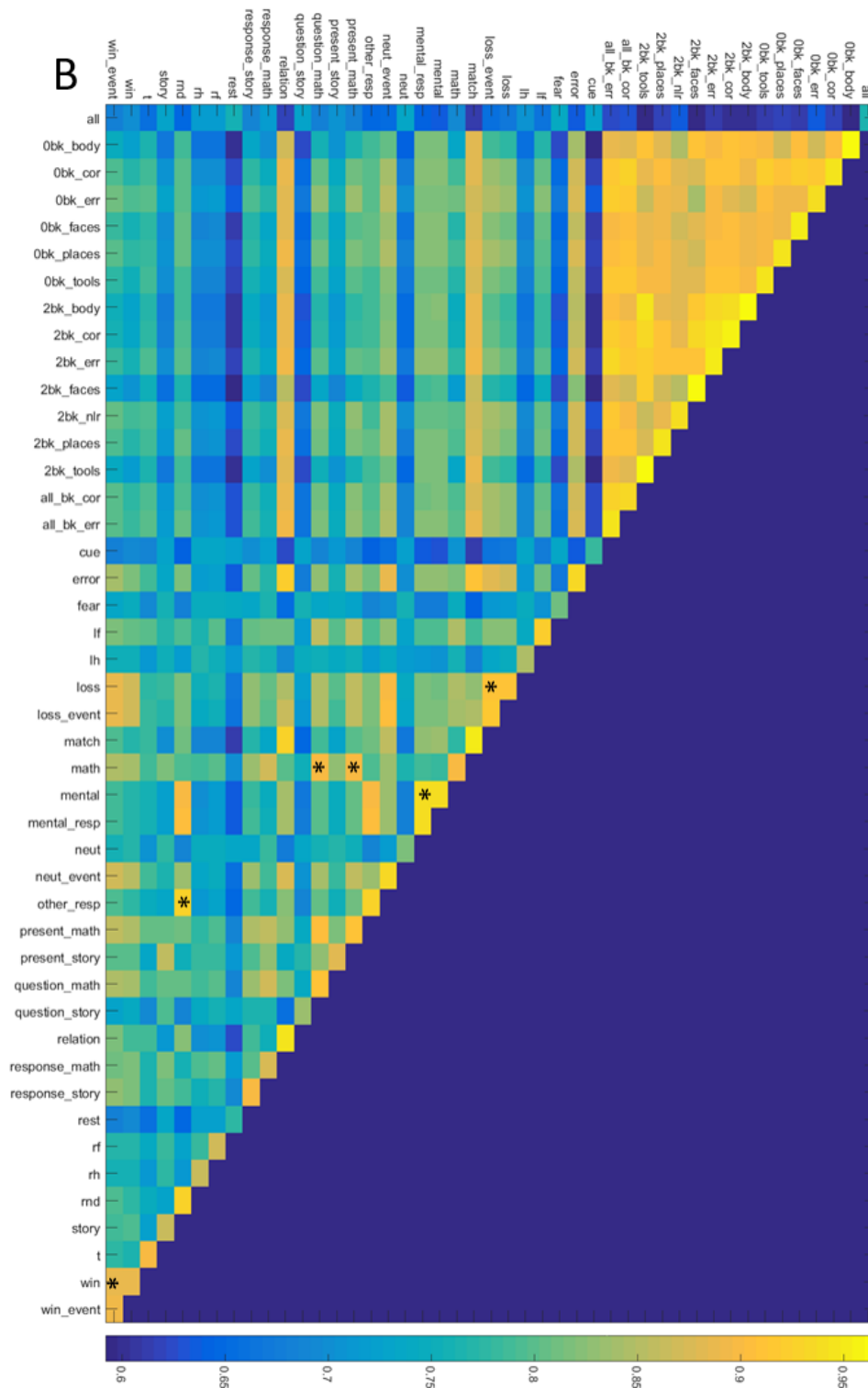


Figure 5.9 displays and compares 2D Euclidean embeddings of instantaneous brain states, segmented by within-scan events. Part A displays the density of each scan's embedded points. Part B displays the mean structural similarity index (SSIM) from 50 bootstrap comparisons, with 2500 points per comparison. Asterisks indicate between-group comparisons whose SSIM was not significantly less than either within-group comparison.

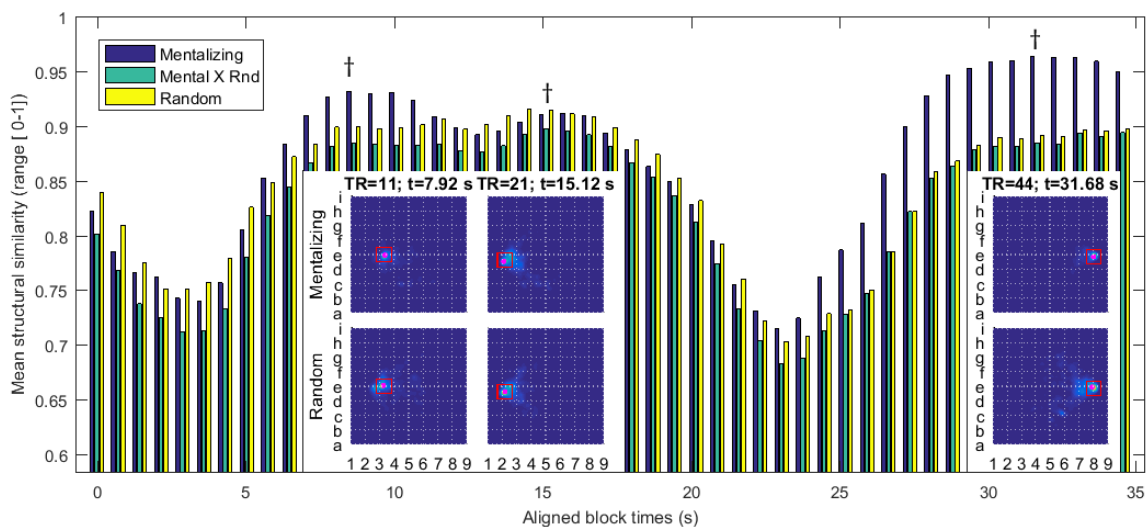


Figure 5.10 analyzes 2D Euclidean embeddings of instantaneous brain states segmented in terms of both block-design task contrasts, and by the acquisition time of temporally aligned task blocks during the SOCIAL scan. The bar chart shows the mean value of the bootstrapped structural similarity index of the within (blue=mentalizing, and yellow=random) and the between (green) block-design-contrast embeddings. For each task contrast, the sample distribution was bootstrapped from 25 realizations of 250 timepoints, randomly sampled from the group-level data set. Fewer bootstrap time points are used to accommodate the reduced sample size in each segmentation. Daggers above the bar chart point to the aligned block times whose embedding density images are displayed in the inset images. Red boxes define the boundary regions given closer scrutiny in figure 5.11.

The block design of HCP task scans—where stimuli are presented in rigidly timed sequences over several blocks—makes it possible to identify significant differences in the point-wise evolution of brain-states during the navigation of contrasting tasks, i.e., fine-scale brain dynamics. While the main text of the present manuscript uses the SOCIAL scan as an example, similar results are found for each set of block-design contrasts. (A movie illustrating the time-locked brain state distributions for all block-design contrasts may be found in the supplemental materials). Figure 5.10 outlines the point-wise state transitions during each SOCIAL task contrast’s 35 s block. A bar chart of the mean SSIM at each time point surveys the focality of the progression of brain states evoked by either stimuli. Comparing the SSIM between stimuli provides a metric of state colocalization. The results demonstrate that, during the first 4 to 5 seconds of the stimulus, brain states in both conditions are incoherent. After  $\sim 7$  s, both conditions achieve focal brain states, with the *mentalizing* condition being much

more compactly delineated. After  $\sim 12$  s, both conditions assume similar brain states. The onset of the fixation block causes brain states to, again, disperse across the embedding. In the latter half of the fixation block, participants who witnessed a *mentalizing* condition tend to linger in a very tightly localized brain state. This suggests that a more characteristic variety of rumination occurs in response to the *mentalizing* stimulus. Density maps from time points having focal brain states are shown in the insets of figure 5.10 and close up in figure 5.11.

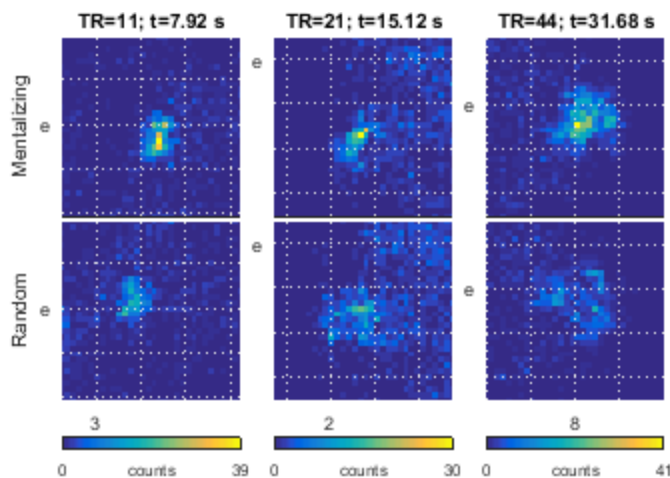


Figure 5.11 details the brain-state differences between task contrasts by displaying close-up views of the boxed areas from figure 5.10. Boxed areas are  $1/8$  the total map space, on a side. Each column is from the same map boundary region. Data are displayed as 2-dimensional histograms from a  $32 \times 32$  grid inside each box. Column colorbars share the same upper limits.

To check the uniqueness of each contrast's associated brain states, figure 5.11 magnifies the most densely populated regions in each contrast's embedding at those time points presented in figure 5.10. After  $\sim 8$  s, volunteers' brains are observed to adopt adjacent and disjoint states. A short time later ( $\sim 15$  s), participants may adopt similar states albeit with the *mentalizing* stimulus inducing brains to adopt a more focal subset of the *random* stimulus' state space. A similar observation obtains during the fixation block ( $\sim 32$  s) with the *mentalizing* stimuli evoking a focal subset relative to the *random* stimuli's state space.

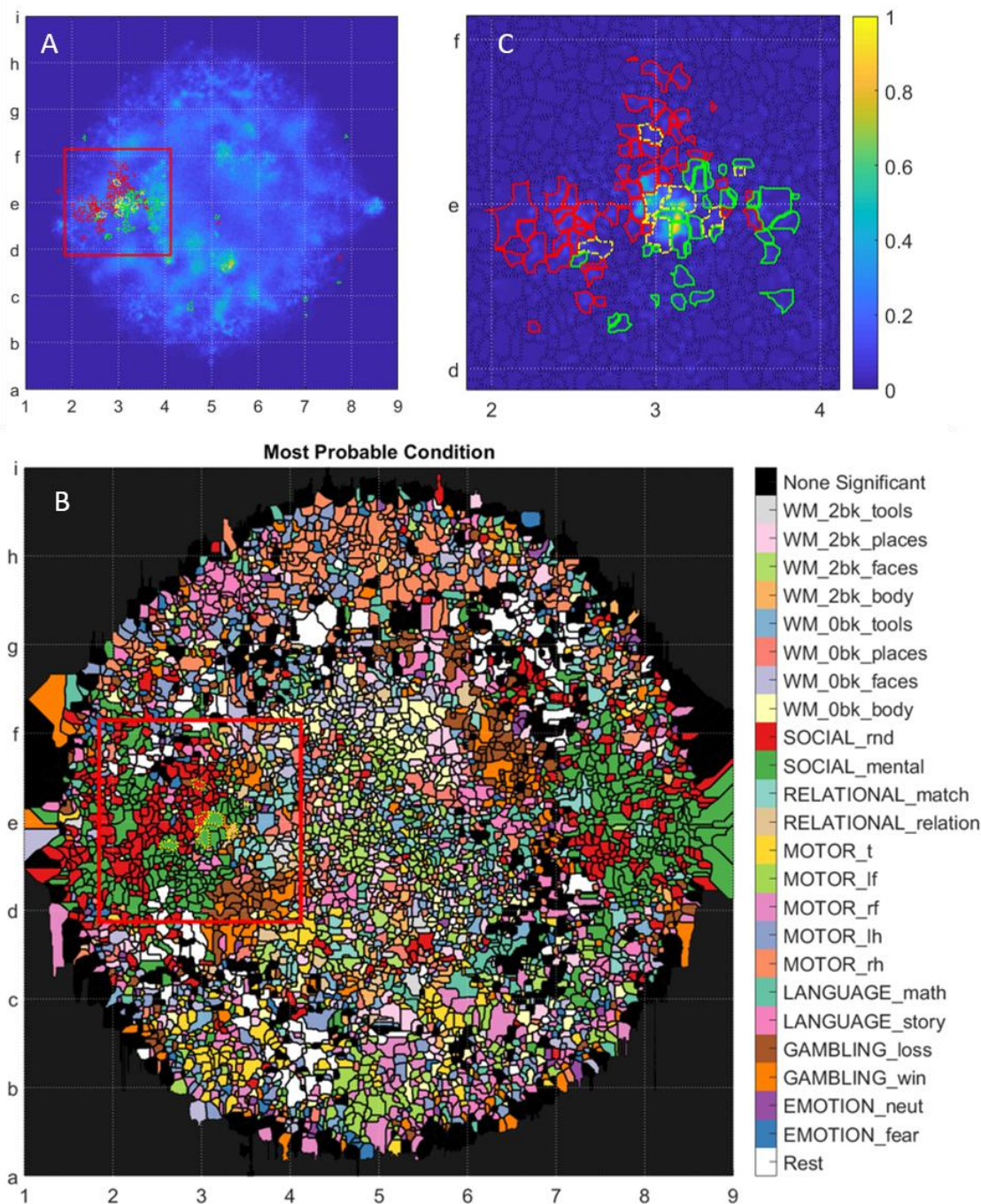


Figure 5.12 displays the statistical affinity of time-resolved and condition-dependent brain-states for a set of watershed map region. Map regions were segmented using a fine-grained density map generated from all studied time points. This granularity was motivated by the focal organization of map points in figure 5.11. Here, the filter width was set to  $1/256^{\text{th}}$  the distance of the furthest map point from the map's center. Part B displays the most probable state associated with each watershed map region. Regions where no significantly associated state was found were marked in black. Part C pursues the hypothesis that volunteers adopt different brain states around the 11<sup>th</sup> image of the SOCIAL task when presented with either the mentalizing (green) or the random (red) stimulus. Map regions significantly populated in response to either stimuli, at this instant, are outlined in yellow, while regions statistically populated by only one stimulus are outlined in their respective colors. Part C's density map is from only SOCIAL scan data. The red boxes in parts A and B outline the range of part C.

The extremely focused distribution of brain states during particular moments of block-design tasks motivated a closer investigation of the statistical distribution of embedded points at particular moments in time. To conduct this analysis, we generated a watershed segmentation of the embedded space after convolving all points on the embedded map with a very narrow Gaussian filter (figure 5.12, part A). We then labeled each embedded point in terms of the experimental condition under which the brain-state was generated, as well as in terms of the time that state was generated relative to the start of each experimental block. Next, we randomly permuted the point labels 100 times to generate a null distribution of the embedded point locations for each condition, at each time point. Finally, we calculated the z-statistic of the probability that the number of embedded points in each watershed region was greater in the real data than in the permuted data. The significance threshold was initially set to a p-value of 5%. With Bonferroni correction for multiple comparisons across  $\sim 5000$  watershed regions and  $\sim 1000$  individual time points, the significance threshold was set to a p-values less than  $1e-8$ . Part B of figure 5.12 color-codes fine-grained watershed regions in terms of the most probable state associated with that region. For simplicity, all time points from a given condition share the same color coding. Part C of the figure addresses the inference from figures 5.10 and 5.11 that the contrasting conditions in the SOCIAL task result in highly stereotypical brain states at especially  $t \cong 8s$  after the start of the block. As inferred from figure 5.11, the *social* stimulus induces highly focal brain states in the map space below and to the right of grid location e3 (green borders). While some brain states generated by the *random* stimulus overlap this region (yellow border), these brain states mostly lie above grid line e or to the left of grid line 3 (red borders).

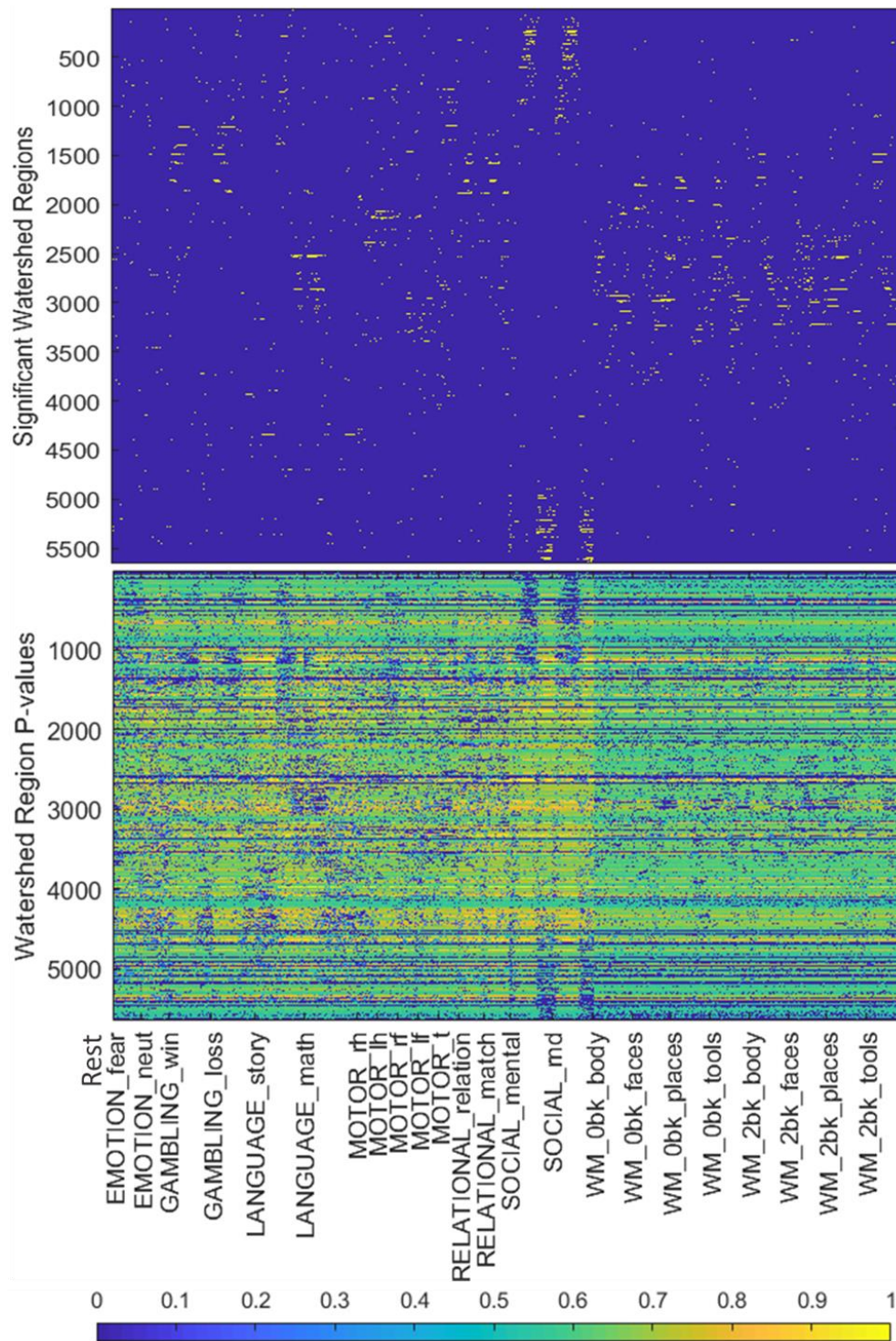


Figure 5.13 addresses the likelihood that each of the experimental condition results in any of the brain states. Conditions are aligned task blocks. The resting state is taken as a single condition. Watershed regions are from a fine-grained density map, and resulted in  $\sim 5000$  regions. A  $\chi$ -statistic was calculated across all possible affinities. The null distribution was generated by randomly permuting the labels associated with each point 100 times. The top plot highlights statistically significant affinities (after Bonferroni correction). The bottom plot displays each comparison's p-value.

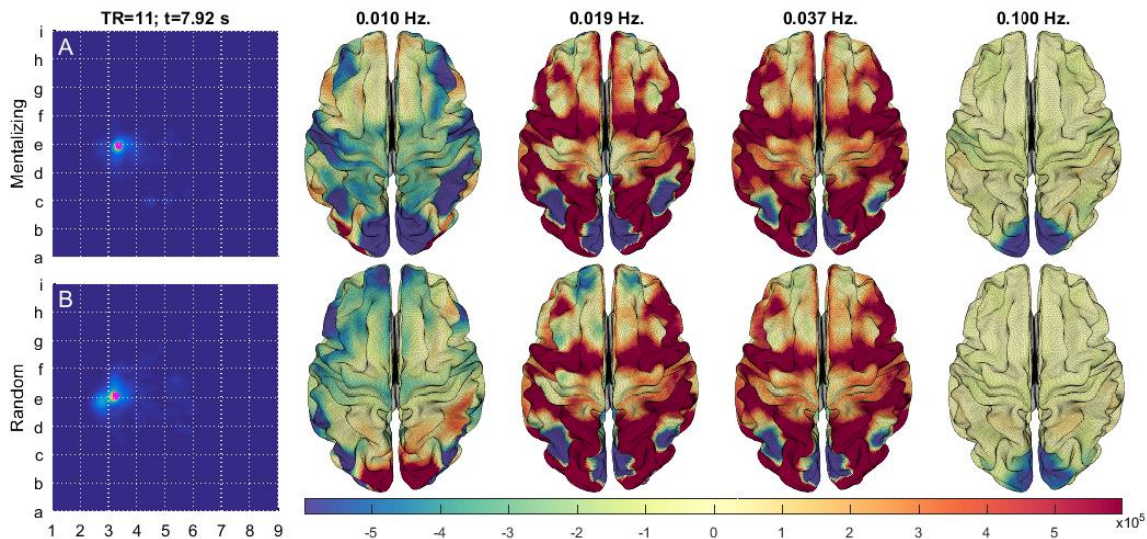


Figure 5.14 displays the difference between the brain states of participants at  $\sim 8$  seconds after being given either a mentalizing (A) or the random (B) visual stimulus during the SOCIAL scan. The brain state is an average from the maximally populated embedding region from within a  $32 \times 32$  grid (magenta points).

We can gain insights into how the brain responds to the contrasting stimuli by projecting a local averaging of the state space (magenta points) onto a model brain surface. Figure 5.14 displays the contrast between the *mentalizing* and *random* stimuli at 7.92 s (TR = 11). Whereas higher frequency ( $\geq 0.037$  Hz) activations are similar, the lower frequency ( $\leq 0.019$  Hz) brain states bear marked differences. At infra-slow frequencies (0.01 Hz) the *mentalizing* stimuli induces in-phase oscillations between the visual, parietal, sensorimotor, and lateral prefrontal cortices. This contrasts with brains experiencing the *random* stimulus for which the visual and left parietal cortex are out-of-phase relative to the anterior prefrontal, left orbitofrontal, and left parietal networks. Slow (0.019 Hz) activations are similar between block contrasts save for, 1) the inclusion of the medial prefrontal cortex within the positive-phase network during the *mentalizing* condition, and 2) stronger negative-phase activation in the anterior prefrontal cortex among volunteers receiving the *random* stimulus. Task-based activation studies of the same task-contrasts identified similar areas of contrasting brain

activity, including the medial prefrontal cortex, lateral parietal cortices, and the visual cortex (Barch et al., 2013; Castelli et al., 2000).

### 5.3. Discussion

The present analytical framework, where BOLD dynamics are interpreted as multiscalar, instantaneous events overcomes many of the challenges faced in the study of brain dynamics. Unlike methods based on sliding window correlation, it avoids the challenges involved in choosing a window length (Hindriks et al., 2016; Shakil et al., 2016). Additionally, whereas previous studies using clustering tended to delineate brain states into a fixed number,  $k$ , of categories (Calhoun et al., 2014), manifold embedding optimizes a low-dimensional representation of the high-dimensional data, allowing a continuous distribution. Nevertheless, it remains possible to identify discrete state categories via subsequent analyses (e.g., through a watershed transformation of the continuous state space).

The statistically significant differences between the state-space distributions of each task provides assurance that the embedded state space effectively differentiates between activation patterns related to different tasks (figures 5.6 and 5.7). On the other hand, the statistically insignificant differences between the state-space distributions of the repeated resting-state scans provide assurance that the embedded state space does not overspecify differences between brain states. The identification of fine-grained differences between the brain states of task contrasts confirms our hypothesis that common stimuli result in short distances between embedding points. Our qualitative and quantitative analysis shows that the random and mentalizing portions of the social task inhabit adjacent but disjoint map regions (figures 5.10 through 5.14).

The segmentation of the embedded space allows the identification of networks whose coactivations (or lack there-of), at particular frequencies and phases, are predominant in any given state (figure 5.2). Our analysis of the SOCIAL scan demonstrates this point when brain regions involved in attention (lateral prefrontal) mental representation (parietal cortex) and

somatic representation (somatomotor cortex) are slowly driven, in-phase, with activations of the visual system.

One of the advantages of the 2D representation obtained from t-SNE is the ease of exploratory data analysis. From the distribution of the data, one can hypothesize about the similarities of different tasks, identify common trajectories, identify states and substates, etc. The resulting hypotheses can be addressed through further statistical analysis as demonstrated for the social task, or they might motivate more specific experiments designed to address the questions in other ways. Regardless of the following analysis, t-SNE provides a powerful tool for characterizing functional neuroimaging data.

*Insight into resting state fMRI.* Given the success of t-SNE at differentiating between tasks, the present study's embedded state space may offer new insights into lingering questions on the character of the resting state (Lowe, 2012). The wide spatial extent, absence of low velocity regions, and overall short dwell times, converge on the finding that the resting-state is not a singular condition. As the only difference between rest and task is the absence of an explicit stimuli, the preference resting brains display for peripheral map regions marks the resting-state as mostly distinct from each of the 7 task states. One notable exception is the interior map region roughly bounded by grid vertices f5, f7, e5 and e7. Details of the region's contribution from each task contrast (figure 5.9) the LANGUAGE scan's *story* condition, the EMOTION scan's *neutral* stimulus, WM *0 back* challenges, and the collection of time points when no stimulus information was explicitly provided (labeled rest). The region may therefore relate to times when volunteers are externally oriented albeit with low cognitive demands. Indeed, volunteer brains often populate this region during the fixation blocks of most tasks (see supplemental videos of especially the GAMBLING and RELATIONAL scans). Another notable exception is the projection of MOTOR and SOCIAL brain states to locations further

out in the map's periphery than the significant REST regions in figure 5.12 part B. Despite the general lack of overlap between the REST and TASK conditions, the REST condition itself exhibits several dense concentrations of time points similar to those observed during the tasks, suggesting that these network configurations constitute common brain states during the resting condition.

*Limitations.* The generation of the embedding's features comes directly from a combination of the input data and the analytical model. As always, the BOLD signal's lack of direct sensitivity to neural activity limits our ability to infer the underlying neurophysiology from the functional imaging data. Noise in the BOLD signal (from residual physiological noise, motion, or the scanner) will affect the embedding of the data.

Regarding the analysis itself, the symmetric distribution of contrasting brain-states across the map may owe itself to the use of signed wavelet coefficients. Like all spectral decompositions, the wavelet transform inherently generates phase information as complex coefficients. The present study projects complex coefficients onto the set of real numbers, thus limiting the analysis to account for two phases, separated by  $180^\circ$ . Other studies have found good segmentation when comparing BOLD signals across additional phases (Chang and Glover, 2010; Yaesoubi et al., 2015). The utility of incorporating phase information supports the notion that regional activations bear some degree of phase-coupling (Thompson GJ, 2014; Tort et al., 2010). Future studies may appropriate this natural feature of brain activity by characterizing the data in alternative metric spaces that better utilize complex-valued data in the high-dimensional space, and better distribute their states into a low-dimensional space.

Furthermore, it should be noted that while using as a wavelet kernel for the spectral transform is expected to result in improved time frequency localization relative to a short-time Fourier transform, it is possible to tune the kernel function to extract additional information

about BOLD dynamics. In addition to requiring that the transform kernel decay smoothly to 0 after a short time, we might also require that the kernel somehow better represent the BOLD signal's underlying impulse waveform. Such kernels may be developed by directly “lifting” the temporal shape from the data itself (Sweldens, 1998). Such a procedure would provide better localization of the BOLD signal's energy into fewer wavelet coefficients, and thus improve the ability to differentiate between states.

*Future directions.* This study demonstrates an analytical technique to observe BOLD dynamics that performs well in segmenting contrasting activities. This approach provides a simple way to summarize patterns of brain state dynamics across various tasks as well as when participants are at rest. The ready capacity to chart brain-state dynamics against experimental stimuli raises the interest for demarcating the functional space of other varieties of conditions. Indeed, study methods are readily amenable to describing brain state dynamics of differing populations and animal models including patient populations. One potential application for the t-SNE embedding is to determine whether it can identify specific states that are present in patients but not in healthy controls. Another area of interest utilizes the preserved timing information to determine common trajectories of brain activity across states during task and rest. The t-SNE embedding facilitates exploratory analysis but can also be used to identify significant differences between tasks or populations using additional analysis. While permutation tests were applied for most of the statistical analyses shown in this manuscript, more sophisticated approaches should also be pursued.

The subsampling procedure reduces the computational complexity of fitting an out of sample point from  $O(n^2)$  operations to  $O(n)$ . This feature enables future research to chart increasingly detailed and comprehensive maps of the brain's dynamical state space from an ever-increasing pool of shared data. One future area of investigation should examine whether

data acquired on different scanners or with different parameters (TR, for example) can be added to the existing embedding or should be handled separately.

## 6. Conclusions and Final Remarks

While whole-brain imaging provides the ability to look into the active human brain, interpreting the meaning of spontaneous fluctuations in 4D BOLD images remains an ongoing challenge. Of course, the capacity to distinguish any system's operation requires raw data to be well curated. Chapter 2, demonstrated that the spatial distribution to the global BOLD signal exhibits localized hot spots that may be due to coil sensitivity or small amounts of motion that increase variance near grey matter/CSF interfaces. Demeaning, detrending, and regression of motion parameters all reduce the relative contribution of these hot spots. Z scoring further reduces the contribution of the hot spots and shows that the entire grey matter contributes strongly to the GS. While widespread, the contributions are not global, being reduced in white matter and subcortical regions. The spatial contribution to the BOLD signal varies substantially across individuals, a finding that may motivate further examination of the previous differences found in patient populations (Hahamy et al., 2014; Yang et al., 2014). No contribution from known repeated large-scale quasi-periodic patterns were observed, but both vascular and neural processes remain potential contributors to the global BOLD signal. Future work with hemodynamic contrasts may help to disentangle these components.

Chapter 3 demonstrated that complex relationships between brain activity at different rates causes spectrally delimited BOLD signaling to behave independently from the processes at other spectra. A system of functional connectivity networks from functional magnetic resonance imaging data in the low frequency oscillation range (0.01 to 0.1 Hz) naturally segments out from other frequency bands. Filtering data to passbands within this range greatly enhances network quality. Further spectral differentiation within the LFO range is warranted by the fact that moderate thresholds of an information theoretic distance metric segment

multispectral BOLD LFOs into distinct FC networks. This fractionation is maintained even as imaging acquisition parameters (such as the sampling TR and voxel size) are changed. Spectral segmentation produces visible alterations in network structure among all groupings of volunteers, and particularly within the brain's default mode network. The appearance of degraded network architectures outside the LFF range of some data sets suggests that BOLD FC is enhanced by fast repetition times ( $\leq 0.645$  s) and by longer scan lengths ( $>10$  min).

Comparative studies in rodents (Chapter 4) confirms that hemodynamic networks are not spandrels, but rather are found in neuroelectric signals. Moreover; this correspondence is dependent on spectral scale, with the most positive correlations corresponding to prominent LFP rhythms, particularly in the delta (1-4 Hz), alpha (8-12 Hz), and gamma (40-60 Hz) bands. These findings confirm that the hemodynamic response is a delayed, and low-pass filtered version of coherent neuroelectric activities.

Multiscale BOLD dynamics are put to use in Chapter 5 to disentangle the complex network changes associated with rest and with multiple task-active states. High-dimensional graphs depicting point-to-point brain state dynamics are made tractable by embedding the graph onto a 2-dimensional sheet. Our analysis of a dynamical brain-state embedding from a large population ( $N=446$ ) concludes that the resting brain actively pursues a range of distinctive states from those adopted during explicit tasks. The realization of both resting and task-active states involves large-scale, and often phase-locked coordination's among multiple brain regions at particular frequencies.

The history of the representation of scaling systems has progressed remarkably in the information age. In the early 80's, fractals as algorithms were just entering human knowledge. Mandelbrot published *The Fractal Geometry of Nature* in 1983; Morlet, Grossman, and others coined the name *wavelets* (French: *Ondelettes*) in a series of publications from 1982 thru 1984

(Daubechies 1992). The advance of modern computing is pushing the threshold of what kinds of multiscale patterns may be uncovered with the advance of deep neuronal networks and other techniques from artificial intelligence (Bengio 2009). The present dissertation is a demonstration that understanding naturally complex multiscale systems, such as the brain, is facilitated by imposing analytical models that account for, and efficiently represent, the system's multiscale properties, and thereby, the codependent structures that emerge at each characteristic scale.

## 7. References

- Abou Elseoud, A., H. Littow, J. Remes, T. Starck, J. Nikkinen, J. Nissilä, O. Tervonen, M. Timonen and V. J. Kiviniemi (2011). "Group-ICA model order highlights patterns of functional brain connectivity." Frontiers in Systems Neuroscience **5**.
- Achard, S., R. Salvador, B. Whitcher, J. Suckling and E. Bullmore (2006). "A Resilient, Low-Frequency, Small-World Human Brain Functional Network with Highly Connected Association Cortical Hubs." The Journal of Neuroscience **26**(1): 63-72.
- Alexander-Bloch, A. F., N. Gogtay, D. Meunier, R. Birn, L. Clasen, F. Lalonde, R. Lenroot, J. Giedd and E. T. Bullmore (2010). "Disrupted modularity and local connectivity of brain functional networks in childhood-onset schizophrenia." Front Syst Neurosci **4**: 147.
- Allen, E. A., E. Damaraju, S. M. Plis, E. B. Erhardt, T. Eichele and V. D. Calhoun (2012). "Tracking Whole-Brain Connectivity Dynamics in the Resting State." Cerebral Cortex.
- Bandettini, P. A. (2012). "Twenty years of functional MRI: The science and the stories." Neuroimage **62**(2): 575-588.
- Bardeen, J. M., B. Carter and S. W. Hawking (1973). "The four laws of black hole mechanics." Communications in Mathematical Physics **31**(2): 161-170.
- Barks, S. K., L. A. Parr and J. K. Rilling (2013). "The Default Mode Network in Chimpanzees (Pan troglodytes) is Similar to That of Humans." Cerebral Cortex.
- Bassett, D. S., B. G. Nelson, B. A. Mueller, J. Camchong and K. O. Lim (2012). "Altered resting state complexity in schizophrenia." Neuroimage **59**(3): 2196-2207.
- Belliveau, J. W., D. N. Kennedy, Jr., R. C. McKinstry, B. R. Buchbinder, R. M. Weisskoff, M. S. Cohen, J. M. Vevea, T. J. Brady and B. R. Rosen (1991). "Functional mapping of the human visual cortex by magnetic resonance imaging." Science **254**(5032): 716-719.
- Bengio, Y. (2009). "Learning Deep Architectures for AI." Found. Trends Mach. Learn. **2**(1): 1-127.
- Benton, M. J. and P. C. Donoghue (2007). "Paleontological evidence to date the tree of life." Mol Biol Evol **24**(1): 26-53.
- Berger, H. (1929). "Über das Elektrenkephalogramm des Menschen." Archiv für Psychiatrie und Nervenkrankheiten **87**(1): 527-570.
- Berman, G. J., D. M. Choi, W. Bialek and J. W. Shaevitz (2014). "Mapping the stereotyped behaviour of freely moving fruit flies." Journal of The Royal Society Interface **11**(99).

- Billings, J. C., A. Medda and S. D. Keilholz (2015). Multiscale FC analysis refines functional connectivity networks in individual brains. 2015 IEEE Global Conference on Signal and Information Processing (GlobalSIP).
- Billings, J. C. W., A. Medda and S. D. Keilholz (2013). Agglomerative clustering for resting state MRI. Neural Engineering (NER), 2013 6th International IEEE/EMBS Conference on.
- Birn, R. M., E. K. Molloy, R. Patriat, T. Parker, T. B. Meier, G. R. Kirk, V. A. Nair, M. E. Meyerand and V. Prabhakaran (2013). "The effect of scan length on the reliability of resting-state fMRI connectivity estimates." Neuroimage **83**: 550-558.
- Biswal, B., E. A. Deyoe and J. S. Hyde (1996). "Reduction of physiological fluctuations in fMRI using digital filters." Magnetic Resonance in Medicine **35**(1): 107-113.
- Biswal, B., F. Z. Yetkin, V. M. Haughton and J. S. Hyde (1995). "Functional connectivity in the motor cortex of resting human brain using echo-planar MRI." Magn Reson Med **34**(4): 537-541.
- Buckner, Randy L. Krienen Fenna M. Castellanos Angela Diaz Julio C. Yeo B. T. Thomas (2011). "The organization of the human cerebellum estimated by intrinsic functional connectivity." Journal of Neurophysiology **106**(5): 2322-2345.
- Bullmore, E., J. Fadili, V. Maxim, L. Sendur, B. Whitcher, J. Suckling, M. Brammer and M. Breakspear (2004). "Wavelets and functional magnetic resonance imaging of the human brain." Neuroimage **23 Suppl 1**: S234-249.
- Bullmore, E. and O. Sporns (2009). "Complex brain networks: graph theoretical analysis of structural and functional systems." Nat Rev Neurosci **10**(3): 186-198.
- Bullock, T. H. (1948). "PROPERTIES OF A SINGLE SYNAPSE IN THE STELLATE GANGLION OF SQUID." Journal of Neurophysiology **11**(4): 343-364.
- Butler, A. B. (2000). "Chordate evolution and the origin of craniates: an old brain in a new head." Anat Rec **261**(3): 111-125.
- Buzsaki, G. (2009). Rhythms of the Brain, Oxford University Press.
- Buzsáki, G., C. A. Anastassiou and C. Koch (2012). "The origin of extracellular fields and currents — EEG, ECoG, LFP and spikes." Nat Rev Neurosci **13**(6): 407-420.
- Buzsáki, G. and A. Draguhn (2004). "Neuronal Oscillations in Cortical Networks." Science **304**(5679): 1926-1929.
- Calhoun, V. D., T. Adali, G. D. Pearlson and J. J. Pekar (2001). "A method for making group inferences from functional MRI data using independent component analysis." Hum Brain Mapp **14**(3): 140-151.

- Calhoun, Vince D., R. Miller, G. Pearlson and T. Adalı (2014). "The Chronnectome: Time-Varying Connectivity Networks as the Next Frontier in fMRI Data Discovery." Neuron **84**(2): 262-274.
- Chang, C. and G. H. Glover (2010). "Time-frequency dynamics of resting-state brain connectivity measured with fMRI." Neuroimage **50**(1): 81-98.
- Cheng, H., H. Yan, L. J. Bai and B. G. Wang (2013). "Exploration of whole brain networks modulated by acupuncture at analgesia acupoint ST36 using scale-specific wavelet correlation analysis." Chin Med J (Engl) **126**(13): 2459-2464.
- Ciuciu, P., G. Varoquaux, P. Abry, S. Sadaghiani and A. Kleinschmidt (2012). "Scale-Free and Multifractal Time Dynamics of fMRI Signals during Rest and Task." Front Physiol **3**: 186.
- Coifman, R. R., Y. Meyer and V. Wickerhauser (1992). Wavelet analysis and signal processing. In Wavelets and their Applications, Citeseer.
- Coifman, R. R. and M. V. Wickerhauser (1992). "Entropy-based algorithms for best basis selection." Information Theory, IEEE Transactions on **38**(2): 713-718.
- Cordes, D., V. Haughton, J. D. Carew, K. Arfanakis and K. Maravilla (2002). "Hierarchical clustering to measure connectivity in fMRI resting-state data." Magnetic resonance imaging **20**(4): 305-317.
- Daubechies, I. (1988). "Orthonormal bases of compactly supported wavelets." Communications on pure and applied mathematics **41**(7): 909-996.
- Daubechies, I. (1992). Ten lectures on wavelets. Philadelphia, PA, Society for Industrial and Applied Mathematics.
- Deco, G., V. K. Jirsa and A. R. McIntosh (2011). "Emerging concepts for the dynamical organization of resting-state activity in the brain." Nat Rev Neurosci **12**(1): 43-56.
- Du, C., N. D. Volkow, A. P. Koretsky and Y. Pan (2014). "Low-frequency calcium oscillations accompany deoxyhemoglobin oscillations in rat somatosensory cortex." Proc Natl Acad Sci U S A **111**(43): E4677-4686.
- Einevoll, G. T., C. Kayser, N. K. Logothetis and S. Panzeri (2013). "Modelling and analysis of local field potentials for studying the function of cortical circuits." Nat Rev Neurosci **14**(11): 770-785.
- Eklund, A., T. E. Nichols and H. Knutsson (2016). "Cluster failure: Why fMRI inferences for spatial extent have inflated false-positive rates." Proceedings of the National Academy of Sciences **113**(28): 7900-7905.
- Feinberg, D. A., S. Moeller, S. M. Smith, E. Auerbach, S. Ramanna, M. F. Glasser, K. L. Miller, K. Ugurbil and E. Yacoub (2010). "Multiplexed Echo Planar Imaging for Sub-Second Whole Brain FMRI and Fast Diffusion Imaging." PLoS ONE **5**(12): e15710.

Fox, M. D., A. Z. Snyder, J. L. Vincent, M. Corbetta, D. C. Van Essen and M. E. Raichle (2005). "The human brain is intrinsically organized into dynamic, anticorrelated functional networks." Proceedings of the National Academy of Sciences of the United States of America **102**(27): 9673-9678.

Fox, M. D., D. Zhang, A. Z. Snyder and M. E. Raichle (2009). "The Global Signal and Observed Anticorrelated Resting State Brain Networks." Journal of Neurophysiology **101**(6): 3270.

Friston, K. J., J. T. Ashburner, S. J. Kiebel, T. E. Nichols and W. D. Penny (2011). Statistical Parametric Mapping: The Analysis of Functional Brain Images: The Analysis of Functional Brain Images, Academic Press.

Garcia-Fernandez, J. (2005). "The genesis and evolution of homeobox gene clusters." Nat Rev Genet **6**(12): 881-892.

Glomb, K., A. Ponce-Alvarez, M. Gilson, P. Ritter and G. Deco (2017). "Stereotypical Modulations In Dynamic Functional Connectivity Explained By Changes In BOLD Variance." bioRxiv.

Gonzalez-Castillo, J., C. W. Hoy, D. A. Handwerker, M. E. Robinson, L. C. Buchanan, Z. S. Saad and P. A. Bandettini (2015). "Tracking ongoing cognition in individuals using brief, whole-brain functional connectivity patterns." Proceedings of the National Academy of Sciences **112**(28): 8762-8767.

Greene, B. (2004). The fabric of the cosmos: Space, time, and the texture of reality, Vintage.

Greicius, M. D., V. Kiviniemi, O. Tervonen, V. Vainionpää, S. Alahuhta, A. L. Reiss and V. Menon (2008). "Persistent default-mode network connectivity during light sedation." Human Brain Mapping **29**(7): 839-847.

Greve, D. N., G. G. Brown, B. A. Mueller, G. Glover and T. T. Liu (2013). "A survey of the sources of noise in fMRI." Psychometrika **78**(3): 396-416.

Gu, S., F. Pasqualetti, M. Cieslak, Q. K. Telesford, A. B. Yu, A. E. Kahn, J. D. Medaglia, J. M. Vettel, M. B. Miller, S. T. Grafton and D. S. Bassett (2015). "Controllability of structural brain networks." Nat Commun **6**.

Hasenkamp, W., C. D. Wilson-Mendenhall, E. Duncan and L. W. Barsalou (2012). "Mind wandering and attention during focused meditation: a fine-grained temporal analysis of fluctuating cognitive states." NeuroImage **59**(1): 750-760.

He, B. J. (2011). "Scale-free properties of the functional magnetic resonance imaging signal during rest and task." J Neurosci **31**(39): 13786-13795.

He, B. J. (2014). "Scale-free brain activity: past, present, and future." Trends Cogn Sci **18**(9): 480-487.

Henry, E. R., R. B. Best and W. A. Eaton (2013). "Comparing a simple theoretical model for protein folding with all-atom molecular dynamics simulations." Proceedings of the National Academy of Sciences **110**(44): 17880-17885.

Hidalgo, C. (2015). Why information grows: The evolution of order, from atoms to economies, Basic Books.

Hsu, J. (2014). "Ibm's new brain [news]." IEEE Spectrum **51**(10): 17-19.

Human Connectome Project (2014). HCP beta-release of group-ICAmaps, nodetimeseries and network matrices. <http://humanconnectome.org>.

Hutchison, R. M., T. Womelsdorf, E. A. Allen, P. A. Bandettini, V. D. Calhoun, M. Corbetta, S. Della Penna, J. H. Duyn, G. H. Glover, J. Gonzalez-Castillo, D. A. Handwerker, S. Keilholz, V. Kiviniemi, D. A. Leopold, F. de Pasquale, O. Sporns, M. Walter and C. Chang (2013). "Dynamic functional connectivity: promise, issues, and interpretations." Neuroimage **80**: 360-378.

Jarvis, E. D., O. Gunturkun, L. Bruce, A. Csillag, H. Karten, W. Kuenzel, L. Medina, G. Paxinos, D. J. Perkel, T. Shimizu, G. Striedter, J. M. Wild, G. F. Ball, J. Dugas-Ford, S. E. Durand, G. E. Hough, S. Husband, L. Kubikova, D. W. Lee, C. V. Mello, A. Powers, C. Siang, T. V. Smulders, K. Wada, S. A. White, K. Yamamoto, J. Yu, A. Reiner and A. B. Butler (2005). "Avian brains and a new understanding of vertebrate brain evolution." Nat Rev Neurosci **6**(2): 151-159.

Johnson, M. (2012). "Laboratory mice and rats." Mater. Methods **2**: 113.

Kalcher, K., R. N. Boubela, W. Huf, L. Bartova, C. Kronnerwetter, B. Derntl, L. Pezawas, P. Filzmoser, C. Nasel and E. Moser (2014). "The Spectral Diversity of Resting-State Fluctuations in the Human Brain." PLoS ONE **9**(4): e93375.

Keilholz, S. D., M. E. Magnuson, W. J. Pan, M. Willis and G. J. Thompson (2013). "Dynamic properties of functional connectivity in the rodent." Brain Connect **3**(1): 31-40.

Kiviniemi, V., T. Starck, J. Remes, X. Long, J. Nikkinen, M. Haapea, J. Veijola, I. Moilanen, M. Isohanni, Y. F. Zang and O. Tervonen (2009). "Functional segmentation of the brain cortex using high model order group PICA." Hum Brain Mapp **30**(12): 3865-3886.

Krubitzer, L. (1995). "The organization of neocortex in mammals: are species differences really so different?" Trends Neurosci **18**(9): 408-417.

Lam, S. C., Z. Wang, Y. Li, T. Franklin, C. O'Brien, J. Magland and A. R. Childress (2013). "Wavelet-transformed temporal cerebral blood flow signals during attempted inhibition of cue-induced cocaine craving distinguish prognostic phenotypes." Drug Alcohol Depend **128**(1-2): 140-147.

Lee, H.-L., B. Zahneisen, T. Hugger, P. LeVan and J. Hennig (2013). "Tracking dynamic resting-state networks at higher frequencies using MR-encephalography." NeuroImage **65**(0): 216-222.

- Li, J. M., W. J. Bentley, A. Z. Snyder, M. E. Raichle and L. H. Snyder (2015). "Functional connectivity arises from a slow rhythmic mechanism." Proceedings of the National Academy of Sciences **112**(19): E2527-E2535.
- Lisman, John E. and O. Jensen (2013). "The Theta-Gamma Neural Code." Neuron **77**(6): 1002-1016.
- Liu, X., B. D. Ward, J. R. Binder, S.-J. Li and A. G. Hudetz (2014). "Scale-Free Functional Connectivity of the Brain Is Maintained in Anesthetized Healthy Participants but Not in Patients with Unresponsive Wakefulness Syndrome." PLoS ONE **9**(3): e92182.
- Logothetis, N. K. (2008). "What we can do and what we cannot do with fMRI." Nature **453**(7197): 869-878.
- Logothetis, N. K., J. Pauls, M. Augath, T. Trinath and A. Oeltermann (2001). "Neurophysiological investigation of the basis of the fMRI signal." Nature **412**(6843): 150-157.
- Lowe, M. J. (2012). "The emergence of doing "nothing" as a viable paradigm design." Neuroimage **62**(2): 1146-1151.
- Lu, H., Q. Zou, H. Gu, M. E. Raichle, E. A. Stein and Y. Yang (2012). "Rat brains also have a default mode network." Proceedings of the National Academy of Sciences **109**(10): 3979-3984.
- Lu, H., Y. Zuo, H. Gu, J. A. Waltz, W. Zhan, C. A. Scholl, W. Rea, Y. Yang and E. A. Stein (2007). "Synchronized delta oscillations correlate with the resting-state functional MRI signal." Proc Natl Acad Sci U S A **104**(46): 18265-18269.
- Magnuson, M. E., G. J. Thompson, W. J. Pan and S. D. Keilholz (2014). "Effects of Severing the Corpus Callosum on Electrical and BOLD Functional Connectivity and Spontaneous Dynamic Activity in the Rat Brain." Brain Connect **4**(1): 15-29.
- Magnuson, M. E., G. J. Thompson, W. J. Pan and S. D. Keilholz (2014). "Time-dependent effects of isoflurane and dexmedetomidine on functional connectivity, spectral characteristics, and spatial distribution of spontaneous BOLD fluctuations." NMR Biomed **27**(3): 291-303.
- Majeed, W. and M. J. Avison (2014). "Robust Data Driven Model Order Estimation for Independent Component Analysis of fMRI Data with Low Contrast to Noise." PLoS ONE **9**(4): e94943.
- Mallat, S. (1999). A wavelet tour of signal processing, Access Online via Elsevier.
- Mallat, S. G. (1989). "A theory for multiresolution signal decomposition: the wavelet representation." Pattern Analysis and Machine Intelligence, IEEE Transactions on **11**(7): 674-693.
- Mandelbrot, B. B. (1983). The fractal geometry of nature, Macmillan.

Mantini, D., M. G. Perrucci, C. Del Gratta, G. L. Romani and M. Corbetta (2007). "Electrophysiological signatures of resting state networks in the human brain." Proceedings of the National Academy of Sciences **104**(32): 13170-13175.

McKeown, M. J., S. Makeig, G. G. Brown, T.-P. Jung, S. S. Kindermann, A. J. Bell and T. J. Sejnowski (1997). Analysis of fMRI data by blind separation into independent spatial components, DTIC Document.

Medda, A., J. C. Billings and S. D. Keilholz (2014). Multiscale functional networks in human resting state functional MRI. Signals, Systems and Computers, 2014 48th Asilomar Conference on.

Meilă, M. (2007). "Comparing clusterings—an information based distance." Journal of Multivariate Analysis **98**(5): 873-895.

Meng, C., F. Brandl, M. Tahmasian, J. Shao, A. Manoliu, M. Scherr, D. Schwerthoffer, J. Bauml, H. Forstl, C. Zimmer, A. M. Wohlschlagel, V. Riedl and C. Sorg (2013). "Aberrant topology of striatum's connectivity is associated with the number of episodes in depression." Brain.

Meyer, F. (1994). "Topographic distance and watershed lines." Signal Processing **38**(1): 113-125.

Meyer, Y. (1993). "Wavelets-algorithms and applications." Wavelets-Algorithms and applications Society for Industrial and Applied Mathematics Translation., 142 p. **1**.

Milham, M. P. (2013). "1000 Functional Connectomes Project." 2013.

Misiti, M., Y. Misiti, G. Oppenheim and J.-M. Poggi (2013). Wavelet toolbox user's guide. The Math Works Inc. Online.

Mitra, P. and H. Bokil (2008). Observed brain dynamics. Oxford ; New York, Oxford University Press.

Mnih, V., K. Kavukcuoglu, D. Silver, A. A. Rusu, J. Veness, M. G. Bellemare, A. Graves, M. Riedmiller, A. K. Fidjeland, G. Ostrovski, S. Petersen, C. Beattie, A. Sadik, I. Antonoglou, H. King, D. Kumaran, D. Wierstra, S. Legg and D. Hassabis (2015). "Human-level control through deep reinforcement learning." Nature **518**(7540): 529-533.

Moeller, S., E. Yacoub, C. A. Olman, E. Auerbach, J. Strupp, N. Harel and K. Uğurbil (2010). "Multiband multislice GE-EPI at 7 tesla, with 16-fold acceleration using partial parallel imaging with application to high spatial and temporal whole-brain fMRI." Magnetic Resonance in Medicine **63**(5): 1144-1153.

Murphy, K., R. M. Birn and P. A. Bandettini (2013). "Resting-state fMRI confounds and cleanup." Neuroimage **80**: 349-359.

Nallasamy, N. and D. Y. Tsao (2011). "Functional Connectivity in the Brain: Effects of Anesthesia." The Neuroscientist **17**(1): 94-106.

Nathan Kline Institute for Psychiatric Research (2013). Enhanced Rockland Sample Multiband Imaging Test-Retest Pilot Dataset. Online: [http://fcon\\_1000.projects.nitrc.org/indi/pro/eNKI\\_RS\\_TRT/FrontPage.html](http://fcon_1000.projects.nitrc.org/indi/pro/eNKI_RS_TRT/FrontPage.html), 1000 Functional Connectomes Project.

Nicolis, G. and I. Prigogine (1977). Self-organization in nonequilibrium systems, Wiley, New York.

Nomura, T., H. Gotoh and K. Ono (2013). "Changes in the regulation of cortical neurogenesis contribute to encephalization during amniote brain evolution." Nat Commun **4**: 2206.

Nooner, K. B., S. J. Colcombe, R. H. Tobe, M. Mennes, M. M. Benedict, A. L. Moreno, L. J. Panek, S. Brown, S. T. Zavitz, Q. Li, S. Sikka, D. Gutman, S. Bangaru, R. T. Schlachter, S. M. Kamiel, A. R. Anwar, C. M. Hinz, M. S. Kaplan, A. B. Rachlin, S. Adelsberg, B. Cheung, R. Khanuja, C. Yan, C. C. Craddock, V. Calhoun, W. Courtney, M. King, D. Wood, C. L. Cox, A. M. Kelly, A. Di Martino, E. Petkova, P. T. Reiss, N. Duan, D. Thomsen, B. Biswal, B. Coffey, M. J. Hoptman, D. C. Javitt, N. Pomara, J. J. Sidtis, H. S. Koplewicz, F. X. Castellanos, B. L. Leventhal and M. P. Milham (2012). "The NKI-Rockland Sample: A Model for Accelerating the Pace of Discovery Science in Psychiatry." Front Neurosci **6**: 152.

O'Leary, M. A., J. I. Bloch, J. J. Flynn, T. J. Gaudin, A. Giallombardo, N. P. Giannini, S. L. Goldberg, B. P. Kraatz, Z.-X. Luo, J. Meng, X. Ni, M. J. Novacek, F. A. Perini, Z. S. Randall, G. W. Rougier, E. J. Sargis, M. T. Silcox, N. B. Simmons, M. Spaulding, P. M. Velazco, M. Weksler, J. R. Wible and A. L. Cirranello (2013). "The Placental Mammal Ancestor and the Post-K-Pg Radiation of Placentals." Science **339**(6120): 662-667.

Ogawa, S., T. M. Lee, A. R. Kay and D. W. Tank (1990). "Brain magnetic resonance imaging with contrast dependent on blood oxygenation." Proceedings of the National Academy of Sciences **87**(24): 9868-9872.

Pan, W. J., G. Thompson, M. Magnuson, W. Majeed, D. Jaeger and S. Keilholz (2011). "Broadband local field potentials correlate with spontaneous fluctuations in functional magnetic resonance imaging signals in the rat somatosensory cortex under isoflurane anesthesia." Brain Connect **1**(2): 119-131.

Pan, W. J., G. J. Thompson, M. E. Magnuson, D. Jaeger and S. Keilholz (2013). "Infraslow LFP correlates to resting-state fMRI BOLD signals." Neuroimage **74**: 288-297.

Pani, A. M., E. E. Mullarkey, J. Aronowicz, S. Assimacopoulos, E. A. Grove and C. J. Lowe (2012). "Ancient deuterostome origins of vertebrate brain signalling centres." Nature **483**(7389): 289-294.

Papo, D., J. M. Buldú, S. Boccaletti and E. T. Bullmore (2014). "Complex network theory and the brain." Philosophical Transactions of the Royal Society B: Biological Sciences **369**(1653): 20130520.

Peltier, S. J., C. Kerssens, S. B. Hamann, P. S. Sebel, M. Byas-Smith and X. Hu (2005). "Functional connectivity changes with concentration of sevoflurane anesthesia." Neuroreport **16**(3): 285-288.

- Plis, S. M., D. Hjelm, R. Salakhutdinov, E. A. Allen, H. J. Bockholt, J. D. Long, H. J. Johnson, J. Paulsen, J. A. Turner and V. D. Calhoun (2014). "Deep learning for neuroimaging: a validation study." Frontiers in Neuroscience **8**.
- Power, J. D., M. Plitt, T. O. Laumann and A. Martin (2017). "Sources and implications of whole-brain fMRI signals in humans." NeuroImage **146**: 609-625.
- Raichle, M. E., A. M. MacLeod, A. Z. Snyder, W. J. Powers, D. A. Gusnard and G. L. Shulman (2001). "A default mode of brain function." Proceedings of the National Academy of Sciences **98**(2): 676-682.
- Raichle, M. E. and M. A. Mintun (2006). "Brain work and brain imaging." Annu Rev Neurosci **29**: 449-476.
- Rosen, B. R. and R. L. Savoy (2012). "fMRI at 20: Has it changed the world?" Neuroimage **62**(2): 1316-1324.
- Rubinov, M. and E. Bullmore (2013). "Fledgling pathoconnectomics of psychiatric disorders." Trends in Cognitive Sciences **17**(12): 641-647.
- Salomon, R. M., R. L. Cowan, B. P. Rogers, M. S. Dietrich, A. L. Bauernfeind, R. M. Kessler and J. C. Gore (2011). "Time series fMRI measures detect changes in pontine raphe following acute tryptophan depletion." Psychiatry Res **191**(2): 112-121.
- Salomon, R. M., J. Karageorgiou, M. S. Dietrich, J. Y. McLellan, E. J. Charboneau, J. U. Blackford and R. L. Cowan (2012). "MDMA (Ecstasy) association with impaired fMRI BOLD thalamic coherence and functional connectivity." Drug Alcohol Depend **120**(1-3): 41-47.
- Salvador, R., J. Suckling, C. Schwarzbauer and E. Bullmore (2005). "Undirected graphs of frequency-dependent functional connectivity in whole brain networks." Philosophical Transactions of the Royal Society B: Biological Sciences **360**(1457): 937-946.
- Samuels, E. R. and E. Szabadi (2008). "Functional Neuroanatomy of the Noradrenergic Locus Coeruleus: Its Roles in the Regulation of Arousal and Autonomic Function Part I: Principles of Functional Organisation." Current Neuropharmacology **6**(3): 235-253.
- Schwarz, A. J., N. Gass, A. Sartorius, L. Zheng, M. Spedding, E. Schenker, C. Risterucci, A. Meyer-Lindenberg and W. Weber-Fahr (2013). "The low-frequency blood oxygenation level-dependent functional connectivity signature of the hippocampal–prefrontal network in the rat brain." Neuroscience **228**(0): 243-258.
- Shakil, S., C. H. Lee and S. D. Keilholz (2016). "Evaluation of sliding window correlation performance for characterizing dynamic functional connectivity and brain states." Neuroimage **133**: 111-128.
- Shannon, C. E. (2001). "A mathematical theory of communication." ACM SIGMOBILE Mobile Computing and Communications Review **5**(1): 3-55.

- Skidmore, F., D. Korenkevych, Y. Liu, G. He, E. Bullmore and P. M. Pardalos (2011). "Connectivity brain networks based on wavelet correlation analysis in Parkinson fMRI data." Neurosci Lett **499**(1): 47-51.
- Smith, S. M., P. T. Fox, K. L. Miller, D. C. Glahn, P. M. Fox, C. E. Mackay, N. Filippini, K. E. Watkins, R. Toro, A. R. Laird and C. F. Beckmann (2009). "Correspondence of the brain's functional architecture during activation and rest." Proceedings of the National Academy of Sciences.
- Smith, S. M., K. L. Miller, S. Moeller, J. Xu, E. J. Auerbach, M. W. Woolrich, C. F. Beckmann, M. Jenkinson, J. Andersson, M. F. Glasser, D. C. Van Essen, D. A. Feinberg, E. S. Yacoub and K. Ugurbil (2012). "Temporally-independent functional modes of spontaneous brain activity." Proceedings of the National Academy of Sciences **109**(8): 3131-3136.
- Spreng, R. N., J. Sepulcre, G. R. Turner, W. D. Stevens and D. L. Schacter (2012). "Intrinsic Architecture Underlying the Relations among the Default, Dorsal Attention, and Frontoparietal Control Networks of the Human Brain." Journal of Cognitive Neuroscience **25**(1): 74-86.
- Stanberry, L., R. Nandy and D. Cordes (2003). "Cluster analysis of fMRI data using dendrogram sharpening." Human Brain Mapping **20**(4): 201-219.
- Supekar, K., V. Menon, D. Rubin, M. Musen and M. D. Greicius (2008). "Network analysis of intrinsic functional brain connectivity in Alzheimer's disease." PLoS Comput Biol **4**(6): e1000100.
- Thomas Yeo, B. T., F. M. Krienen, J. Sepulcre, M. R. Sabuncu, D. Lashkari, M. Hollinshead, J. L. Roffman, J. W. Smoller, L. Zöllei, J. R. Polimeni, B. Fischl, H. Liu and R. L. Buckner (2011). The organization of the human cerebral cortex estimated by intrinsic functional connectivity.
- Thompson, G. J., M. D. Merritt, W. J. Pan, M. E. Magnuson, J. K. Grooms, D. Jaeger and S. D. Keilholz (2013). "Neural correlates of time-varying functional connectivity in the rat." Neuroimage **83**: 826-836.
- Thompson GJ, P. W., Billings JC, Grooms JK, Shakil S, Jaeger D and Keilholz SD (2014). "Phase-amplitude coupling and infraslow (<1Hz) frequencies in the rat brain: relationship to resting state fMRI." Front. Integr. Neurosci **8**(14).
- Tian, J. and R. O. Wells Jr (1996). A remark on vanishing moments. Signals, Systems and Computers, 1996. Conference Record of the Thirtieth Asilomar Conference on, IEEE.
- Tort, A. B. L., R. Komorowski, H. Eichenbaum and N. Kopell (2010). "Measuring Phase-Amplitude Coupling Between Neuronal Oscillations of Different Frequencies." Journal of Neurophysiology **104**(2): 1195-1210.
- Upadhyay, J., S. J. Baker, P. Chandran, L. Miller, Y. Lee, G. J. Marek, U. Sakoglu, C.-L. Chin, F. Luo, G. B. Fox and M. Day (2011). "Default-Mode-Like Network Activation in Awake Rodents." PLoS ONE **6**(11): e27839.

- Van Bellegem, S. and R. von Sachs (2008). "Locally adaptive estimation of evolutionary wavelet spectra." 1879-1924.
- van der Maaten, L. and G. Hinton (2008). "Visualizing data using t-SNE." Journal of Machine Learning Research **9**(2579-2605): 85.
- van der Maaten, L., E. Postma and J. Van den Herik (2009). "Dimensionality reduction: a comparative." J Mach Learn Res **10**: 66-71.
- Van Essen, D. C., K. Ugurbil, E. Auerbach, D. Barch, T. E. Behrens, R. Bucholz, A. Chang, L. Chen, M. Corbetta, S. W. Curtiss, S. Della Penna, D. Feinberg, M. F. Glasser, N. Harel, A. C. Heath, L. Larson-Prior, D. Marcus, G. Michalareas, S. Moeller, R. Oostenveld, S. E. Petersen, F. Prior, B. L. Schlaggar, S. M. Smith, A. Z. Snyder, J. Xu and E. Yacoub (2012). "The Human Connectome Project: a data acquisition perspective." Neuroimage **62**(4): 2222-2231.
- van Oort, E. S., A. M. van Cappellen van Walsum and D. G. Norris (2014). "An investigation into the functional and structural connectivity of the Default Mode Network." Neuroimage **90**: 381-389.
- Vincent, J. L., I. Kahn, A. Z. Snyder, M. E. Raichle and R. L. Buckner (2008). Evidence for a Frontoparietal Control System Revealed by Intrinsic Functional Connectivity.
- Wada, H., H. Saiga, N. Satoh and P. W. Holland (1998). "Tripartite organization of the ancestral chordate brain and the antiquity of placodes: insights from ascidian Pax-2/5/8, Hox and Otx genes." Development **125**(6): 1113-1122.
- Wagner, S. and D. Wagner (2007). Comparing clusterings: an overview, Universität Karlsruhe, Fakultät für Informatik.
- Wang, J., X. Zuo, Z. Dai, M. Xia, Z. Zhao, X. Zhao, J. Jia, Y. Han and Y. He (2013). "Disrupted functional brain connectome in individuals at risk for Alzheimer's disease." Biol Psychiatry **73**(5): 472-481.
- Wang, Y. and T.-Q. Li (2013). "Analysis of Whole-Brain Resting-State fMRI Data Using Hierarchical Clustering Approach." PLoS ONE **8**(10): e76315.
- Weisstein, E. W. (2017). "Complexity." Retrieved 2017-04-27, from <http://mathworld.wolfram.com/Complexity.html>.
- Whitfield-Gabrieli, S. and J. M. Ford (2012). "Default Mode Network Activity and Connectivity in Psychopathology." Annual Review of Clinical Psychology **8**(1): 49-76.
- Wicht, H. and R. G. Northcutt (1992). "The forebrain of the Pacific hagfish: a cladistic reconstruction of the ancestral craniate forebrain." Brain Behav Evol **40**(1): 25-64.
- Wornell, G. W. (1993). "Wavelet-based representations for the 1/f family of fractal processes." Proceedings of the IEEE **81**(10): 1428-1450.

- Wu, C. W., H. Gu, H. Lu, E. A. Stein, J.-H. Chen and Y. Yang (2008). "Frequency specificity of functional connectivity in brain networks." NeuroImage **42**(3): 1047-1055.
- Xue, S. W., D. Li, X. C. Weng, G. Northoff and D. W. Li (2014). "Different neural manifestations of two slow frequency bands in resting fMRI: A systemic survey at regional, inter-regional, and network levels." Brain Connect.
- Yaesoubi, M., E. A. Allen, R. L. Miller and V. D. Calhoun (2015). "Dynamic coherence analysis of resting fMRI data to jointly capture state-based phase, frequency, and time-domain information." NeuroImage **120**: 133-142.
- Zahn, C. T. (1971). "Graph-Theoretical Methods for Detecting and Describing Gestalt Clusters." Computers, IEEE Transactions on **C-20**(1): 68-86.
- Zalesky, A., A. Fornito, L. Cocchi, L. L. Gollo and M. Breakspear (2014). "Time-resolved resting-state brain networks." Proceedings of the National Academy of Sciences **111**(28): 10341-10346.
- Zhou, W., A. C. Bovik, H. R. Sheikh and E. P. Simoncelli (2004). "Image quality assessment: from error visibility to structural similarity." IEEE Transactions on Image Processing **13**(4): 600-612.
- Zuo, X. N., A. Di Martino, C. Kelly, Z. E. Shehzad, D. G. Gee, D. F. Klein, F. X. Castellanos, B. B. Biswal and M. P. Milham (2010). "The oscillating brain: complex and reliable." Neuroimage **49**(2): 1432-1445.